Squeezed-Light-Enhanced Magnetometry in a High Density Atomic Vapor

Charikleia Troullinou

A thesis submitted for the degree of Doctor of Philosophy

ICFO - The Institute of Photonic Sciences
UPC - Universitat Politècnica de Catalunya

Thesis Advisor: Prof. Dr. Morgan W. Mitchell

to "Family"

Abstract

This thesis describes experiments that employ squeezed light to improve the performance of a sensitive optically-pumped magnetometer (OPM). The squeezed light source employs parametric amplification of vacuum fluctuations to produce squeezed vacuum and polarization-squeezed light tunable around the Rb D_1 line. The OPM employs Bell-Bloom optical pumping of a high density vapor (with atom number density $n \sim 1 \times 10^{13}$ atoms/cm^3) and paramagnetic Faraday rotation, also on the Rb D_1 line. The setup allows convenient switching from probing with laser light to probing with polarization-squeezed light, to study the use of the latter in atomic magnetometry.

The magnetometer shows sub-pT/$\sqrt{\text{Hz}}$ sensitivity, limited by quantum noise; spin projection noise at low frequencies ($\lesssim 100\,\text{Hz}$) and photon shot noise at high frequencies. Probing with polarization squeezed light suppresses the photon shot noise by $\sim 2\,\text{dB}$, limited by the available squeezing and optical losses in passing through the vapor. This shot-noise suppression improves the high-frequency sensitivity and increases the measurement bandwidth, with no observed loss of sensitivity at any frequency. This result confirms experimentally the expected evasion of measurement back-action noise in the Bell-Bloom magnetometer.

The thesis also develops a physical model to explain the observed spin dynamics of the Bell-Bloom magnetometer. The model describes the combined spin and optical polarization dynamics using Bloch equations with stochastic drive and detection noise terms. A perturbative approach and Fourier methods are then used to obtain analytic expressions for the magnetometer's frequency response, spin projection noise and photon shot noise. The role of measurement back-action emerges from a study of this model. As polarization squeezing reduces optical noise in the detected Stokes parameter, the accompanying ellipticity anti-squeezing is shunted into the unmeasured spin component.

The thesis also reports a study of squeezed-light-enhanced magnetometry at a range of atomic densities, from 2.18×10^{12} atoms/cm^3 to 1.13×10^{13} atoms/cm^3. Operating with fixed conditions of optical pumping, the signal amplitude, instrument noise spectrum and magnetic resonance width are measured as a function of atomic number density, for both laser- and squeezed-light probing. The equivalent magnetic noise spectra are then calculated. In the photon-shot-noise-limited portion of the spectrum, the squeezed light probing improves the magnetometer's sensitivity and measurement bandwidth for the full range of atomic density values. In particular, the laser-probed magnetometer shows a sensitivity optimum at $n \approx 6 \times 10^{12}$ atoms/cm^3, and the squeezed-light-probed magnetometer surpasses this sensitivity.

The thesis concludes with a discussion of the potential of stronger optical squeezing to enhance the instrument's sensitivity in different portions of the spectrum. Using the theory model we estimate the enhancement of the equivalent magnetic noise spectrum for $2\,\text{dB}$, $5.6\,\text{dB}$ and perfect squeezing (zero noise in the detected polarization component) at the input to the atomic medium.

Resum

Aqueta tesi descriu la millora d'un magnetòmetre de bombeig òptic (OPM) mitjançant l'ús d'estats de llum amb incertesa comprimida (squeezed states). S'usa amplificació paramètrica per a comprimir la incertesa de la font de llum. En concret, es comprimeix la incertesa de l'estat de buit quàntic, com també de la polarització òptica, amb la possibilitar d'ajustar la longitud d'ona al voltant de la transició atòmica D_1 de ^{87}Rb. L'OPM usa bombeig òptic Bell-Bloom de vapors d'alta densitat (amb densitats atòmiques properes a 10^{13}) i rotació de Faraday, també al voltant de la transició atòmica D_1 de ^{87}Rb. L'aparell experimental permet canviar de mostreig amb llum coherent làser a mostreig amb llum de polarització comprimida, amb la finalitat d'avaluar el seu impacte en la sensitivitat del magnetòmetre.

El magnetòmetre té una sensitivitat de sub-pT/$\sqrt{\text{Hz}}$, principalment limitada per soroll quàntic; soroll de projecció de spin a baixes freqüències ($\lesssim 100\,\text{Hz}$) i soroll de quantització fotònica a altes freqüències. L'ús d'estats de llum amb polarització comprimida permet reduir el soroll fotònic en $\sim 2\,\text{dB}$, limitat per la compressió disponible i les pèrdues en travessar el vapor atòmic. La supressió del soroll fotònic augmenta l'amplada de banda del sistema amb l'avantatge de no perdre sensitivitat a cap banda de freqüència. Els resultats experimentals confirmen l'esperada supressió de retroalimentació de soroll en magnetòmetres de Bell-Bloom.

La tesi també estudia el model teòric darrere les dinàmiques de spin en un magnetòmetre de tipus Bell-Bloom. El model descriu la combinació de les dinàmiques de spin i de la polarització òptica mitjançant equacions de Bloch forçades estocàsticament i amb termes de soroll de detecció. Es treballa en el límit pertorbatiu on mitjançant mètodes de Fourier s'obtenen expressions analítiques de la resposta en freqüència del magnetòmetre, dels sorolls de projecció de spin i del soroll de quantització fotònica. El rol de la retroalimentació de soroll també s'extrau d'aquest model. En concret, s'observa que la compressió en polarització redueix el soroll en els paràmetres de Stokes detectats, mentre els paràmetres de spin no mesurats experimenten una expansió de la seva incertesa (anti-squeezing).

La tesi estudia magnetòmetres òptics de llum amb incertesa comprimida per a densitats entre $2.18 \times 10^{12}\,\text{atoms/cm}^3$ i $1.13 \times 10^{13}\,\text{atoms/cm}^3$. Es mesuren l'amplitud de senyal, l'espectre de soroll i l'amplada de la ressonància magnètica en funció de la densitat atòmica, per a un bombeig òptic constant i per a ambdós tipus de mostreig òptic (llum coherent i llum de polarització comprimida). A continuació, es calculen els espectres de soroll equivalents. En la part d'espectre on domina el soroll de quantització fotònica, s'observa que l'ús de llum de polarització comprimida millora la sensitivitat del magnetòmetre al llarg de tot el rang

de densitats atòmics. En concret, la sensitivitat del magnetòmetre amb mostreig coherent és òptima per a $n \approx 6 \times 10^{12}$ atoms/cm^3 i es demostra una millora amb l'ús de mostreig amb llum comprimida.

Es conclou amb una discussió sobre l'efecte de compressions més severes en la sensitivitat del magnetòmetre. Mitjançant el model teòric s'estima la millora en la sensitivitat per a compressions de 2 dB, 5.6 dB i "compressió perfecta" a l'entrada del medi atòmic.

Contents

Contents

1

Introduction

The study of quantum noise in measurement is motivated both by the fundamental theory of quantum mechanics and practical applications. In a sensor with optical readout, a fundamental source of noise is optical shot noise that appears due to the discrete arrival of photons to the detector [1, 2].

Historically, the work of Braginsky [3] and Helstrom [4] were the first to explain the role of quantum mechanical noise in the performance of a sensor. For a quantum noise limited sensor, detecting for example mechanical displacement or a small magnetic field, the sensitivity can be improved when squeezed states are used.

The most well known example of quantum enhanced sensitivity is the optical interferometers used for gravitational wave detection [5, 6, 7]. Caves [8] in 1981 proposed the use of squeezed light for probing the interferometer in order to suppress shot noise dominating in the high frequency range of the spectrum. Since then, the advance of laser technology and optomechanics allowed for greater power to be used for probing. It was noted though that a very high level of optical power introduces nonlinear optical effects that have a deleterious impact on the sensitivity [9]. Almost 30 years after the original proposal, squeezed light probing was employed to improve in practice the instruments' sensitivity to a level that could not be achieved with classical methods [10, 11].

The application of squeezed light in the optical interferometers demonstrates as well the effect of measurement back-action. Squeezing of the phase fluctuations inevitably increases the noise in amplitude quadrature. This gives rise to radiation pressure increasing the total noise in the low-frequency range of the spectrum. More sophisticated methods are required to handle the measurement back-action and improve the sensor's sensitivity throughout the spectrum [12, 13]. The history of noise suppression in optical interferometers indicates that quantum enhancement techniques are of interest for physical systems in which the sensitivity cannot be improved with classical methods, e.g., increasing the optical power or reducing the technical noise. The recent technological advancement and the trend towards miniaturized sensors with low technical noise make atomic sensors and in particular optically pumped magnetometers (OPMs) an ideal platform to

test quantum enhancement techniques.

The understanding of optical pumping theory [14, 15] and the evolution of laser technology have contributed significantly to the development of OPMs reaching sub-fT$\sqrt{\text{Hz}}$ sensitivities [16, 17]. OPMs have numerous applications in geomagnetic [18, 19, 20] and biomagnetic research [21, 22, 23], space science and physics beyond the standard model [24].

In a simple scheme, OPMs contain two interacting systems: an atomic ensemble and light that optically prepares and detects the atomic state. Quantum noise [25] is associated with atoms and photons. The atomic quantum noise often also mentioned as *spin projection noise* is related to the intrinsic uncertainty the atomic observables. It can be reduced through non-disturbing measurement of the atomic state, known as quantum non-demolition (QND) measurements. They have been employed in experiments of high atomic density sensors [26, 27] and showed atomic entanglement. *Photon shot noise* is white noise, contributing equally throughout the spectrum of the atomic magnetometer. A magnetometer employing a differential polarization detection of light after the atomic interaction can be though of as a polarization interferometer. Therefore, the squeezed light enhancement of optical interferometers motivates the use of optical squeezing for atomic magnetometers.

Light squeezing in atomic magnetometry

In the following section, we summarize the magnetometers known as squeezed light enhanced. They are atomic magnetometers in which optical squeezing has been employed and it has improved the sensitivity.

A squeezed light enhanced magnetometer was first accomplished in 2010 [28] with polarization squeezing generated through spontaneous parametric down-conversion (SPDC) in a sub-threshold optical parametric oscillator cavity. The magnetometer operated by alignment to orientation conversion in an ensemble of Rb atoms pumped only by the off-resonant probe light. The experiment was performed in an area of operating parameters for which the photon shot noise was dominant, so that the suppression of photon shot noise due to squeezed light probing has been considerable. The magnetometer sensitivity was improved by 3.2 dB and reached nT/$\sqrt{\text{Hz}}$ sensitivity when polarization squeezed light was used for probing. The vapor cell of this experiment was at low temperature, a condition beneficial for preserving to a good degree the generated squeezing. At this low density any measurement backaction effect would have been negligible.

In 2012, a magnetometer with orders of magnitude improved sensitivity was realized by Horrom et al. [29]. Squeezed light was generated through polarization self-rotation in an atomic squeezer, in a Rb cell placed before the magnetometer and along the propagation axis. Even though the squeezer has been

Reference	Atomic magnetometer	Type of squeezer	Sensitivity $(\mathrm{pT}/\sqrt{\mathrm{Hz}})$	Squeezing improvement (dB)
Wolfgramm et al. (2010) [28]	NMOR	SPDC OPO	$\sim 10^4$	3.2
Horrom et al. (2012) [29]	NMOR	PSR	2	2
Otterstrom et al. (2014) [30]	NMOR Single beam	FWM	19.3	4.7
Novikova et al. (2015) [31]	Nonlinear Faraday effect	PSR	3	2
Bai et al. (2021) [32]	NMOR	PSR	20	3.7
Troullinou et al. (2021) [33]	Bell Bloom OPM, Faraday rotation	SPDC OPO	0.3	2

Table 1.1.: Optically pumped magnetometers employing optical squeezing to improve sensitivity. SPDC: spontaneous parametric down-conversion, OPO: optical parametric oscillator, PSR: polarization self-rotation, FWM: Four-wave mixing.

designed to have good performance at low frequencies, this has not been achieved due to laser technical noise. The same squeezed light source was used to probe the magnetometer while operating at different atomic densities. It was demonstrated that optical squeezing improves the sensitivity only for conditions of atomic density lower than 2×10^{11} atoms/cm^3. The best sensitivity reported for 2×10^{11} atoms/cm^3 did not change with optical squeezing while the sensitivity of the magnetometer with atomic density higher than that is worse when probed with squeezed light. The authors mention "At higher densities, squeezing is degraded due to absorption by the atoms and so we expect less noise suppression. We also see that at the highest densities, due to the backaction of atoms, the total noise is amplified rather than suppressed. This effect shows that using squeezed light will only improve the magnetometer sensitivity at certain atomic densities and experimental conditions "

In 2014, Otterstrom et al. [30] operated a single beam NMOR magnetometer, enhanced by optical squeezing. The squeezed light was generated by means of four wave mixing in a cell of ^{85}Rb and they reported 4.7 dB of squeezing. The magnetometer's sensitivity was 20 pT/$\sqrt{\mathrm{Hz}}$.

In 2015, squeezed light magnetometry was performed by Novikova et al. [31] to study the additional noise in polarization self-rotation (PSR). This setup also

included a single cell of non-polarized ^{87}Rb. The squeezed light suppressed the noise by $4\,\mathrm{dB}$ at $2 \times 10^{11}\,\mathrm{atoms/cm}^3$. The sensitivity after the squeezing was $20\,\mathrm{pT}/\sqrt{\mathrm{Hz}}$ and it was estimated to improve with increased atom number density.

In recent experiments [32] Bai et al. demonstrated improved squeezing ($3.7\,\mathrm{dB}$) at low frequencies. They implemented it in a single beam low density atomic magnetometer and reported the sensitivity of about $20\,\mathrm{pT}/\sqrt{\mathrm{Hz}}$ to improve when the magnetometer is probed with squeezed light.

Optical squeezing and NMOR magnetometry has been studied by Zhang et al. [34] in a single beam setup where squeezing may be generated during the magnetic sensing process, depending on the probe power level. In this study the magnetometer was shown to be most sensitive in the low optical power regime where squeezing is not generated.

The above activities are indicative of the strong interest on the role of optical quantum noise in magnetometers. Meanwhile, a main goal in magnetometry is to improve the sensitivity, which often requires high atomic number densities. At the same time, at high atomic number densities measurement backaction can introduce significant extra noise, which moreover depends on the measurement scheme [35]. In this context, this thesis presents an experimental study to test the utility of squeezed light in a sensitive OPM in which quantum noise is the dominant noise source across the spectrum. The magnetometer scheme is also designed to evade measurement backaction.

Thesis outline

The thesis is organized as follows;

Chapter 2 introduces the concepts of quadrature squeezing and polarization squeezing. The latter's generation and detection are explained through Stokes operators in the single-mode description. A continuous-time description of the polarization noise properties follows. The chapter finishes with a brief discussion on optical parametric amplification as a process to generate squeezing.

Chapter 3 presents a solution of the Bloch equations when considering the main physical effects in an OPM; the spin precession in the presence of a magnetic field, relaxation and optical pumping. Introducing the atom-light interaction Hamiltonian later we explain a probing scheme of the spin dynamics based on Faraday rotation and the AC stark shift that can be a source of measurement back-action noise.

Chapter 4 reports results from the application of squeezed light to a sub-$\mathrm{pT}/\sqrt{\mathrm{Hz}}$ Bell-Bloom magnetometer when operating at an atomic density of $n \sim 1 \times 10^{13}\,\mathrm{atoms/cm}^3$. The squeezed light source generates polarization squeezing tunable around the Rb D1 line. When optical squeezing is used to probe the

quantum noise limited OPM, the shot noise suppression improves the high frequency sensitivity and increases the measurement bandwidth. The results prove experimentally the evasion of measurement backaction noise in the Bell-Bloom magnetometer. The results of this work are presented in [33].

Chapter 5 introduces a physical model to explain the spin dynamics in the magnetometer using Bloch equations. The model employs also a perturbative approach and Fourier methods. Analytic expressions are derived for the magnetometer's frequency response and the equivalent magnetic noise spectrum. The model is published in the supplemental material of [33].

Chapter 6 contains details on the magnetometer operation regarding the optical pumping and the signal analysis. The squeezed light source is briefly described focusing mostly on the novelties introduced to generate $\sim 2.3\,\mathrm{dB}$ of squeezing. The discussion finishes with the description of the electronic chain used for the quantum noise lock of the magnetometer signal's noise.

Chapter 7 reports a study of a squeezed-light-enhanced magnetometer operating at a range of atomic densities from $2.18 \times 10^{12}\,\mathrm{atoms/cm^3}$ to $1.13 \times 10^{13}\,\mathrm{atoms/cm^3}$. For fixed conditions of optical pumping we measure the magnetometer's signal, the magnetic resonance width and the equivalent magnetic noise spectra for different atomic number density. Squeezed light probing improves the high frequency sensitivity and the measurement bandwidth for all the atomic density values tested, including densities on either side of the optimum.

Chapter 8 summarizes the results of the thesis and closes with a discussion on the potential of higher squeezing improving the sensitivity at different frequencies of the spectrum.

2

Theoretical background of polarization squeezing generation and detection

This chapter contains a theoretical description of quadrature squeezing and polarization squeezing. First we introduce the Stokes operators in the single mode scenario to explain squeezed light generation and detection. A continuous time description of the Stokes operators is used to infer the polarization noise properties. The chapter finishes with a discussion of squeezed light generation through optical parametric amplification.

2.1. Squeezing of Light

The concept of squeezing is central in quantum optics and sensing as it refers to the reduction of an observable's variance $(\Delta \hat{A})^2 = \langle \hat{A}^2 \rangle - \langle \hat{A} \rangle^2$ below a standard quantum limit (SQL). This observable may relate to atomic or photonic states and the standard quantum limit is normally set by the corresponding coherent states.

2.1.1. Quadrature squeezing

The modes of the electromagnetic field are described with the quadrature operators that are expressed as a function of the creation a and annihilation operators $a^\dagger$, as

$$X_1 \equiv a + a^\dagger \tag{2.1}$$
$$X_2 \equiv i(a^\dagger - a). \tag{2.2}$$

Then the single mode contribution of wavevector $\mathbf{k}$ and frequency ω to the electromagnetic field at time t and position $\mathbf{r}$ is

$$E_{\mathbf{k},\omega}(\mathbf{r}, t) \sim X_1 \sin(\mathbf{k} \cdot \mathbf{r} - \omega t) - X_2 \cos(\mathbf{k} \cdot \mathbf{r} - \omega t). \tag{2.3}$$

Given the commutation relation for the creation (a) and annihilation ($a^\dagger$) operators, for the operators X_1 and X_2, follows that

$$[X_1, X_2] = 2i. \tag{2.4}$$

The above commutation relation gives rise to the uncertainty relation

$$\Delta X_1 \Delta X_2 \geqslant 1, \tag{2.5}$$

where $(\Delta X_i|_\beta)^2 \equiv \langle\beta|X_i^2|\beta\rangle - \langle\beta|X_i|\beta\rangle^2$ is the variance of the quadrature component $X_i, i \in [1, 2]$ calculated in the quantum state $|\beta\rangle$. Suppressing the uncertainty of one quadrature then implies the expansion of the uncertainty in the other one so that the above relation holds.

Starting from the relation for the coherent state $|\alpha\rangle$ [1] with amplitude $|\alpha|$ and phase ϕ ;

$$a|\alpha\rangle = |\alpha|e^{i\phi}|\alpha\rangle. \tag{2.6}$$

a simple calculation leads to

$$(\Delta X_i|_\alpha)^2 = \langle\alpha|X_i^2|\alpha\rangle - \langle\alpha|X_i|\alpha\rangle^2 = 1, \quad \text{for} \quad i \in [1, 2]. \tag{2.7}$$

The quantum state $|\xi\rangle$ for which

$$(\Delta X_i|_\xi)^2 < 1 \quad \text{for} \quad i \in [1, 2] \tag{2.8}$$

is known as squeezed state. The squeezed state $|\xi\rangle \equiv S(\xi)|0\rangle$ is generated from the vacuum state $|0\rangle$ (a special coherent state with $\langle 0|a^\dagger a|\alpha\rangle \equiv 0$) by applying the squeezing operator

$$S(\xi) = \exp\left[\frac{1}{2}\xi^* a^2 - \frac{1}{2}\xi(a^\dagger)^2\right], \tag{2.9}$$

where $\xi = re^{-2i\phi}$ is the squeezing parameter with amplitude r and phase ϕ.

2.1.2. Polarization Squeezing

Similarly one can define the squeezing of polarization of light. To describe this, we introduce the Stokes operators

$$S_0 = \frac{1}{2}(a_H^\dagger a_H + a_V^\dagger a_V) \tag{2.10}$$

$$S_1 = \frac{1}{2}(a_H^\dagger a_H - a_V^\dagger a_V) \tag{2.11}$$

$$S_2 = \frac{1}{2}(a_H^\dagger a_V + a_V^\dagger a_H) \tag{2.12}$$

$$S_3 = -\frac{i}{2}(a_H^\dagger a_V - a_V^\dagger a_H), \tag{2.13}$$

where $a_\alpha, a_\alpha^\dagger$, are the creation and annihilation operators of electric field mode α and the polarization modes are horizontal (H) and vertical (V). The creation and annihilation operators obey the commutation relations $[a_i, a_j^\dagger] = \delta_{ij}$, and a simple calculation finds

$$[S_i, S_j] = i\epsilon_{ijk}S_k, \quad i, j, k \in \{1, 2, 3\} \tag{2.14}$$

and

$$[S_0, S_i] = 0, \quad i, j, k \in \{1, 2, 3\}, \tag{2.15}$$

which we recognize as angular momentum commutation relations.

Defining annihilation operators for the diagonal (D), anti-diagonal (A), left circular (L) and right circular (R) polarizations as

$$a_D \equiv \frac{1}{\sqrt{2}}(a_H + a_V) \tag{2.16}$$

$$a_A \equiv \frac{1}{\sqrt{2}}(a_H - a_V) \tag{2.17}$$

$$a_L \equiv \frac{1}{\sqrt{2}}(a_H + ia_V) \tag{2.18}$$

$$a_R \equiv \frac{1}{\sqrt{2}}(a_H - ia_V), \tag{2.19}$$

we can write (Equation 2.10)-(Equation 2.13) as

$$S_0 = \frac{1}{2}(a_H^\dagger a_H + a_V^\dagger a_V) \tag{2.20}$$

$$S_1 = \frac{1}{2}(a_H^\dagger a_H - a_V^\dagger a_V) \tag{2.21}$$

$$S_2 = \frac{1}{2}(a_D^\dagger a_D - a_A^\dagger a_A) \tag{2.22}$$

$$S_3 = \frac{1}{2}(a_R^\dagger a_R - a_L^\dagger a_L). \tag{2.23}$$

Each Stokes operator is thus the sum or difference of photon numbers in a pair of orthogonal modes, and thus directly observable using polarization optics and a pair of detectors.

2. Theoretical background of polarization squeezing generation and detection

A polarization squeezed state can be generated by combining two quadrature squeezed states [36]. It can also be generated by combining in a single spatial mode a strong coherent state of one polarization with squeezed vacuum of the orthogonal polarization. This is the scenario of our squeezed light source [37] that generates squeezed vacuum when a periodically-poled nonlinear optical crystal is pumped by a frequency-doubled laser.

The coherent polarization state can be defined as the product of two coherent states with perpendicular polarization $|\alpha_H\rangle \otimes |\alpha_V\rangle$. Using this symbolism for both the horizontal and vertical component, the mean values of the Stokes operators are

$$\langle S_0 \rangle = \frac{1}{2}(|\alpha_H|^2 + |\alpha_V|^2) \tag{2.24}$$

$$\langle S_1 \rangle = \frac{1}{2}(|\alpha_H|^2 - |\alpha_V|^2) \tag{2.25}$$

$$\langle S_2 \rangle = |\alpha_H||\alpha_V|\cos(\Delta\phi) \tag{2.26}$$

$$\langle S_3 \rangle = |\alpha_H||\alpha_V|\sin(\Delta\phi), \tag{2.27}$$

where $\Delta\phi \equiv \phi_V - \phi_H$ is the relative phase difference between the vertical and horizontal polarization input states. We consider now the scenario where the amplitude of the field with horizontal polarization is larger than the one of the vertical,

$$|\alpha_H| = |\alpha_{\mathrm{LO}}| \gg |\alpha_V|. \tag{2.28}$$

and without loss of generality we set $\phi_H = 0$. The approximate Stokes operators can then be written as

$$S_1 \approx S_0 \approx \frac{1}{2}|\alpha_{\mathrm{LO}}|^2 \tag{2.29}$$

$$S_2 \approx |\alpha_{\mathrm{LO}}|X_{1,V} \tag{2.30}$$

$$S_3 \approx |\alpha_{\mathrm{LO}}|X_{2,V}, \tag{2.31}$$

where $X_{i,V}$ and $X_{i,H}$, $i \in [1,2]$, are the quadrature operators for the field in the vertical and horizontal polarization, respectively. The uncertainties of the Stokes parameters also depend linearly on the uncertainties of the quadrature components

$$\Delta S_2 \approx |\alpha_{\mathrm{LO}}|^2 \Delta X_{1,V} \quad \text{and} \quad \Delta S_3 \approx |\alpha_{\mathrm{LO}}|^2 \Delta X_{2,V}. \tag{2.32}$$

Therefore, quadrature squeezing of the vertical component ($\Delta X_{1,V} < 1$) leads to polarization squeezing ($\Delta S_2/|\alpha_{\mathrm{LO}}|^2 < 1$). At the same, squeezing of S_2 implies the antisqueezing of S_3.

As described in more detail in chapter 6, the squeezing of the S_2 Stokes parameter in this experiment is achieved when the output of the OPO cavity, squeezed vacuum with reduced noise fluctuations in the vertical component ($S(\xi)\,|0\rangle_V = |\xi\rangle_V$), is combined at a polarizing beam splitter (PBS) with the local oscillator in the horizontal polarization, $|a_{\mathrm{LO}}\rangle_{\mathrm{H}}$.

The S_2 Stokes component (Equation 2.22) is detected with a balanced polarimeter, consisting of a PBS and a preceded halfwave plate set to detect polarization components in the diagonal/antidiagonal basis.

2.1.3. Time-dependent Stokes operators

The above Stokes operators, defined in terms of photon number observables, are often convenient, especially for describing optical pulses. In other situations, including the continuous probing to be described in chapter 4 and chapter 5, it is necessary to have a continuous-time description of the polarization. For this purpose, we define continuous-time Stokes operators

$$S_0(t) \;=\; \frac{1}{2}[\mathring{E}_H^{(-)}(t)\mathring{E}_H^{(+)}(t) + \mathring{E}_V^{(-)}(t)\mathring{E}_V^{(+)}(t)] \tag{2.33}$$

$$S_1(t) \;=\; \frac{1}{2}[\mathring{E}_H^{(-)}(t)\mathring{E}_H^{(+)}(t) - \mathring{E}_V^{(-)}(t)\mathring{E}_V^{(+)}(t)] \tag{2.34}$$

$$S_2(t) \;=\; \frac{1}{2}[\mathring{E}_H^{(-)}(t)\mathring{E}_V^{(+)}(t) + \mathring{E}_V^{(-)}(t)\mathring{E}_H^{(+)}(t)] \tag{2.35}$$

$$S_3(t) \;=\; -\frac{i}{2}[\mathring{E}_H^{(-)}(t)\mathring{E}_V^{(+)}(t) - \mathring{E}_V^{(-)}(t)\mathring{E}_H^{(+)}(t)], \tag{2.36}$$

where

$$\mathring{E}_\alpha^{(+)}(t) = \left[\mathring{E}_\alpha^{(-)}(t)\right]^\dagger \equiv c_E E_\alpha^{(+)}(t) \tag{2.37}$$

and $E_\alpha^{(+)}$ is the positive-frequency part of the quantized electromagnetic field with polarization α.[1] Expressing these in the H/V, A/D, and L/R bases as in Equation 2.16 - Equation 2.23, we obtain

$$S_0(t) \;=\; \frac{1}{2}[\mathring{E}_H^{(-)}(t)\mathring{E}_H^{(+)}(t) + \mathring{E}_V^{(-)}(t)\mathring{E}_V^{(+)}(t)] \tag{2.38}$$

$$S_1(t) \;=\; \frac{1}{2}[\mathring{E}_H^{(-)}(t)\mathring{E}_H^{(+)}(t) - \mathring{E}_V^{(-)}(t)\mathring{E}_V^{(+)}(t)] \tag{2.39}$$

---

[1]In describing the field this way, i.e., with a time coordinate but without spatial coordinates, we are implicitly assuming that the quantities of interest to us will be the Stokes operators, and thus normally-ordered products of the fields of the form $E_\alpha^{(-)}(t)E_\beta^{(+)}(t)$, in a specific transverse mode (here the probe beam mode), and always close to a single longitudinal plane, which we can call $z = 0$. Concretely, taking the centre of the vapor cell as $z = 0$, and considering the 5 µs time resolution of the detection, any points within about 1 km of the vapor cell would count as "close."

$$S_2(t) = \frac{1}{2}[\mathring{E}_D^{(-)}(t)\mathring{E}_D^{(+)}(t) - \mathring{E}_A^{(-)}(t)\mathring{E}_A^{(+)}(t)] \tag{2.40}$$

$$S_3(t) = \frac{1}{2}[\mathring{E}_R^{(-)}(t)\mathring{E}_R^{(+)}(t) - \mathring{E}_L^{(-)}(t)\mathring{E}_L^{(+)}(t)]. \tag{2.41}$$

Thus each time-dependent Stokes operator is proportional to a sum or difference of normally-ordered operators of the form $\mathring{E}_\alpha^{(-)}(t)\mathring{E}_\alpha^{(+)}(t)$. From photodetection theory [38], and restricting ourselves to the narrow-band scenario in which all photons have nearly the same frequency, we recognize this operator as (proportional to) the instantaneous photon flux of polarization α. We choose the constant c_E such that for z-propagating light with frequency close to the atomic resonance, $[\mathring{E}_\alpha^{(+)}(t), \mathring{E}_\beta^{(-)}(t')] = \delta(t-t')\delta_{\alpha,\beta}$, where the delta functions are first a Dirac delta and then a Kronecker delta. $\mathring{E}_\alpha^{(-)}(t)\mathring{E}_\alpha^{(+)}(t)$ is then equal to the photon flux of polarization α.

A simple calculation finds as before that

$$[S_i(t), S_j(t')] \propto i\epsilon_{ijk}S_k(t)\delta(t - t'), \;\; i,j,k \in \{1,2,3\}, \tag{2.42}$$

which implies angular-momentum uncertainty relations, and

$$[S_0(t), S_i(t)] = 0, \;\; i,j,k \in \{1,2,3\}, \tag{2.43}$$

which indicates that $S_0(t)$ is commensurate with the other Stokes operators.

Polarization noise properties can be calculated using these time-dependent Stokes operators. For example, we consider a state

$$|\psi\rangle \equiv |\alpha_H\rangle_H \otimes |0\rangle_V \tag{2.44}$$

i.e., a coherent state with amplitude α_H for the mode with polarization H and frequency ω, and amplitude zero for the mode V, and with amplitudes defined such that the positive-frequency field operators act on this state as $\mathring{E}_H^{(+)}(t)|\psi\rangle = \alpha_H \exp[-i\omega t]|\psi\rangle$, $\mathring{E}_V^{(+)}(t)|\psi\rangle = 0$. We can then evaluate expectation values to find $\langle S_0(t)\rangle = \langle S_1(t)\rangle = |\alpha_H|^2/2$, while $\langle S_2(t)\rangle = \langle S_3(t)\rangle = 0$, describing a state that is fully horizontally polarized. Using Equation 2.34 - Equation 2.35, we can then compute the auto-correlation of $S_2(t)$

$$
\begin{aligned}
\langle\psi|S_2(t)S_2(t')|\psi\rangle &= \frac{1}{4}\langle\psi|[\mathring{E}_H^{(-)}(t)\mathring{E}_V^{(+)}(t) + \mathring{E}_V^{(-)}(t)\mathring{E}_H^{(+)}(t)] \\
&\quad \times [\mathring{E}_H^{(-)}(t')\mathring{E}_V^{(+)}(t') + \mathring{E}_V^{(-)}(t')\mathring{E}_H^{(+)}(t')]|\psi\rangle \\
&= \frac{1}{4}\langle\psi|[\mathring{E}_H^{(-)}(t)\mathring{E}_V^{(+)}(t)\mathring{E}_V^{(-)}(t')\mathring{E}_H^{(+)}(t')]|\psi\rangle \\
&= \frac{1}{4}|\alpha_H|^2\langle\psi|\mathring{E}_V^{(+)}(t)\mathring{E}_V^{(-)}(t')|\psi\rangle
\end{aligned}
$$

$$= \frac{1}{2}\langle S_1(t)\rangle \delta(t-t') \tag{2.45}$$

A horizontally-polarized coherent state thus produces delta-correlated white noise in $S_2(t)$, with a noise power proportional to $\langle S_0(t)\rangle = \langle S_1(t)\rangle$, and thus to the mean optical power. A very similar calculation shows that

$$\langle \psi|S_3(t)S_3(t')|\psi\rangle = \frac{1}{2}\langle S_1(t)\rangle \delta(t-t'), \tag{2.46}$$

and thus that $S_3(t)$ is also delta-correlated white noise, with the same noise power. In chapter 5, $S_2(t)$ and $S_3(t)$ will be denoted by N_{S_2} and N_{S_3}, respectively.

We can recover the single-mode description of Equation 2.10 - Equation 2.13 as follows. We consider a pulse with envelope amplitude $f(t)$, normalized such that $\int dt |f(t)|^2 = 1$. We define

$$a_{f,\alpha} \equiv \int dt\, f(t)\mathring{E}_\alpha^{(+)}(t), \tag{2.47}$$

from which we find the single-mode commutation relation

$$[a_{f,\alpha}, a_{f,\beta}^\dagger] = \int dt\, dt'\, f(t)f^*(t')[\mathring{E}_\alpha^{(+)}(t), \mathring{E}_\beta^{(-)}(t')] \tag{2.48}$$

$$= \int dt\, dt'\, f(t)f^*(t')\delta(t-t')\delta_{\alpha,\beta} \tag{2.49}$$

$$= \delta_{\alpha,\beta}\int dt\, f(t)f^*(t) \tag{2.50}$$

$$= \delta_{\alpha,\beta}. \tag{2.51}$$

2.2. Light propagation in a nonlinear medium

As light propagates inside the medium, the electromagnetic field ($\mathbf{E}$) affects the electronic charge distribution of the atoms and therefore changes the medium's polarization $\mathbf{P}$. This macroscopic change is described by

$$\mathbf{P} = \epsilon_0 \chi \mathbf{E} \tag{2.52}$$

where ϵ_0 is the electric permittivity of vacuum and χ is the electric susceptibility. The latter is in fact a function of the electromagnetic field and it can be written as

$$\chi(\mathbf{E}) = \chi^{(1)} + \chi^{(2)}\mathbf{E} + \chi^{(3)}\mathbf{E}\mathbf{E} + \cdots \tag{2.53}$$

Here the linear part of the susceptibility is used in processes like absorption or refraction and it is encountered in the definition of the refractive index of the

medium $n = \sqrt{1 + \chi^{(1)}}$. The high order terms of the susceptibility, $\chi^{(2)}$ and $\chi^{(3)}$, are used for the description of non linear optical processes that give rise to non classical states of light.

2.3. Squeezed light generation with parametric amplification

Several nonlinear optical effects have been demonstrated to produce optical squeezing. Some of them are parametric amplification by three-wave mixing, parametric amplification by four-wave mixing [39], two-photon absorption and optical polarization self-rotation [40, 41, 42].

Parametric amplification with three-wave mixing [43] employs the $\chi^{(2)}$ nonlinearity of a material such as a non-centrosymmetric crystal that is pumped with short-wavelength laser beam. The pump laser frequency is $\omega_p = 2\omega$ the second harmonic of the frequency of the field to be amplified. The parametric process changes the noise properties of the field. It produces an amplification of one quadrature and de-amplification of its conjugate one. When fed with vacuum, which has equal noise in each quadrature, the output has one quadrature with noise below the vacuum noise level, which is also the standard quantum limit (SQL).

In practice, the $\chi^{(2)}$ parametric amplification can be produced in a crystal that is transparent to both ω and 2ω, and introduces very little excess noise. For an enhanced performance of the parametric amplification the χ^2 crystal is placed in a cavity. Optical parametric amplification takes place when the pump power is below the resonator's threshold. The threshold is defined as the minimum pump power for which the signal or idler modes experience more gain due to the down-conversion than loss after the multiple pass in the cavity. The degree of the generated squeezing is then limited by optical losses prior to the photo-detection.

Squeezed light sources employing this method are tunable to a wide range of frequencies. Therefore, they can be used along with lasers of existing instruments, e.g. in gravitational-wave detection, or tuned to any desired point relative to an atomic line. Squeezing up to 15 dB below the SQL [44] has been demonstrated at 1064 nm. For shorter wavelengths though squeezing generation is less efficient, e.g. 5.6 dB of quadrature squeezing at 795 nm [45, 46].

3

Atomic vapor spin dynamics

This chapter discusses basic concepts of atomic physics that are useful for the understanding of the dynamics in the main experiment (chapter 4) as well as the discussion of the quantum noise model (chapter 5). First we describe the evolution of the collective angular momentum in the Bell Bloom magnetometer through the Bloch equations. When assuming a sinusoidal form of the optical pumping, we provide a steady state solution. Later, we consider the atom-light interaction Hamiltonian that explains the Faraday rotation of the off resonant probe and the AC Stark shift that could be a source of measurement back-action noise.

3.1. Atomic spin structure

The ^{87}Rb atoms used in the experiment have a spin-3/2 nucleus and a single spin-1/2 valence electron. The ground state is $5S_{1/2}$, meaning that the electron has no orbital angular momentum, and the total electronic angular momentum is $J = 1/2$. The ground state is split into two hyperfine ground states $F = 1$ and $F = 2$, with a splitting of 6.8 GHz. The excited state of the D_1 transition is $5P_{1/2}$, which again is split into hyperfine states $F = 1$ and $F = 2$, with a splitting of 0.8 GHz.

3.2. Bloch equations

3.2.1. Spin evolution in the presence of a magnetic field

If $\mathbf{F}$ is the collective spin of a collection of atoms in hyperfine ground state F, and $\mathbf{B}$ is the magnetic field experienced by the atoms, the spin dynamics is governed by the Hamiltonian

$$H_B = g_F \mu_B \mathbf{B} \cdot \mathbf{F}, \tag{3.1}$$

where g_F is the Landé factor of hyperfine state F, and μ_B is the Bohr magneton. The equation of motion for **F** is then

$$\frac{d}{dt}\mathbf{F} = -\gamma \mathbf{B} \times \mathbf{F},\qquad(3.2)$$

where $\gamma_F = g_F \mu_B/\hbar$ the gyromagnetic ratio [47]. The hyperfine ground states have gyromagnetic ratios of opposite sign and nearly equal magnitude, and thus they precess in opposite directions. We will refer to an equation like Equation 3.2, i.e., one that describes the precession of a spin vector, as a *Bloch equation*. In what follows, we will add terms to our Bloch equation to give a richer dynamics.

3.2.2. Spin Relaxation

In a hot vapor, several processes cause the depolarization of the atomic spin. This is a complex topic in itself, and we will not make more than a few qualitative observations. A good starting point for understanding collisional relaxation is the thesis of Scott Seltzer [48].

It is helpful to imagine an ensemble of atoms, roughly half of which are in the $F = 1$ state, and half in the $F = 2$ state, each of these sub-ensembles is initially polarized, and as just described they precess in opposite directions.

In a collision between two Rb atoms, the spins of the unpaired electrons interact strongly, but briefly. Two consequences of this interactions are usually distinguished:

A *spin-exchange collision* describes the exchange of angular momentum between the electrons of the colliding atoms. This process does not change the total spin angular momentum of the pair, and thus does not change the total spin angular momentum of the ensemble of atoms. It can, however, flip each electron relative to its accompanying nucleus, and in this way change the hyperfine states of the atoms, and the hyperfine population of the ensemble. Because the collision, and thus the change of hyperfine state, occurs at a random time, the atom will have a random phase relative to other atoms in the hyperfine state it acquires through the collision, and on average the ensemble loses polarization. This is spin-exchange relaxation.

A *spin-destruction collision* describes the exchange of angular momentum between the electron spins and the center-of-mass angular momentum of the colliding pair. This process does not conserve the total spin angular momentum in the ensemble. Spin-destruction collisions are much weaker than spin-exchange collisions, i.e., they have smaller collision cross-sections. They are nonetheless important, because spin destruction collisions can occur between alkali atoms and buffer gas atoms or molecules such as Ne or N_2 that do not have valence electrons. In experiments with high buffer gas pressures, spin-destruction collisions can be a dominant source of spin relaxation.

The *spin-exchange-relaxation-free* (SERF) regime is a regime of low magnetic field and high alkali density, in which spin-exchange collisions happen so frequently that the hyperfine populations do not precess appreciably in the time between spin-exchange collisions. In this regime, any given atom is continually being promoted and demoted in hyperfine level, and the entire ensemble precesses at an average rate. Because the atoms do not have time to dephase due to the differential magnetic precession between hyperfine states, spin-exchange relaxation is greatly reduced in the SERF regime. The highest-sensitivity OPMs work in this regime, but are restricted to measurement of very weak fields.

Collisions of the alkali atoms with cell walls is another relaxation mechanism. An atom colliding with an uncoated glass surface is normally totally depolarized. To reduce this depolarization, atomic cells designed for hot vapor sensors either apply antirelaxation coating to the walls [49] or include a buffer gas [50] to slow diffusion. When buffer gas is used, both diffusion to the walls and spin-destruction collisions may be important in determining the coherence time, and some compromise will give optimal coherence time.

Radiation trapping is when, due to high optical depth of the vapor, resonant or near-resonant light does not escape the cell before suffering several scattering events. This has the effect of depolarizing the atomic spins. N_2 buffer gas acts as a quenching gas [51], mitigating the problem of radiation trapping. At moderate or high buffer gas pressures, an excited Rb atom is likely to suffer a collision before decaying to the ground state, and these collisions can transfer the atom's electronic energy to the vibrational degrees of freedom of the N_2 molecule. To ensure effective quenching, the atoms must suffer several buffer gas collision during the natural lifetime of the optically excited state, and thus the transition must experience collisional broadening by many natural linewidths [14].

The experiments described in chapter 4 and chapter 7 are performed outside the SERF regime, and thus contain two hyperfine populations precessing in opposite directions. A N_2 buffer gas of 100 Torr is used to reduce diffusion to the walls, and to suppress radiation trapping.

The effect of spin relaxation can be incorporated into the dynamical model of Equation 3.2 by adding a relaxation term $-\Gamma\mathbf{F}$, where Γ is the spin-relaxation rate:

$$\frac{d}{dt}\mathbf{F} = -\gamma\mathbf{B} \times \mathbf{F} - \Gamma\mathbf{F} \tag{3.3}$$

3.2.3. Optical Pumping

To generate spin polarization, optical magnetometers employ depopulation optical pumping with circularly polarized light [14]. When illuminated with circularly-polarized light, an atom can only absorb a photon if it is allowed to by selection

rules. For some transitions, and some optical polarizations, no absorption is allowed. For example, with light tuned to the D_1 transition, $5S_{1/2} \rightarrow 5P_{1/2}$, the ground state $F = 2, m_F = 2$, is incapable of absorbing a photon of σ_+ polarization, because a selection rule requires that the excited state would have $m_F = 3$, and there is no state in $5P_{1/2}$ with $m_F = 3$. The state $F = 2, m_F = 2$ is thus "dark" (incapable of scattering light) of with this frequency and polarization. In contrast, all the other states have allowed transitions, and can be excited to the $5P_{1/2}$ level. Once excited, the angular momentum is thoroughly scrambled through collisions with buffer gas, and returns to a random ground state, possibly the $F = 2, m_F = 2$ dark state. In this way, population accumulates in the dark state, and is depleted from the other states. The $F = 2, m_F = 2$ state is, moreover fully polarized, so this constitutes an efficient optical pumping mechanism.

In contrast, the D_2 transition, $5S_{1/2} \rightarrow 5P_{3/2}$, does have states with $m_F = 3$, and the same optical pumping strategy is much less efficient [48]. For this reason, we optically pump on the D_1 transition.

In optical pumping, the spin state is driven toward a polarized equilibrium state $\mathbf{F}_{\mathrm{max}}$. The dynamics of this driving is described by adding a term $-R_{\mathrm{OP}}(\mathbf{F} - \mathbf{F}_{\mathrm{max}})$ to Equation 3.3, to get

$$\frac{d}{dt}\mathbf{F} = -\gamma\mathbf{B} \times \mathbf{F} - \Gamma\mathbf{F} - R_{\mathrm{OP}}(\mathbf{F} - \mathbf{F}_{\mathrm{max}}) \tag{3.4}$$

where the R_{OP} is the pumping rate.

3.2.4. Bell-Bloom excitation

Considering Equation 3.3, if $\mathbf{B}$ and $\mathbf{F}_{\mathrm{max}}$ are not parallel, then as the optical pumping drives $\mathbf{F}$ toward $\mathbf{F}_{\mathrm{max}}$, Larmor precession will simultaneously drive it in an orthogonal direction. In such conditions, it requires strong optical pumping to build up a large polarization, especially for strong fields.

A more efficient optical pumping method was introduced by Bell and Bloom [52]: the optical pumping rate R_{OP} is modulated at a frequency Ω near the Larmor frequency ω or one of its subharmonics. In this scenario the spin polarization precesses, with an amplitude that can build up over several cycles. Here we consider the simplest case, in which $R_{\mathrm{OP}} = \Gamma_{\mathrm{P}}(1 + \cos\Omega t)$, where Γ_{P} is the mean optical pumping rate. Our Bloch equation then becomes

$$\frac{d}{dt}\mathbf{F} = -\gamma\mathbf{B} \times \mathbf{F} - \Gamma\mathbf{F} - \Gamma_{\mathrm{P}}(1 + \cos\Omega t)(\mathbf{F} - \mathbf{F}_{\mathrm{max}}) \tag{3.5}$$

We now consider a scenario of practical interest, schematically shown in Figure 3.1 , with $\mathbf{B} = B\hat{x}$ and thus Larmor frequency $\omega = \gamma B$ and $\mathbf{F}_{\mathrm{max}} = F_{\mathrm{max}}\hat{z}$. We also assume that the relaxation Γ and the pumping Γ_{P} are considerably
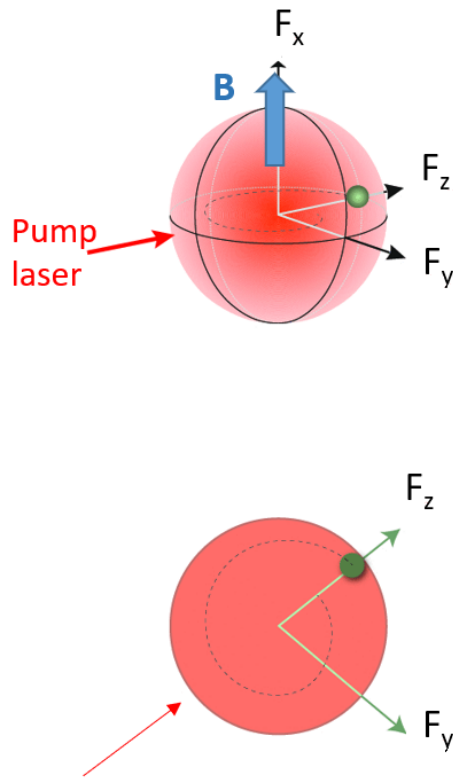
Figure 3.1.: **Spin dynamics in the presence of a bias magnetic field, spin relaxation and optical pumping** (top) Bloch sphere representation (bottom) Projection on the y-z plane.

smaller than ω_L, so that the spins precess by several cycles before relaxing. We can then approximate Equation 3.5 by replacing $-\Gamma_P(1 + \cos \Omega t)\mathbf{F}$ by its cycle-average, i.e. by $-\Gamma_P\mathbf{F}$, which can then be joined with $-\Gamma\mathbf{F}$ in a single term $-\tilde{\Gamma}\mathbf{F}$, where $\tilde{\Gamma}$ is the net relaxation rate $\tilde{\Gamma} \equiv \Gamma_P + \Gamma$. The Bloch equations then become

$$\frac{d}{dt}\mathbf{F} = -\omega\hat{x} \times \mathbf{F} - \tilde{\Gamma}\mathbf{F} + \Gamma_P F_{\max}(1 + \cos \Omega t)\hat{z}, \tag{3.6}$$

or

$$\frac{d}{dt}F_y = \omega F_z - \tilde{\Gamma}F_y \tag{3.7}$$

$$\frac{d}{dt}F_z = -\omega F_y - \tilde{\Gamma}F_z + \Gamma_P F_{\max}(1 + \cos \Omega t). \tag{3.8}$$

These can be represented in terms of the ladder operators

$$F_{\pm} \equiv F_y \pm iF_z, \tag{3.9}$$

as

$$\frac{d}{dt}F_+ = \omega(F_z - iF_y) - \tilde{\Gamma}(F_y + iF_z) + i\Gamma_P F_{\max}(1 + \cos \Omega t)$$

$$= -i\omega F_+ - F_+\tilde{\Gamma} + i\Gamma_P F_{\max}(1 + \cos \Omega t). \tag{3.10}$$

This is solved by the anzatz

$$F_+ = \lambda(t)e^{-i\omega_L t}e^{-t\tilde{\Gamma}}\Gamma_P F_{\max}, \tag{3.11}$$

if $\lambda(t)$ satisfies

$$\frac{d}{dt}\lambda(t) = (1 + \cos \Omega t)e^{i\omega_L t}e^{t\tilde{\Gamma}}. \tag{3.12}$$

This equation for λ is is solved by

$$\lambda(t) = \sum_{k=-1}^{+1} c_k \frac{e^{i(\omega_L + k\Omega)t}e^{t\tilde{\Gamma}}}{\tilde{\Gamma} + i(\omega_L + k\Omega)}, \tag{3.13}$$

with $c_0 = 1$ and $c_{\pm 1} = \frac{1}{2}$. Of the three terms in this solution, only the $k = -1$ term can be resonant. We make the rotating wave approximation and keep only this term to find

$$\lambda(t) \approx \frac{1}{2}\frac{e^{i(\omega_L - \Omega)t}e^{t\tilde{\Gamma}}}{\tilde{\Gamma} + i(\omega_L + k\Omega)}. \tag{3.14}$$

We can now compute F_z, which gives rise to the Faraday rotation signal [53]

$$
\begin{aligned}
F_z &= -\frac{i}{2}(F_+ - F_-) & (3.15)\\
&= \frac{\Gamma_{\mathrm{P}} F_{\max}}{2}\left[\frac{\tilde{\Gamma}}{(\Omega - \omega_L)^2 + \tilde{\Gamma}^2}\cos\Omega t + \frac{\Omega - \omega_L}{(\Omega - \omega_L)^2 + \tilde{\Gamma}^2}\sin\Omega t\right] & (3.16)\\
&\equiv \rho\cos\Omega t + \sigma\sin\Omega t & (3.17)
\end{aligned}
$$

where ρ and σ the components of the oscillating spin.

3.3. Atom-light interaction Hamiltonian

The measurement scheme of the main experiment in this thesis includes a polarized hot vapor probed by an off-resonant, linearly-polarized beam propagating in the z direction, as illustrated in Figure 3.2. Similar schemes have been studied in the context of cold atoms [54] and the dynamics of quantum non demolition measurement [55, 56].

The atom light interaction in such measurement schemes can be described with the Hamiltonian

$$
H_{\mathrm{int}} = H^{(0)} + H^{(1)} + H^{(2)}, \tag{3.18}
$$

with components

$$
\begin{aligned}
H^{(0)} &= \frac{2}{3}g\alpha^{(0)}S_0 N_A, & (3.19)\\
H^{(1)} &= g\alpha^{(1)}S_z F_z, & (3.20)\\
H^{(2)} &= g\alpha^{(2)}[\frac{1}{3}S_0 N_A + S_1(F_x^2 - F_y^2) + S_2(F_x F_y + F_y F x)]. & (3.21)
\end{aligned}
$$

Here $\alpha^{(i)}$, $i \in [0, 1, 2]$ are the scalar, vector and tensor components of the atomic polarizability, respectively and $g = \omega_0/(2\epsilon_0 V)$ is a form factor with atomic resonance frequency ω_0 and interaction volume V and N_A, the number of atoms.

For a more complete discussion on the atomic polarizability components and how they depend on the probe detuning, the interested reader may refer to works by the Mabuchi group [57, 58] or the Mitchell group [59] aimed at cold atom experiments, or for hot atoms (in which Doppler broadening is significant) in works by the Happer [15] and Romalis [60] groups. For the experimental conditions found in this thesis, only the term $H^{(1)}$ is relevant, and we write the interaction Hamiltonian as

$$
H_{\mathrm{int}} = GS_3 F_z, \tag{3.22}
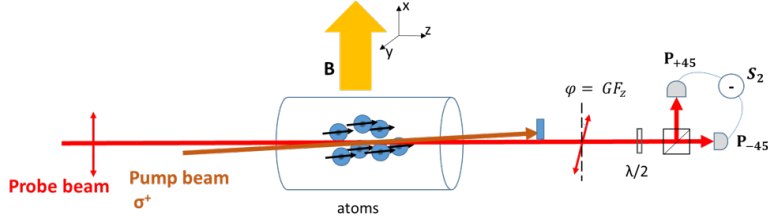$$

where $G = g\alpha^{(1)}$ the coupling constant.

Figure 3.2.: **Faraday rotation in the Bell Bloom magnetometer scheme.**
The polarization plane of the linearly polarized probe beam rotates
by an angle ϕ after the interaction with the polarized atomic vapor.

3.3.1. Faraday rotation

The atomic vapor shows a circular birefringence due to the F_z component, which
causes the rotation of polarization by an angle $\phi = GF_z$.

This is expressed in terms of the evolution of the S_1 and S_2 Stokes components
before and after the laser beam passes through the atomic cell as

$$
\begin{aligned}
S_1^{(\text{out})} &= S_1^{(\text{in})} \cos \phi - S_2^{(\text{in})} \sin \phi & (3.23) \\
S_2^{(\text{out})} &= S_2^{(\text{in})} \cos \phi + S_1^{(\text{in})} \sin \phi. & (3.24)
\end{aligned}
$$

Here we consider the probe laser beam linearly polarized along the x direction.
Therefore the S_1 Stokes parameter is the largest component of the polarization
and assuming a small angle ϕ, it is;

$$
S_1^{(\text{in})} \approx S_1^{(\text{out})}. \tag{3.25}
$$

In the small angle approximation, Equation 3.24 becomes

$$
S_2^{(\text{out})} \approx S_2^{(\text{in})} + S_1^{(\text{in})} \phi. \tag{3.26}
$$

Then the input-output relation for the detected Stokes component in this
scheme is [26]

$$
S_2^{(\text{out})} = S_2^{(\text{in})} + GS_1F_z. \tag{3.27}
$$

3.3.2. AC Stark shift and quantum back-action

The AC Stark shift is a well studied effect in optical magnetometry [61, 62, 63]
and various techniques have been implemented to reduce the impact it has on
the magnetic field measurement [64]. These include the use of linearly polarized

light, reducing the light intensity or tuning the laser to a frequency where the AC Stark shifts are minimized. The experimental geometry in which the propagation direction of the probe beam is orthogonal to the bias magnetic field (B_0) direction can also be employed. In such a configuration, the circular components of the electromagnetic field can introduce noise to the spin dynamics. It acts as a fictitious magnetic field adding in quadrature with the leading field [25]. In this section, we are interested in this mechanism as a source of quantum noise from the light acting back on the atoms.

The same interaction Hamiltonian (Equation 3.22) that was used to explain the Faraday rotation gives rise to the AC Stark shift too. In particular, the time evolution of the collective angular momentum operator $\mathbf{F}$ due to the Hamiltonian H_{int} is

$$\frac{d\mathbf{F}(t)}{dt} = \frac{1}{i\hbar}[\mathbf{F}(t), H_{\mathrm{int}}(t)]. \tag{3.28}$$

According angular momentum components commutation relation, the components of $\mathbf{F}$ perpendicular to the probing direction are the only ones affected as

$$\frac{d}{dt}F_x(t) = GS_3(t)F_y(t) \tag{3.29}$$

$$\frac{d}{dt}F_y(t) = GS_3(t)F_x(t), \tag{3.30}$$

while the longitudinal atomic magnetization remains constant

$$\frac{d}{dt}F_z(t) = 0. \tag{3.31}$$

For the experimental scheme of the Bell Bloom magnetometer in this thesis, where the probing is along the z direction, the evolution due to the AC Stark shift is equivalently written as

$$\frac{d}{dt}\mathbf{F}(t) = GS_3(t)\hat{z} \times \mathbf{F}(t). \tag{3.32}$$

Just as the interaction $H = -\mu_B g_F \mathbf{F} \cdot \mathbf{B}$ generates the Zeeman shift and the spin precession around the perpendicular magnetic field, this term can be treated as the evolution due to a magnetic field [65], in the direction parallel to the probe beam [48]. It is evident then that $S_3(t)$ can cause $\mathbf{F}$ to precess out of the plane perpendicular to the real magnetic field. In the experiment described in chapter 4, the probe is linearly polarized, so that $S_3(t)$ is zero on average. The fluctuations of $S_3(t)$ about zero, including quantum fluctuations, can nonetheless cause $\mathbf{F}$ to precess about $\hat{z}$, although the sense and magnitude of that precession will be

random. That is, noise in $S_3(t)$ can create noise in $\mathbf{F}$. This random effect on the measured system by the probe is *measurement back-action.*

Combining the Larmor precession in the presence of the magnetic field (Equation 3.2) with the effects of relaxation, optical pumping (Equation 3.3) and AC Stark shift (Equation 3.32), the evolution of the collective spin state operator $\mathbf{F}$ is

$$\frac{d}{dt}\mathbf{F}(t) = [-\gamma\mathbf{B}(t) + GS_3(t)\hat{z}] \times \mathbf{F}(t) - \Gamma\mathbf{F}(t) + P(t)[\hat{z}F_{\max} - \mathbf{F}(t)]. \quad (3.33)$$

This is the starting point in chapter 5 to describe the spin dynamics and develop a physical model for the noise properties of the magnetometer.

While this model contains all the physical effects required to understand the role of polarization squeezing and measurement back-action in the experiment, it also contains some important simplifications relative to the real spin system studied. These include the description of only one hyperfine component, whereas the real system has two, and treatment of the atomic vapor as homogeneous, whereas in the experiment the optical pumping and probing are performed with finite beams that will cause different regions of the cell to be pumped and probed differently. For this reason, we do not expect to make quantitative predictions with this model. Nonetheless, as will be shown in chapter 4 and chapter 5, it appears to describe well the experimental behaviour.

4

Squeezed Light Enhanced Magnetometer

[1] Optically-pumped magnetometers (OPMs) [17], in which an atomic spin ensemble is optically pumped [14] and its spin-dynamics optically detected, are a paradigmatic quantum sensing technology with applications ranging from geophysics [18] to medical diagnosis [66] to searches for physics beyond the standard model [67]. OPMs are also a useful proving ground to test sensitivity enhancement techniques that may some day be applied to atomic clocks [68], gyroscopes [69], and co-magnetometers [70, 71]. In these sensors two quantum systems – atoms and light – interact to produce the signal. Understanding and controlling the quantum noise in this interacting system is an outstanding challenge [72, 73, 29, 31].

At high atomic densities that give high OPM sensitivity, quantum noise of both atoms and light is important [17]. Measurement backaction, including the effect of probe quantum noise on the spin system, becomes important in such conditions [35], making it unclear whether squeezing of the probe light [8, 74, 75, 76], which reduces noise in one optical component while increasing it in another, can reduce total noise in a high-sensitivity OPM. In contrast to squeezed-light enhancement in low-density OPMs [28], high-density squeezed-light OPMs [30] have to date shown a trade-off of sensitivity vs. quantum noise reduction [77, 78], and a worsening of sensitivity due to probe squeezing [29].

To show that squeezing can indeed benefit a high-sensitivity OPM, we study a backaction evading measurement scheme based on Bell-Bloom (BB) optical pumping [52] and off-resonance probing. We model the quantum noise dynamics, including optical and spin quantum noise, and their interaction. We find that measurement backaction noise is shunted into a spin component that does not contribute to the signal. In this way the scheme almost fully evades measurement backaction noise, including that associated with squeezing. We predict and experimentally demonstrate that squeezing improves the sensitivity of the OPM above the response bandwidth of the magnetometer, without significantly

---

[1]This chapter is partially published in Phys. Rev. Lett. 127, 193601(2021) [33]

increasing noise in any part of the spectrum. Squeezing is also observed to improve the measurement bandwidth [79], i.e., the frequency range over which the sensitivity is within 3 dB of its best value.

Our sensor achieves sub-pT/$\sqrt{\text{Hz}}$ sensitivity to low-frequency finite fields, comparable to that of the best scalar OPMs implemented with mm-sized [80] vapor cells and far better than previous squeezed-light enhanced OPMs [28, 29, 30]. The backaction evasion scheme is compatible with sub-fT/$\sqrt{\text{Hz}}$ methods including high-density [18] and multi-pass [81] techniques, as well as with pulsed gradiometry [82, 83] and closed-loop [84] techniques for operation at Earth's field [85] and in unshielded environments [86]. The BB technique also gives a clear view of the relationships among different noise sources. The results provide experimental input to the much-discussed question of whether squeezing techniques can, in practice, improve the performance of atomic sensors [72, 73, 29, 78, 87].

The experimental setup and coordinate system are shown in Figure 4.1. Isotopically enriched ^{87}Rb vapor and 100 Torr of N_2 buffer gas are contained in a cell with interior length 3 cm. The cell, within a ceramic oven, is maintained by intermittent Joule heating at 105 °C to create a ^{87}Rb density of 8.2×10^{12} atoms/cm^3 and an optical transmission of about 70 % for probe light blue detuned by 20 GHz from the D_1 line. The cell and heater sit at the centre of four layers of cylindrical mu-metal shielding with cylindrical coils to control the bias field components B_α and gradients $\partial B_\alpha / \partial_z$, $\alpha \in \{x, y, z\}$. A 500 µW pump beam from a distributed Bragg reflector (DBR) laser, circularly polarized and current-tunable within the D_1 line at 795 nm, propagates through the cell at a small angle from the z axis. An extended cavity diode laser at 795 nm is stabilized 20 GHz to the blue from the ^{87}Rb D_1 line with a fiber interferometer [88] and frequency-doubled to produce violet light at 397.4 nm (Toptica TA-SHG 110). The violet light is mode-cleaned in a polarization-maintaining fiber and then pumps a sub-threshold optical parametric oscillator to produce vertically-polarized squeezed vacuum at the laser fundamental frequency, as described in [37]. The squeezed vacuum is combined on a polarizing beam-splitter with a mode-matched, horizontally-polarized "local oscillator" (LO) laser beam at 795 nm to produce the polarization-squeezed probe. The relative phase between LO and squeezed vacuum is controlled by a piezo-electric actuator and active feedback using the broadband noise level of the signal as the system variable [37]. In both coherent and squeezed-light probing, a 400 µW beam is detected with a shot-noise-limited balanced polarimeter after the cell. The system is operated as a BB OPM at a finite field B = 4.3 µT by applying a low-noise current through the coils (current source Twinleaf CSUA300); gradients and other bias components are nulled. The DBR laser's current is square modulated with duty cycle 10% at angular frequency $\Omega = \omega_L \approx 2\pi \times 30$ kHz, equal to the angular Larmor frequency ω_L. The effect of the current modulation is to bring the laser frequency into optical resonance with the $F = 1 \rightarrow F' = 1, 2$
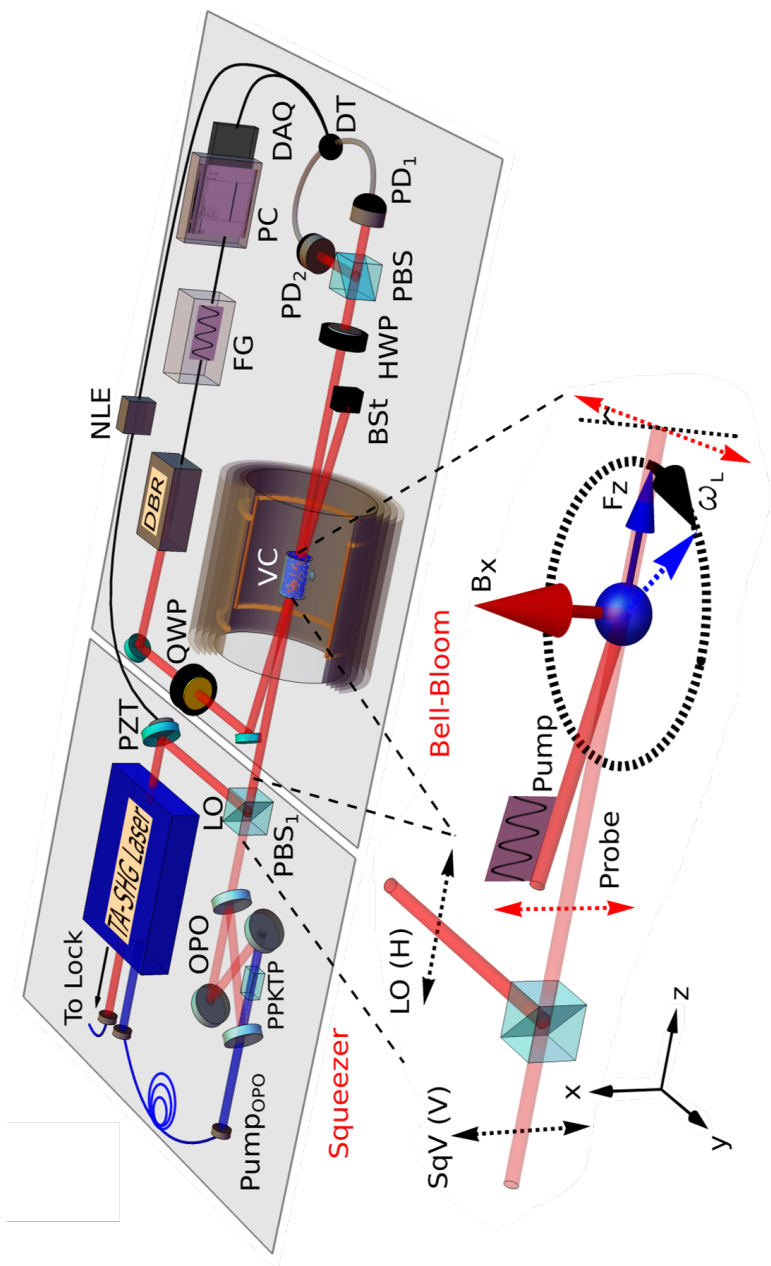
Figure 4.1.: **Squeezed-light Bell Bloom OPM**. Experimental setup. TA-SHG, Tapered Amplified Second Harmonic Generator; OPO, Optical Parametric Oscillator; PPKTP, Nonlinear crystal; LO, Local Oscillator; PBS, Polarizing Beam Splitter; QWP - Quarter Wave-plate; VC - Vapor Cell; BSt - Beam stopper; HWP - Half Wave-Plate; PD - Photodiode; DTIA - Differential Transimpedance Amplifier; DAQ - Data Acquisition; FG - Function Generator; NLE - Noise Lock Electronics.

35
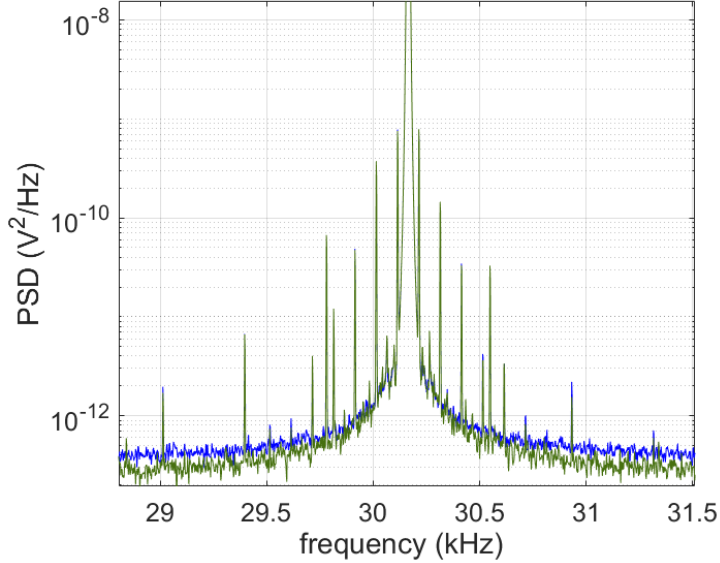
Figure 4.2.: **Squeezed-light Bell-Bloom OPM. Power Spectral Density (PSD).** Power spectrum of the BB signal for coherent and squeezed-light around the Larmor frequency. The spectra are averages of 100 measurements, each one with duration of 0.5 s.

transitions once per modulation cycle. In each measurement cycle, the modulated pumping is maintained for 0.5 s. The resulting spin dynamics are observed as paramagnetic Faraday rotation of the probe beam. Under continuous, modulated pumping, the polarimeter signal oscillates with frequency Ω, and shows noise from both spin projection noise and photon shot noise [89]. The role of quantum noise can be qualitatively understood from a Bloch equation model described in detail in chapter 5. The spins evolve according to the stochastic differential equation $d\mathbf{F}/dt = \mathbf{V} + \mathbf{N}$, where $\mathbf{F}$ is the collective atomic spin vector, $\mathbf{N}$ is a Langevin noise term and

$$\mathbf{V} = -\gamma B \hat{x} \times \mathbf{F} - \Gamma \mathbf{F} + P(\hat{z} F_{\max} - \mathbf{F}) \qquad (4.1)$$

is the drift rate (chapter 5). Here γ is the gyromagnetic ratio of ^{87}Rb, $\Gamma = 1/T_2$ is the transverse relaxation rate, P is the optical pumping rate, $F_{\max} = N_A F$ is the maximum possible polarization, and N_A is the atom number. Equation 4.1 describes a spin oscillator with resonant frequency $\omega_L \equiv \gamma B = \gamma(B^{(0)} + B^{(1)})$, where $B^{(0)}$ is the time-average of B and $|B^{(1)}| \ll |B^{(0)}|$.

In the small-angle approximation appropriate here, the Faraday rotation signal can be written as [26] :

$$S_2 = GS_1F_z + N_{S_2},\tag{4.2}$$

where S_α, $\alpha \in \{1, 2, 3\}$ indicate Stokes parameters at the output of the cell, G is a coupling constant, and N_{S_2} is the polarization noise of the detected Stokes component, a manifestation of quantum vacuum fluctuations [8].

The oscillating spins and signal can be described in terms of slowly-varying quadratures ρ, σ, u, v via $F_z(t) = \rho \cos \Omega t + \sigma \sin \Omega t$ and $S_2(t) = u \cos \Omega t + v \sin \Omega t$. The in-phase ($u$) and quadrature ($v$) components are obtained by digital lock-in detection of the signal S_2. We set $\Omega = \gamma B^{(0)}$ to maximize u, at which point v is linear in $B^{(1)}$. Small changes in B produce a linear change in the phase of the S_2 oscillation, such that $\tilde{v}(\omega) = R(\omega)\tilde{B}(\omega)$, where a tilde indicates a Fourier amplitude,

$$R(\omega) \quad \equiv \quad \frac{\gamma\langle u\rangle}{-i\omega + \Delta\omega},\tag{4.3}$$

is the magnetic response, $\langle u\rangle = GS_1^{(\text{in})}\langle\rho\rangle$ is the signal amplitude, $\langle\rho\rangle$ is the equilibrium spin polarization, and $\Delta\omega \equiv \Gamma + \bar{P}$ is the response bandwidth, where $\bar{P}$ is the cycle-average of P. We compute the single-sided power spectral density of this signal, as $\mathcal{S}_v(\omega) \equiv |\mathcal{F}[N_v]|^2$, where $\mathcal{F}$ is the discrete Fourier transform implemented with a Hann window.

4.1. Quantum noise

The spin noise is

$$\mathbf{N} \quad = \quad \mathbf{N}_F + GS_3\hat{z} \times \mathbf{F},\tag{4.4}$$

where $\mathbf{N}_F$ accounts for the noise introduced by pumping and relaxation, as required by the fluctuation-dissipation theorem, $GS_3\hat{z}$ is the effective field produced by ac-Stark shifts [90] due to the probe, and is effectively white.

The three quantum noise sources affect differently the measurement. The azimuthal projection of $\mathbf{N}_F$ contributes directly to the spin angle θ, just as would a magnetic field, and thus with efficiency $\propto R(\omega)$. In contrast, N_{S_2} is white noise, unrelated to the atomic response. Spectra of these two noise sources are shown in Figure 4.3(a) along with the experimentally measured magnetic response for comparison. The weak noise term $GS_3\hat{z}$ competes with the stronger $|B|\hat{x}$ in directing the spin precession, such that only its Ω-resonant component has a first-order effect. Said effect only alters the F_x component, which has no first
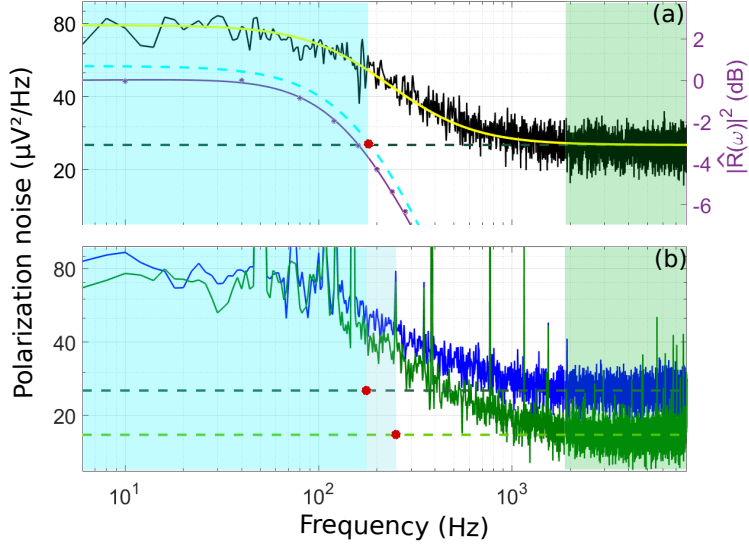
Figure 4.3.: **Polarization rotation noise after demodulation. (a) Spin noise for unpolarized atoms.** We fit the spectrum (black) with a model function of Equation 5.33 to estimate the response bandwidth, the photon shot noise (dashed green line) and the low frequency spin projection noise. Subtracting the constant shot noise contribution from the fitted combined noise (yellow) we infer the spin projection noise curve in the unpolarized state probed (dashed cyan). These noise levels define the spin projection noise (cyan) and photon shot noise (green) limited areas and the intermediate transition region (white). Purple dots and curve show, on the right axis, the measured normalized frequency response $|\hat{R}(\omega)|^2$ to an applied B_x modulation, and its fit with Equation 4.3 with best fit parameter $\Delta\omega = 170$ Hz. **(b) Magnetometer noise for polarized atoms.** With $500\,\mu$W of pump power, the noise spectrum of the magnetometer shows a very similar behaviour to the unpolarized spectrum and apart from the technical noise peaks at the power-line frequency and harmonics, quantum noise is dominant. At high frequencies, the noise level is reduced by 1.9 dB for squeezed-light (green), with respect to the coherent (blue) probing. The dashed lines and the red dots depict estimates of photon shot noise level and cross-over frequencies when the squeezer is on and off, respectively.

order effect on the signal S_2. As a result, this BB magnetometer is backaction evading [79, 91, 92]. Most importantly for the use of squeezed light, there is no deleterious effect from using squeezing to reduce the noise in S_2. While this necessarily increases the noise in S_3, said increase has no effect on the signal. Two potential benefits of optical squeezing are thus clear: it will reduce the noise for higher frequencies, and increase the frequency at which the noise $S_v(\omega)$ transitions from spin-noise dominated to photon shot-noise dominated. As we describe below, this improves both high-frequency sensitivity and measurement bandwidth of this quantum-noise-limited sensor.

4.2. Equivalent magnetic noise spectrum

The calculation of magnetic sensitivity requires the above noise contributions to be normalized by the magnetic response. The latter is shown experimentally in Figure 4.3(a), and via the BB noise model (chapter 5) to have a characteristic roll-off described by a Lorentzian $\mathcal{L}(\omega) = (\Delta\omega)^2/(\omega^2 + (\Delta\omega)^2)$ [79]. The magnetic noise density is then

$$
\begin{aligned}
\mathcal{S}_B(\omega) &= \mathcal{S}_v(\omega)|R(\omega)|^{-2} \\
&= \frac{\Delta\omega^2}{\gamma^2\langle u\rangle^2}\left(\mathcal{S}_\sigma + \frac{1}{\mathcal{L}(\omega)}\mathcal{S}_{N_{S_2}}\right),
\end{aligned}
\tag{4.5}
$$

where $\mathcal{S}_\sigma$ and $\mathcal{S}_{N_{S_2}}$ are the noise spectral densities of the quadrature components of F and N_{S_2}, respectively, and are frequency-independent. $\mathcal{S}_B(\omega)$ is nearly constant in the spin projection noise limited region and increases quadratically with frequency to double the low-frequency value at $\omega_{3\,\mathrm{dB}} \equiv \Delta\omega\sqrt{\mathcal{S}_\sigma/\mathcal{S}_{N_{S_2}} + 1}$. This frequency defines the $3\,\mathrm{dB}$ measurement bandwidth and grows with decreasing $\mathcal{S}_{N_{S_2}}$.

To demonstrate these advantages, we implement continuous-wave squeezed-light probing of the quantum-noise-limited BB OPM by using the experimental setup shown in Figure 4.1. As already described, the resulting optical beam is horizontally polarized with squeezed fluctuations in the diagonal basis, i.e., squeezed in S_2. For an OPO pump power of $40.6\,\mathrm{mW}$ the generated polarization squeezing is at $2.4\,\mathrm{dB}$ before the cell, as measured from the PSD of the signal from an auxiliary balanced polarimeter. Because of $30\,\%$ absorption losses, $1.9\,\mathrm{dB}$ of squeezing is observed in the PSD of both the BB polarimeter signal, shown in Figure 4.2, and the demodulated quadrature component, shown in Figure 4.3(b).

We compute the experimental sensitivity following prior work on BB magnetometers [93, 94, 80], as

$$
\mathcal{S}_B(\omega) = \left(\frac{dv}{dB}\right)^{-2}\frac{\mathcal{S}_v(\omega)}{|\hat{R}(\omega)|^2},
\tag{4.6}
$$

where $\mathcal{S}_v(\omega)$ is the observed noise in the lock-in quadrature component v, dv/dB is the slope of the quadrature signal and $|\hat{R}(\omega)|^2 \equiv |R(\omega)/R(0)|^2$ is the normalized frequency response of the spins to a modulation of the field B_x, shown in Figure 4.3(b), Figure 6.9 and Figure 4.3(a) respectively. Measurement of the magnetometer frequency response to a fixed amplitude sine wave magnetic field modulation in the range of $10\,\text{Hz}$ to $2.4\,\text{kHz}$ is used to experimentally determine $|R(\omega)|^2$.

4.3. Sensitivity and measurement bandwidth with squeezed-light probing

Turning on the squeezer causes $\mathcal{S}_{N_{S_2}}$ to drop to ξ^2 times its coherent-state value $\mathcal{S}_{N_{S_2}}^{\text{SQL}}$, where ξ^2 is the squeezing parameter [95, 96]. The predicted magnetic power spectral density is then

$$
\begin{aligned}
\mathcal{S}_B(\omega) &= \frac{\Delta\omega^2}{\gamma^2\langle u\rangle^2}[\mathcal{S}_\sigma + \frac{\xi^2}{\mathcal{L}(\omega)}\mathcal{S}_{N_{S_2}}^{\text{SQL}}] \\
&= \mathcal{S}_B^{\text{SQL}}(\omega)\frac{1 + \mathcal{L}(\omega)\xi^2\zeta^{-2}}{1 + \mathcal{L}(\omega)\zeta^{-2}},
\end{aligned} \tag{4.7}
$$

where $\zeta^2 \equiv \mathcal{S}_\sigma/\mathcal{S}_{N_{S_2}}^{\text{SQL}}$.

The enhancement due to squeezing is evident in the high frequency part of the experimental spectrum, shown in Figure 4.4. At the detection frequency of $490\,\text{Hz}$, a polarization squeezing of $1.9\,\text{dB}$ results in a $17\,\%$ quantum enhancement of magnetic sensitivity, from $600\,\text{fT}/\sqrt{\text{Hz}}$ down to $500\,\text{fT}/\sqrt{\text{Hz}}$. As seen in Figure 4.4, squeezing does not add noise to any region of the spectrum. This is a direct experimental demonstration that the BB technique evades backaction associated with the anti-squeezed S_3 component.

Squeezed-light probing also increases the $3\,\text{dB}$ measurement bandwidth [79]. For the data presented in Figure 4.4, the original measurement bandwidth of $275\,\text{Hz}$ is already higher than the response bandwidth $\Delta\omega = 170\,\text{Hz}$ and it is further increased to $320\,\text{Hz}$, with about $15\,\%$ of quantum enhancement. This result agrees with the predicted improved $3\,\text{dB}$ measurement bandwidth estimated via

$$
\omega_{3\,\text{dB}}^{\text{sq}} = \omega_{3\,\text{dB}}^{\text{SQL}}\sqrt{\frac{1 + \zeta^2\xi^{-2}}{1 + \zeta^2}} \tag{4.8}
$$

The quantum advantages demonstrated here are limited by the squeezing produced by our OPO [37], and by probe transmission losses. Optical losses for the
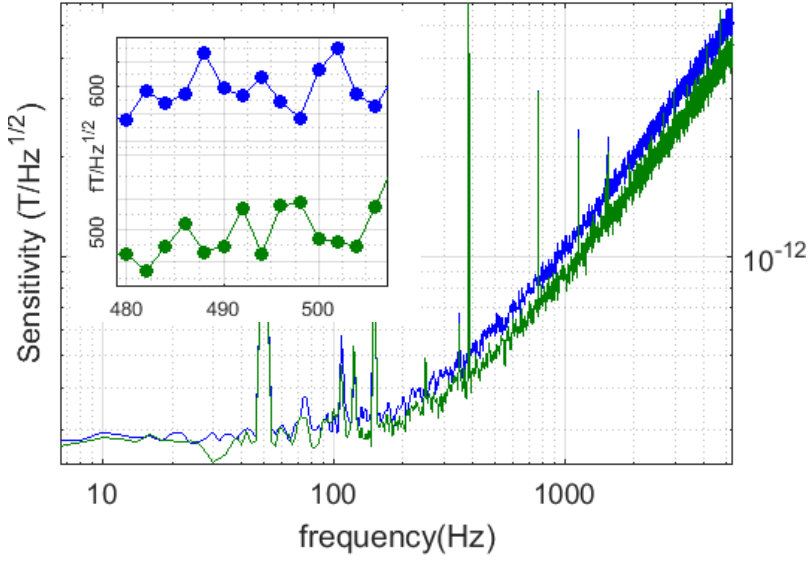
Figure 4.4.: **Magnetic Sensitivity.** Sensitivity spectra for BB magnetometer probed with coherent (blue) and squeezed light (green). All data acquired with $P_{\mathrm{probe}} = 400\,\mu\mathrm{W}$, $P_{\mathrm{pump}} = 500\,\mu\mathrm{W}$, $T = 105\,°\mathrm{C}$, $n = 8.2 \times 10^{12}\,\mathrm{atoms/cm^3}$, $B_0 = 4.3\,\mu\mathrm{T}$, $f_{\mathrm{mod}} = 30.164\,\mathrm{kHz}$. Polarization squeezing was $2.4\,\mathrm{dB}$ before the atomic cell and $1.9\,\mathrm{dB}$ at the detectors.

probe can in principle be made arbitrarily small without altering the other characteristics of the magnetometer, by increasing the probe detuning while boosting the probe power to keep constant the probe power broadening. More recent OPO designs [46, 44] have demonstrated up to 15 dB of squeezing.

In conclusion, in this chapter we have demonstrated that a polarization-squeezed probe can give both higher sensitivity and larger measurement bandwidth in a sensitive optically pumped magnetometer. In contrast to squeezed-light probing of optomechanical sensors such as gravitational wave detectors [97], the sensitivity advantage at high frequencies comes without the cost of increased backaction noise at low frequencies. As discussed in chapter 5, this occurs because QND measurement of a precessing spin system shunts backaction effects into the unmeasured spin degree of freedom [91], something not possible in a canonical system such as a mechanical oscillator [98]. Squeezed-light probing is compatible with and complementary to other methods to enhance sensitivity and bandwidth, including spin-exchange relaxation suppression [99], pulsed geometries [85, 86], multi-pass geometries [81], Kalman filtering [100] and closed-loop techniques [84].

5

Quantum Noise in Bell Bloom magnetometer

In this chapter we describe a quantum noise model for the Bell-Bloom magnetometer.[1] To keep the model reasonably simple while still retaining the essential physics, the model describes only a single spin population. In the experimental atomic system, operated outside of the SERF regime, the two hyperfine components precess with equal but opposite gyromagnetic ratios, contribute differently to the probe polarization rotation, and are resonant with the pump laser at different times in the pump laser's modulation cycle. Due to these differences, we do not expect to obtain quantitatively accurate sensitivity curves from this model. Nonetheless, we see that the model reproduces very accurately the shape of the observed BB noise and sensitivity curves, including the effect of squeezed light on sensitivity and measurement bandwidth. This gives us reason to believe that the model captures the essential physics of quantum noise in the BB magnetometer.

The model employs Bloch equations to describe the spin dynamics, in which the spin evolves as

$$\frac{d}{dt}\mathbf{F} \quad = \quad (-\gamma\mathbf{B} + GS_3\hat{z}) \times \mathbf{F} - \Gamma\mathbf{F} + P(\hat{z}F_{\max} - \mathbf{F}) + \mathbf{N}_F, \qquad (5.1)$$

where the first term describes precession under the magnetic field $\mathbf{B}$ and optically-induced effective field $GS_3\hat{z}$. $F_{\max} = N_A F$ is the maximum possible polarization, and F is the spin quantum number. The time-dependent optical pumping rate is P, and non-pumping relaxation, including spin relaxation due to atomic effects, i.e. spin-exchange and spin-destruction collisions, atomic diffusion and relaxation due to probing, i.e., power broadening, is described by the rate Γ. $\mathbf{N}_F$ is a Langevin term, which accounts for noise introduced by both kinds of relaxation. It is Gaussian white noise with covariance

$$\langle N_{F_i}(t)N_{F_j}(t') \rangle \quad = \quad 2\frac{F(F+1)}{3}N_A[\Gamma + P(t)]\delta_{ij}\delta(t - t')$$

---

[1]This chapter is partially published in the Supplemental Material of [33], `http://link.aps.org/supplemental/10.1103/PhysRevLett.127.193601`

$$\equiv \ G_{N_F}\delta_{ij}\delta(t-t').\tag{5.2}$$

as shown in the Appendix A.

The power spectral density is the Fourier transform of this correlation function

$$\mathcal{S}_{F_i}(f) \ = \ \int dt' \langle N_{F_i}(0)N_{F_j}(t')\rangle e^{-i2\pi ft'} = G_{N_F}\delta_{ij}.\tag{5.3}$$

5.1. Perturbative approach

Eq. (5.1) is not easy to solve exactly: it contains terms like $\gamma\mathbf{B}\times\mathbf{F}$ that are products of the time-dependent $\mathbf{B}$ (what we are trying to measure) and the time-dependent $\mathbf{F}$ (the spin that responds to it). In the scenario of interest, the time dependent quantities divide into strong, predictable ones and weak, noisy or to-be-measured ones. This motivates a perturbative treatment, in which we write $\mathbf{B} = \mathbf{B}^{(0)} + \alpha\mathbf{B}^{(1)}$ where $\mathbf{B}^{(1)}$ is a small unknown perturbation on top of the strong, known $\mathbf{B}^{(0)}$ and α is a perturbation parameter that we take to unity at the end. Similarly, we write $S_3 = \alpha S_3^{(1)}$ and $\mathbf{N}_F = \alpha\mathbf{N}_F^{(1)}$, and we expand $\mathbf{F}$, which depends on the preceding variables, as $\mathbf{F} = \mathbf{F}^{(0)} + \alpha\mathbf{F}^{(1)} + \ldots$. Eq. (5.1) now becomes

$$\frac{d}{dt}(\mathbf{F}^{(0)} + \alpha\mathbf{F}^{(1)} + \ldots) = -\gamma(\mathbf{B}^{(0)} + \alpha\mathbf{B}^{(1)})\times(\mathbf{F}^{(0)} + \alpha\mathbf{F}^{(1)} + \ldots)$$
$$+\alpha GS_3^{(1)}\hat{z}\times(\mathbf{F}^{(0)} + \alpha\mathbf{F}^{(1)} + \ldots) + \Gamma(\mathbf{F}^{(0)} + \alpha\mathbf{F}^{(1)} + \ldots)\tag{5.4}$$
$$+P[\hat{z}F_{\max} - (\mathbf{F}^{(0)} + \alpha\mathbf{F}^{(1)} + \ldots)] + \alpha\mathbf{N}_F^{(1)}.$$

We can formally solve the zero-th order case, i.e. with $\alpha = 0$. The solution is the $\mathbf{F}^{(0)}$ that satisfies

$$\frac{d}{dt}\mathbf{F}^{(0)} \ = \ -\gamma\mathbf{B}^{(0)}\times\mathbf{F}^{(0)} - \Gamma\mathbf{F}^{(0)} + P(\hat{z}F_{\max} - \mathbf{F}^{(0)}),\tag{5.5}$$

or

$$\left(\frac{d}{dt} + \gamma\mathbf{B}^{(0)}\times + \Gamma + P\right)\mathbf{F}^{(0)} \ = \ P\hat{z}F_{\max}.\tag{5.6}$$

The solution of this ordinary differential equation will simply be a function of time, not a stochastic process. It can be further used in the first order, i.e. $O(\alpha)^1$, dynamics, which is described by

$$\frac{d}{dt}\mathbf{F}^{(1)} \ = \ -\gamma(\mathbf{B}^{(1)}\times\mathbf{F}^{(0)} + \mathbf{B}^{(0)}\times\mathbf{F}^{(1)}) + GS_3\hat{z}\times\mathbf{F}^{(0)}$$

$$-\Gamma \mathbf{F}^{(1)} - P\mathbf{F}^{(1)} + \mathbf{N}_F^{(1)} \tag{5.7}$$

or

$$\left(\frac{d}{dt} + \gamma \mathbf{B}^{(0)} \times + \Gamma + P\right) \mathbf{F}^{(1)} \quad = \quad -\gamma \mathbf{B}^{(1)} \times \mathbf{F}^{(0)} + \mathbf{N}_F^{(1)} + GS_3\hat{z} \times \mathbf{F}^{(0)}. \tag{5.8}$$

Note that this equation is linear in the unknown $\mathbf{F}^{(1)}$.

The input light is polarized so that the Stokes parameter $\langle S_1 \rangle$ is maximum, and the readout Stokes parameter S_2 is given by

$$S_2 \quad = \quad GS_1F_z + N_{S_2}, \tag{5.9}$$

where N_{S_2} is the quantum noise in that polarization component. We note that S_3 is on average zero, but will have fluctuations that we describe by another Langevin term N_{S_3}, which has an uncertainty relation with respect to N_{S_2}.

We thus have five noise components represented here: three components of $\mathbf{N}_F$, plus N_{S_2} and N_{S_3}. We do not expect any of these to enter the signal in exactly the same way. We note, for example, that one component of $\mathbf{N}_F$ (and of $\mathbf{F}$) is out of the plane of precession, i.e., in the direction of $\mathbf{B}$, and does not contribute to the signal. Another component of $\mathbf{N}_F$ will be the radial component, i.e., parallel to $\mathbf{F}$, and thus contributing noise to the amplitude of the signal, while the remaining component of $\mathbf{N}_F$ will be the azimuthal component, i.e., normal to both $\mathbf{B}$ and $\mathbf{F}$, and thus adding noise to the angle of precession. This last one we can expect to look like magnetic signal and thus to be the most relevant atomic noise. As regards the optical noises, N_{S_2} will be a white noise that directly enters the measurement record, while N_{S_3} will enter only to the degree that it can perturb the atomic spin precession.

5.2. Bell-Bloom scenario - harmonic drive

We now specialize to the BB scenario. We take $\mathbf{B}^{(0)} = |\mathbf{B}^{(0)}|\hat{x}$ (a constant), and we assume that the pumping $P(t)$ is periodic and close to resonance with the Larmor precession, with an amplitude that is constant over time. Without loss of generality we choose the time origin such that $\int_0^{2\pi/\Omega} P(t)\exp[i\Omega t]dt$ is positive real, meaning that $P(t)$ is in some sense centered on $\Omega t = 0, 2\pi, 4\pi, \ldots$. Because $\mathbf{B}^{(0)}$ is along the $\hat{x}$ direction and the pumping is in the $\hat{z}$ direction, $\mathbf{F}^{(0)}$ will be in the y–z plane. Remembering that the measured component is F_z, we can now see that the S_3 term will make no zero-th order or first-order contribution to the signal. From Eq. (5.7), its contribution to $\mathbf{F}^{(1)}$ is $\propto \hat{z} \times \mathbf{F}^{(0)}$, which is along the $\hat{x}$ direction, i.e. the component of $\mathbf{F}^{(1)}$ that is not measured. For this reason, we can drop this term from here on.

Similarly, the different components of $\mathbf{B}^{(1)}$, the perturbation to the field, have a different effects: The $\hat{x}$ component increases the magnitude of $\mathbf{B}$ in first order, and thus will change the precession rate. The $\hat{y}$ and $\hat{z}$ components will (in first order) only tip the axis of the precession, which introduces in first order an oscillating F_x component. But again, since F_x is not measured, this has no measurable first-order effect. All of which is summarized in the statement that the BB OPM is a scalar magnetometer, sensitive only the magnitude of the field, which in first order involves only the bias $\mathbf{B}^{(0)}$ and the component of $\mathbf{B}^{(1)}$ along $\mathbf{B}^{(0)}$. For this reason, we will consider from here on only $B_x^{(1)}$.

5.2.1. Rotating frame

We assume the system has a resonance that is of reasonably high Q factor, which is to say that relaxation and pumping effects are not strong during one cycle, and forces that are resonant can accumulate over several cycles. It is usual in such scenarios to describe the dynamics in a rotating frame, and to apply the rotating wave approximation. Here we define the frame rotating at Ω, the angular frequency of the drive. Given a vector $\mathbf{X}(t)$, the rotating-frame expression of $\mathbf{X}$ is $X_+ = (iX_y + X_z)\exp[i\Omega t]$. It will also be useful to have the cycle-averaged version

$$\langle X_+ \rangle_{\mathrm{cyc}}(t) \quad \equiv \quad \frac{\Omega}{2\pi} \int_{t-\pi/\Omega}^{t+\pi/\Omega} [iX_y(t') + X_z(t')] \exp[i\Omega t']\, dt'.$$

$$(5.10)$$

The spin itself, for example, is described by $F_+ = (iF_y + F_z)\exp[i\Omega t]$, with the consequence that

$$F_z \quad = \quad \mathcal{R}[F_+ e^{-i\Omega t}] = \mathcal{R}[F_+]\cos\Omega t + \mathcal{I}[F_+]\sin\Omega t \tag{5.11}$$

$$F_y \quad = \quad \mathcal{I}[F_+ e^{-i\Omega t}] = -\mathcal{R}[F_+]\sin\Omega t + \mathcal{I}[F_+]\cos\Omega t. \tag{5.12}$$

We note that in this representation

$$\hat{x} \times (\hat{y}F_y + \hat{z}F_z) \quad = \quad -\hat{y}F_z + \hat{z}F_y \tag{5.13}$$

is accomplished by $F_z \to F_y$ and $F_y \to -F_z$, which is the same as $F_+ \to -iF_+$. From the product rule

$$\frac{d}{dt}[F_+ e^{-i\Omega t}] \quad = \quad \left(\frac{d}{dt}F_+ - i\Omega F_+\right) e^{-i\Omega t} \tag{5.14}$$

we see that the time derivative in the rotating frame is given by $d/dt \to d/dt - i\Omega$.

The torque produced by a field $\mathbf{B}$ along the $\hat{x}$ direction can be written

$$
\begin{aligned}
\mathbf{T} &\equiv \gamma \mathbf{B} \times \mathbf{F} \\
&= \gamma |B| \hat{x} \times \{\hat{y}\mathcal{I}(F_+ \exp[-i\Omega t]) + \hat{z}\mathcal{R}(F_+ \exp[-i\Omega t])\} \\
&= \gamma |B| \{\hat{z}\mathcal{I}(F_+ \exp[-i\Omega t]) - \hat{y}\mathcal{R}(F_+ \exp[-i\Omega t])\} \\
&= \gamma |B| \{\hat{z}(\mathcal{I}[F_+]\cos\Omega t - \mathcal{R}[F_+]\sin\Omega t) \\
&\quad\ -\hat{y}(\mathcal{R}[F_+]\cos\Omega t + \mathcal{I}[F_+]\sin\Omega t), \}
\end{aligned}
\tag{5.15}
$$

so that

$$
\begin{aligned}
\langle T_+ \rangle_{\text{cyc}}(t) &= \frac{\Omega}{2\pi} \int_{t-\pi/\Omega}^{t+\pi/\Omega} [iT_y(t') + T_z(t')]e^{i\Omega t'} dt' \\
&= \gamma |\bar{B}| \frac{1}{2}(\mathcal{I}[F_+] - i\mathcal{R}[F_+] - i\mathcal{R}[F_+] + \mathcal{I}[F_+]) \\
&= \gamma |\bar{B}|(\mathcal{I}[F_+] - i\mathcal{R}[F_+]) \\
&= \gamma |\bar{B}|(-iF_+),
\end{aligned}
\tag{5.16}
$$

where $\bar{B} = \frac{\Omega}{2\pi}\int_{t-\pi/\Omega}^{t+\pi/\Omega} B(t')\, dt'$ is the cycle-averaged field strength. Eq. (5.16) fits our expectations; it describes a contribution to the precession rate.

5.2.2. Demodulation

Supposing we have a signal Y_+, which is in general complex. In the "lab frame," this is

$$
Y = \mathcal{R}[Y_+]\cos\Omega t + \mathcal{I}[Y_+]\sin\Omega t,
\tag{5.17}
$$

where $\mathcal{R}[Y_+]$ and $\mathcal{I}[Y_+]$ the in-phase and quadrature components respectively.

5.2.3. Order zero

We want the steady-state solution to Eq. (5.6), i.e. with $dF_+/dt \to 0$. For the representation of the pump, the cycle-averaged value is appropriate, and simpler than the general form. We use this to define an effective pump rate P_+:

$$
\langle P_+ \rangle_{\text{cyc}} = \frac{\Omega}{2\pi} \int_{t-\pi/\Omega}^{t+\pi/\Omega} P(t')e^{i\Omega t'}\, dt' \equiv P_+.
\tag{5.18}
$$

As in the lab frame, P_+ in the rotating frame can also be assumed real without loss of generality. We note that while P_+ is relevant for describing the forcing

effect of the drive, the relaxation effects, including decay rate and noise, concern rather the cycle-averaged mean pump

$$\langle P \rangle_{\text{cyc}} \quad = \quad \frac{\Omega}{2\pi} \int_{t-\pi/\Omega}^{t+\pi/\Omega} P(t')\, dt' \equiv \bar{P}. \tag{5.19}$$

Using these rotating-frame representations, we transform Eq. (5.6) into a simple algebraic equation:

$$(-i\Omega - i\gamma|B^{(0)}| + \Gamma + \bar{P})F_{+}^{(0)} \quad = \quad P_{+}F_{\text{max}}, \tag{5.20}$$

with solution

$$F_{+}^{(0)} \quad = \quad \frac{P_{+}F_{\text{max}}}{-i\Omega - i\gamma|B^{(0)}| + \Gamma + \bar{P}}. \tag{5.21}$$

We note that $\gamma < 0$, and that $-\gamma|B^{(0)}| \equiv \omega_{L}^{(0)}$, the Larmor (angular) frequency to zero order, so that

$$F_{+}^{(0)} \quad = \quad \frac{P_{+}F_{\text{max}}}{i(\omega_{L}^{(0)} - \Omega) + \Gamma + \bar{P}}. \tag{5.22}$$

This describes a Lorentzian resonance that saturates, with the effective linewidth $\Gamma + \bar{P}$ increasing in such a way that the polarization $F_{\text{max}}P_{+}/\bar{P} \leqslant F_{\text{max}}$ is never exceeded.

5.2.4. Order one

We now translate Eq. (5.8) to the rotating-frame picture. This time, we must keep the time derivative term dF_{+}/dt. We find

$$\left(\frac{d}{dt} + i(\omega_{L}^{(0)} - \Omega) + \Gamma + \bar{P} \right) F_{+}^{(1)} \quad = \quad i\gamma \bar{B}^{(1)} F_{+}^{(0)} + N_{F_{+}}. \tag{5.23}$$

This is a Langevin equation, because of the noise term $N_{F_{+}}$, and also it contains the unknown $B^{(1)}$, which depends on time. The equation has real and imaginary parts, which are coupled. In the demodulation, only the imaginary part, corresponding to the quadrature component, is used to infer the field, so we separate the real and imaginary parts

$$\begin{pmatrix} \frac{d}{dt} + \Gamma + \bar{P} & -(\omega_{L}^{(0)} - \Omega) \\ \omega_{L}^{(0)} - \Omega & \frac{d}{dt} + \Gamma + \bar{P} \end{pmatrix} \begin{pmatrix} \mathcal{R}[F_{+}^{(1)}] \\ \mathcal{I}[F_{+}^{(1)}] \end{pmatrix} = \begin{pmatrix} \mathcal{R}[N_{F_{+}}] - \gamma\bar{B}^{(1)}\mathcal{I}[F_{+}^{(0)}] \\ \gamma\bar{B}^{(1)}\mathcal{R}[F_{+}^{(0)}] + \mathcal{I}[N_{F_{+}}] \end{pmatrix}.$$

$$(5.24)$$

We can solve this in the Fourier domain taking ω as the frequency variable of the Fourier spectrum (note that this is different from ω_L and from Ω, which are constants), $d/dt \rightarrow -i\omega$, at which point we have

$$\begin{pmatrix} -i\omega + \Gamma + \bar{P} & -(\omega_L^{(0)} - \Omega) \\ \omega_L^{(0)} - \Omega & -i\omega + \Gamma + \bar{P} \end{pmatrix} \begin{pmatrix} \mathcal{R}[F_+^{(1)}](\omega) \\ \mathcal{I}[F_+^{(1)}](\omega) \end{pmatrix} = \begin{pmatrix} \mathcal{R}[N_{F_+}](\omega) - \gamma\bar{B}^{(1)}(\omega)\mathcal{I}[F_+^{(0)}] \\ \gamma\bar{B}^{(1)}(\omega)F_+^{(0)} + \mathcal{I}[N_{F_+}](\omega) \end{pmatrix}$$

with solution

$$\mathcal{I}[F_+^{(1)}](\omega) = \frac{[\mathcal{I}[N_{F_+}](\omega) + \gamma\bar{B}^{(1)}(\omega)F_+^{(0)}](-i\omega + \Gamma + \bar{P})}{[-i(\omega - \omega_L^{(0)} + \Omega) + \Gamma + \bar{P}][-i(\omega + \omega_L^{(0)} - \Omega) + \Gamma + \bar{P}]}$$
$$- \frac{(\omega_L^{(0)} - \Omega)[\mathcal{R}[N_{F_+}](\omega) - \gamma\bar{B}^{(1)}(\omega)\mathcal{I}[F_+^{(0)}]]}{[-i(\omega - \omega_L^{(0)} + \Omega) + \Gamma + \bar{P}][-i(\omega + \omega_L^{(0)} - \Omega) + \Gamma + \bar{P}]}.$$
$$(5.25)$$

5.2.5. Resonant case

We focus now on the case of resonant excitation, i.e., $\Omega = \omega_L^{(0)}$, which gives maximum signal and is the natural operating point for the BB magnetometer. In these condition, the response of F_+ to the field perturbation $B^{(1)}(\omega)$ and to spin noise $\mathcal{I}[N_{F_+}](\omega)$ have the same frequency dependence since they enter in exactly the same way, i.e.

$$\frac{\partial \mathcal{I}[F_+^{(1)}]}{\partial \bar{B}^{(1)}} = \frac{\gamma F_+^{(0)}}{-i\omega + \Gamma + \bar{P}} \quad \text{and} \quad \frac{\partial S_2}{\partial \bar{B}^{(1)}} = \frac{GS_1\gamma F_+^{(0)}}{-i\omega + \Gamma + \bar{P}}. \tag{5.26}$$

Moreover, $\mathcal{I}[N_{F_+}](\omega)$ is constant, i.e. the noise is white. This is the basis for saying that the spin noise and response to the magnetic field are matched [79].

Furthermore, we find that $F_+^{(0)}$ reduces to:

$$F_+^{(0)} = \frac{P_+ F_{\text{max}}}{\Gamma + \bar{P}} \tag{5.27}$$

and

$$\mathcal{I}[F_+^{(1)}](\omega) = \frac{\mathcal{I}[N_{F_+}](\omega) + \gamma\bar{B}^{(1)}(\omega)F_+^{(0)}}{-i\omega + \Gamma + \bar{P}}. \tag{5.28}$$

5.2.6. Optical signal, responsivity and sensitivity

The optical signal S_2 is demodulated to obtain the quadrature component $S_2^{(Q)}$. Writing this in the frequency domain we have

$$S_2^{(Q)}(\omega) \quad = \quad \mathcal{I}[N_{S_2+}](\omega) + GS_1\mathcal{I}[F_+^{(1)}](\omega). \tag{5.29}$$

The responsivity to magnetic fields $\bar{B}^{(1)}$ is

$$R(\omega) \quad \equiv \quad \frac{\partial S_2^{(Q)}(\omega)}{\partial \bar{B}^{(1)}(\omega)} = \frac{GS_1\gamma F_+^{(0)}}{-i\omega + \Gamma + \bar{P}}, \tag{5.30}$$

such that

$$|R(\omega)|^2 \quad = \quad \frac{(GS_1\gamma F_+^{(0)})^2}{\omega^2 + (\Gamma + \bar{P})^2}. \tag{5.31}$$

To find the quantum noise contribution to $S_2^{(Q)}$, we use Eq. (5.28) in Eq. (5.29) and assume that technical noise contributions to S_{2+} and F_+ are negligible. Fluctuations of $\bar{B}^{(1)}$, which represent a possible signal, are not counted as noise. We thus have the noise amplitude

$$N_{S_2^{(Q)}}(\omega) \quad = \quad \mathcal{I}[N_{S_2+}](\omega) + \frac{GS_1}{-i\omega + \Gamma + \bar{P}}\mathcal{I}[N_{F_+}](\omega). \tag{5.32}$$

The two terms describe independent noise contributions, so that the noise power spectral density is

$$\mathcal{S}_{S_2^{(Q)}}(\omega) \quad = \quad \mathcal{S}_{\mathcal{I}[N_{S_2+}]}(\omega) + \frac{G^2S_1^2}{\omega^2 + (\Gamma + \bar{P})^2}\mathcal{S}_{\mathcal{I}[N_{F_+}]}(\omega). \tag{5.33}$$

Using the propagation of error formula, we get the magnetic power spectral density $\mathcal{S}_B(\omega)$, i.e. the square of the magnetic sensitivity.

$$\begin{aligned} \mathcal{S}_B(\omega) \quad &= \quad |R(\omega)|^{-2}|N_{S_2^{(Q)}}(\omega)|^2 \\ &= \quad \frac{S_{\mathcal{I}[N_{F_+}]}(\omega)}{(\gamma F_+^{(0)})^2} + \frac{\omega^2 + (\Gamma + \bar{P})^2}{(GS_1\gamma F_+^{(0)})^2}\mathcal{S}_{\mathcal{I}[N_{S_2+}]}(\omega). \end{aligned} \tag{5.34}$$

5.2.7. Simplified notation

To obtain the less cumbersome expressions used in chapter 4, we define the in-phase signal amplitude $\langle u \rangle \equiv GS_1F_+^{(0)}$, the magnetic resonance line width $\Delta\omega \equiv$

$\Gamma + \bar{P}$, and the line-shape function

$$\mathcal{L}(\omega) \quad \equiv \quad \frac{(\Gamma + \bar{P})^2}{\omega^2 + (\Gamma + \bar{P})^2}. \tag{5.35}$$

We can then express Eq. (5.31) as

$$|R(\omega)|^2 \quad = \quad \gamma^2 \frac{\langle u \rangle^2}{\Delta \omega^2} \mathcal{L}(\omega). \tag{5.36}$$

The signal noise spectrum is $\mathcal{S}_v(\omega) \equiv \mathcal{S}_{S^{(Q)}_2}(\omega)$, with an optical noise contribution $\mathcal{S}_{N_{S_2}} \equiv \mathcal{S}_{\mathcal{I}[N_{S_2+}]}(\omega)$. We note this is frequency independent, i.e. white noise. The noise in $\mathcal{I}[N_{F_+}]$ is similarly white, and it is convenient to define its contribution to the signal as

$$\mathcal{S}_\sigma \equiv \frac{G^2 S_1^2}{(\Gamma + \bar{P})^2} \mathcal{S}_{\mathcal{I}[N_{F_+}]}(\omega). \tag{5.37}$$

The signal noise spectrum is then

$$\mathcal{S}_v(\omega) = \mathcal{S}_{N_{S_2}} + \mathcal{L}(\omega) \mathcal{S}_\sigma. \tag{5.38}$$

Using Eq. (5.36) and Eq. (5.38) with the propagation of error formula we obtain the magnetic sensitivity in this notation:

$$\begin{aligned}
\mathcal{S}_B(\omega) \quad &= \quad |R(\omega)|^{-2} \mathcal{S}_v(\omega) \\
&= \quad \frac{\Delta \omega^2}{\gamma^2 \langle u \rangle^2} [\mathcal{S}_\sigma + \frac{1}{\mathcal{L}(\omega)} \mathcal{S}_{N_{S_2}}] \\
&= \quad \frac{1}{\gamma^2 \langle u \rangle^2} [\Delta \omega^2 \mathcal{S}_\sigma + (\omega^2 + \Delta \omega^2) \mathcal{S}_{N_{S_2}}],
\end{aligned} \tag{5.39}$$

c.f. Eq. (4.5).

In this chapter, we have calculated the noise spectrum and sensitivity of the quantum noise limited Bell-Bloom magnetometer, using a simplified model of the atomic dynamics in which only one hyperfine level is occupied. The model could be directly applied also to the electron spin, in scenarios for which that is the most relevant atomic variable. The dynamical model is linear in the spin variables, because it does not include the nonlinear effects that arise due to spin-exchange. It is nonetheless interesting to linearize about the noise- and signal-free solution, to obtain the dynamics of perturbations about this solution, because this fully separates the signal and noise influences on the system. We then use Fourier methods to solve this system and get analytic expressions for the response to the

B-field perturbations, spin noise, and photon shot noise. These are combined to give the noise spectrum and the sensitivity spectrum.

The results agree perfectly with expectations: the field response and spin noise spectrum are matched, and are that of a low-pass filter, while the shot noise is flat. The sensitivity (as an equivalent magnetic noise power) is flat at low frequencies and rises $\propto \omega^2$ at high frequencies, with the constant of proportionality being the ratio of shot noise PSD and magnetic/optical response. The cross-over between one type of behaviour and the other is a function of the both spin noise and photon shot noise powers.

6

Experimental setup

The experimental setup of the squeezed light enhanced magnetometer combines two parts; a squeezed light source and a Bell Bloom magnetometer. The squeezed light source [101] is a sub-threshold optical parametric oscillator based on spontaneous parametric down conversion. On the other hand, the magnetometer exploits the Bell Bloom excitation of Rb atoms. It is based on a pre-existing experimental apparatus used for spin noise spectroscopy [102].

The chapter describes the developments that enabled the transition from spin noise spectroscopy to magnetometry setup. The novelty is the introduction of a circularly polarized pump beam responsible for the optical pumping of the atomic ensemble. More details are given later on the software for the data acquisition and analysis of the magnetometer signal. The second section contains methods for characterization of the balanced detector for shot noise limited performance. The specifics for the operation of the squeezer are provided. In particular, we report the operational conditions for the second harmonic generation and polarization squeezing. The chapter concludes with a discussion of the quantum noise lock setup.

6.1. Bell Bloom magnetometer

The experimental setup is displayed in Figure 4.1. The magnetometer includes a 3 cm long cell with isotopically-enriched ^{87}Rb vapor and 100 Torr of N_2 buffer gas. The cell lies inside a ceramic oven used to increase the temperature up to 190 °C and thus ^{87}Rb vapor can reach density up to values of 1×10^{14} atoms/cm^3. The ceramic oven is surrounded by cylindrical coils used to apply the bias field components B_α and gradients $\partial B_\alpha/\partial_z$, $\alpha \in \{x, y, z\}$. The cell along with the oven and the coils structure sit in the center of the four layers of cylindrical mu-metal shielding.

To operate the setup as a Bell Bloom magnetometer, two light beams propagate through the atomic ensemble in the z direction. The 500 µW pump beam from a distributed Bragg reflector (DBR) laser is circularly polarized and current tunable

within the D_1 line at $795\,\text{nm}$. The $400\,\mu\text{W}$ probe beam is linearly polarized and blue-detuned by $20\,\text{GHz}$ from the D_1 line. It propagates along the z axis and detected with a shot-noise-limited balanced polarimeter.

A bias magnetic field is generated along the x direction when applying a precision current source (Twinleaf CSUA300). For the optical pumping, the DBR laser current is square modulated wit duty cycle 10% at angular frequency $\Omega \approx \omega_L \approx 2\pi \times 30\,\text{kHz}$, where ω_L is the angular Larmor frequency. The effect of the current modulation is to bring the pump laser frequency into optical resonance with the optical resonance with the $F = 1 \to F' = 1, 2$ transitions once per modulation cycle.

The spin dynamics is probed though the Faraday rotation of the linearly polarized probe beam. The polarimeter signal is oscillating at the Larmor precession frequency, driven by the frequency of the pump current modulation. The signal has a power spectral density resonant at the pumping frequency with the same amplitude for coherent and squeezed light probing. The settings for Faraday probing and frequency modulated optical pumping are the same for both the experiments presented in chapter 4 and chapter 7.

6.1.1. Heating process

The main component of the heating system is a V shaped structure made of AlN designed such to host the Rb cell [102]. Three pairs of Kapton heaters surfaces are in thermal contact with the interior surface of the oven, two of them in the bottom part and one on top. The heating circuit consists of a T-type thermocouple (CT-Z2-PFA-T2 from LabFacility) that monitors the oven's temperature just above the main body of the cell. Its output is sent as feedback to a PID digital temperature controller (Omega, CN 9111A) that switches on the relay to output 115VAC until the set temperature is reached. There is a Kapton heater accessible outside the oven, that is in series connected with the internal heaters. The AC voltage across it acts as the input to the rectifier circuit of Figure 6.3. The output of the rectifier circuit is a TTL signal that triggers the data acquisition.

During the operation of this setup at temperature higher than $120\,°\text{C}$, it has been noticed that Rb atoms accumulated at the stem, the coldest part of the cell. To raise the temperature of the stem, and thereby the vapor pressure in the cell, the oven structure has been adapted to accommodate a cubic ceramic structure devoted to temperature regulation of the stem part of the cell. This structure acts a stem oven since a fourth pair of Kapton heaters is attached on it. The heaters are operated on DC current ($\sim 5\,\text{A}$) applied with a voltage power supply ($12\,\text{V}$, triple power supply HM8040-3 from HAMEG instruments) until the temperature difference generated between the stem and the main part of the

Figure 6.1.: **Heater structure**
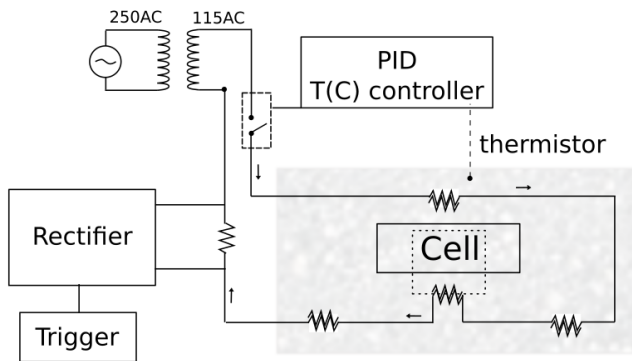(a) ceramic structure of the main part (b) stem oven

Figure 6.2.: **Heating circuit and acquisition triggering.** The heating system consists of a transformer, a PID temperature controller and a switch, 4 pairs of resistor loads attached to the ceramic structure, two on the sides one on the top of the cell and one on the stem oven. The resistors are overlapped, so that the current flow to be in opposite direction on the top compared to the bottom resistor. The overlap minimizes the generation of the magnetic field due to the heater. The rectifier circuit, in parallel with the outer resistor, provides a trigger for data acquisition when the heaters are off.
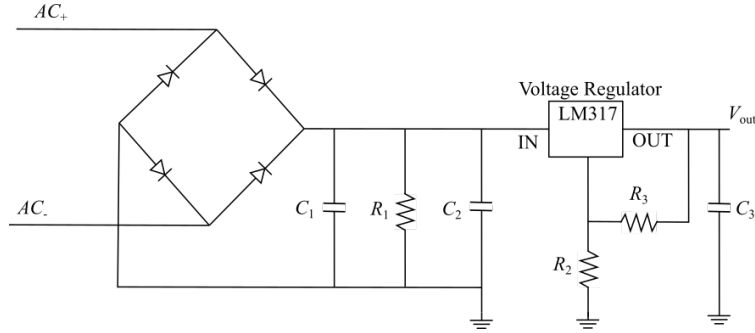
Figure 6.3.: **Rectifier circuit** The circuit performing the rectifying, filtering and voltage regulation of the AC signal to output a $V_{\text{out}} = 5\,\text{V}$ TTL signal. Components $C_1 = 10\,\text{µF}$, $C_2 = C_3 = 0.1\,\text{µF}$, $R_1 = 10\,\text{k}\Omega$, $R_2 = 320\,\text{k}\Omega$, $R_3 = 240\,\text{k}\Omega$.

cell is about $2\,^\circ\text{C}$. The temperature is monitored with a thermistor attached on the side of the stem oven.

From the start of my PhD, the ceramic V shaped oven was preexisting. The interested reader may find more details in the thesis chapter 3 of [102]. The modifications from that point on have been the adjustment of rectifier circuit and the addition of the stem oven. The addition of this part allows the potential operation of magnetometer setup at vapor density of $3.6 \times 10^{14}\,\text{cm}^{-3}$ corresponding to a temperature of $190\,^\circ\text{C}$.

6.1.2. Data acquisition

The acquisition is performed with the data acquisition card PCI4462 from National Instruments with sampling frequency of 204.8 kSamples/s and it is externally triggered with the output of the rectifier circuit. Each measurement cycle has a duration of 0.5 s. The TTL pulse duration depends on the set temperature. Indicatively, at set-point of $105\,^\circ\text{C}$, the heaters are off for 7 s intervals, which allows for 13 measurement cycles to be accommodated with no noise leaking from the turning on and off of the heater circuit. The number of measurement cycles is reduced to 10 for the set temperature of $120\,^\circ\text{C}$, the highest temperature employed in this work.

6.1.3. Spin noise spectroscopy

The spin noise spectroscopy is a technique to probe in a non destructive way the spin dynamics of the ^{87}Rb ensemble in thermal equilibrium. A more complete

discussion on the theory of the spin noise spectra are presented in [95] and the Supplemental material of [100] .

When a linearly polarized probe beam is recorded after the interaction with unpolarized ^{87}Rb vapor in the presence of the field B_x, the spin fluctuations of the ensemble are shown in the Faraday rotation signal. The power spectrum of the Faraday rotation signal shows a peak at the Larmor precession frequency ω_L. Fitting the specta with the Lorentzian function:

$$S(\omega) = S_{\mathrm{ph}} + S_{\mathrm{at}} \frac{(\Delta\omega)^2}{(\omega - \omega_L)^2 + (\Delta\omega)^2} \tag{6.1}$$

one can estimate the photon shot noise level S_{ph} and the linewidth (HWHM) $\Delta\omega$ and the amplitude of the atomic noise contribution S_{at} [95]. We typically perform spin noise spectroscopy before introducing the pump beam in the magnetometer in order to estimate the Larmor precession frequency of the atoms (ω_L) and set the optical pumping frequency $\Omega = \omega_L$.

6.1.4. Frequency modulation of the pump laser

The pump laser is a DBR monolithic diode laser of 795 nm (Photodigm, TO-8 header). Thorlabs drivers LDC202C and TED200C are used to control the injection current and temperature of the diode, respectively. The temperature and current settings allow tuning the wavelength to the Rb D1 resonance $F = 1 \rightarrow F' = 1, 2$, at temperature of 34 °C and current of 93 mA. The temperature calibration is 0.0058 nm/°C. The current calibration -1.72 GHz/mA is obtained from the linear fit slope of the data in Figure 6.4(a). The frequency modulation of the pump is performed by externally modulating the current of the driver LDC202C with a waveform generator (Siglent SDG1025). The optimal optical pumping scheme is the one that gives the highest signal amplitude with low technical noise. In this experiment, we accomplish this requirement when a pulse of duty cycle 10 % and amplitude 1.170 V is applied to the current driver. The resulting modulation for the pump detuning is schematically shown Figure 6.5. The mean power for the pump beam before the cell is measured to be 500 µW as the detuning is modulated with a sine pulse of the same amplitude.

6.1.5. Digital lock-in detection

Lock-in amplifiers are used to extract a signal of known frequency from a noisy background. The input signal V_{S} is mixed with a reference signal V_{ref}, oscillating at the frequency Ω and in phase with the input [103].

For this experiment, the digital lock-in amplification is designed in MatLAB and it is applied after the data acquisition. We record the signal, $V_{\mathrm{S}}(t_i)$, from the
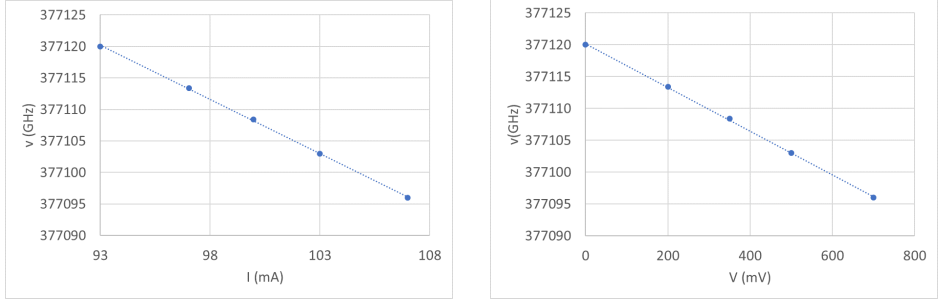
Figure 6.4.: **DBR laser calibration**
(a) detuning as a function of injection current with fixed temperature $(6.812\,\mathrm{k\Omega})$
$\mathrm{T} = 34\,°\mathrm{C}$ (b) detuning as a function of the waveform generator offset for the
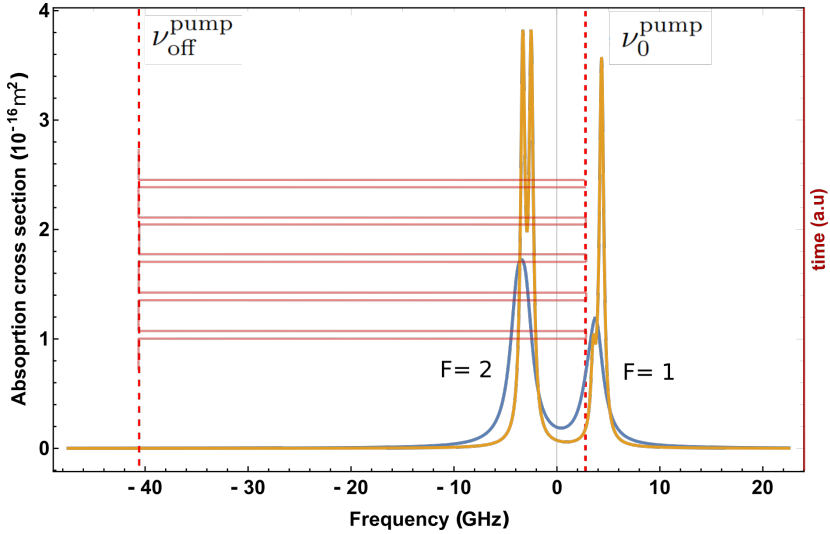diode temperature at $\mathrm{T} = 34\,°\mathrm{C}$ and injection current at $\mathrm{I} = 93\,\mathrm{mA}$

Figure 6.5.: **Optical pumping with frequency modulation**. The calculated
absorption cross section of atomic Rb vapor cell at $\mathrm{T} = 100\,°\mathrm{C}$ in
conditions no buffer gas (yellow) and with $100\,\mathrm{Torr}$ N_2 buffer gas
(blue). The pumping scheme consists of continuous wave beam with
pulsed frequency modulation (red solid line) as a function of time.
The optical pumping frequency is $\Omega \approx 30\,\mathrm{kHz}$, with $10\,\%$ tuned on
resonance $\nu_0^{\mathrm{pump}} = 3.2\,\mathrm{GHz}$ and $90\,\%$ detuned to the red by $\nu_{\mathrm{off}}^{\mathrm{pump}} = 42\,\mathrm{GHz}$ from the center of D1 line.

balanced polarimeter at sampling times t_i and the voltage, $V_{\mathrm{mod}}(t_i)$, used for the external modulation of the current supply of the pump laser. $V_{\mathrm{mod}}(t_i)$ is fitted to a sinusoidal waveform and the fitting parameters provide the values of the frequency Ω and the phase ϕ_{fit} to generate $V_{\mathrm{ref}}(t_i) = \cos(\Omega t_i + \phi_{\mathrm{fit}})$. A scheme of the lock-in detector is shown in Figure 6.6. The in-phase and quadrature components come from the mixing of $V_S(t_i)$ with $V_{\mathrm{ref}}(t_i)$ and the 90° shifted reference signal $V_{\mathrm{ref+}}(t_i)$ respectively, as;

$$u(t_i, \phi) = \sqrt{2}V_S(t_i)V_{\mathrm{ref}}(t_i) = \sqrt{2}V_S(t_i)\cos(\Omega t_i + \phi) \qquad (6.2)$$
$$v(t_i, \phi) = \sqrt{2}V_S(t_i)V_{\mathrm{ref+}}(t_i) = \sqrt{2}V_S(t_i)\cos(\Omega t_i + \phi + \pi/2). \qquad (6.3)$$

At this point, $u(t_i, \phi)$ and $v(t_i, \phi)$ are still functions of the free phase parameter ϕ. In order to find the optimum phase value $\tilde{\phi}$, we need to scan ϕ between $[-\pi, \pi]$. The value $\tilde{\phi}$ should maximize the average power spectral density of the in-phase component $u^{(\mathrm{raw})}(t_i, \phi)$.

$$\tilde{\phi} = \arg\max_{\phi} \int \mathcal{S}_{u(t_i,\phi)}(\nu)d\nu \qquad (6.4)$$

Then the in-phase and quadrature components depend only on t_i :

$$u^{(\mathrm{raw})}(t_i) = \sqrt{2}V_S(t_i)\cos(\Omega t_i + \tilde{\phi}) \qquad (6.5)$$
$$v^{(\mathrm{raw})}(t_i) = \sqrt{2}V_S(t_i)\cos(\Omega t_i + \tilde{\phi} + \pi/2), \qquad (6.6)$$

The last step of the lock in amplification filters out the higher harmonics of $k\Omega, k > 2$ that may come up after the mixing [103]. For the digital lock-in here, the final outputs are

$$u(t_i) = \mathrm{LP}[u^{(\mathrm{raw})}(t_i)] \qquad (6.7)$$
$$v(t_i) = \mathrm{LP}[v^{(\mathrm{raw})}(t_i)], \qquad (6.8)$$

where LP a first-order IIR filter with cutoff frequency $f_c = 26.5\,\mathrm{Hz}$ (Figure 6.7). The low pass filter is not always applied in the data analysis. As explained also in the next section, in the cases where we are interested in the frequency response of the sensor, the low pass filter is skipped. Then the final output of the lock in amplification are the components $u^{(\mathrm{raw})}(t_i)$ and $v^{(\mathrm{raw})}(t_i)$.

6.2. Signal processing

In this section, we present in more detail the methods used to calculate the equivalent magnetic noise spectral density $\mathcal{S}_B(\omega)$. The magnetometer is operated in 3 different conditions as far as the applied magnetic field is concerned. They are distinguished in ;

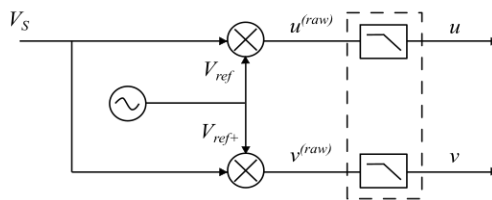Figure 6.6.: **Lock-in detector.** The polarimeter signal V_S is mixed with the reference signal V_{ref} to obtain in phase (u) and the 90° phase shifted $V_{\text{ref}+}$ the quadrature component (v) after the low pass filter.
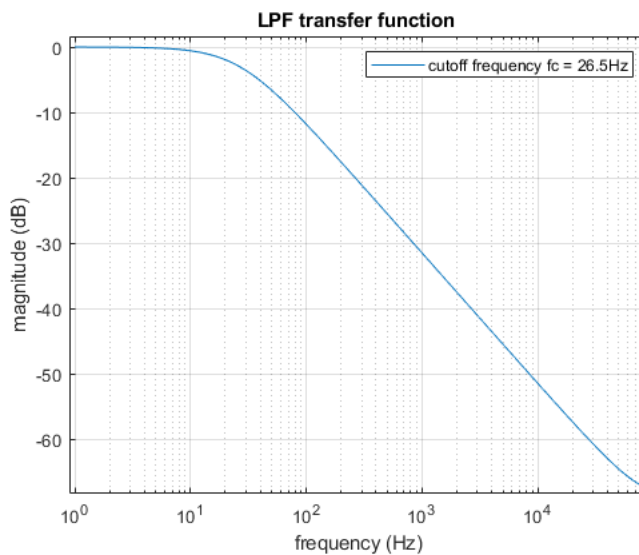

Figure 6.7.: **Transfer function of the low pass filter (LPF) used in the lock-in demodulation** The discrete time implementation of a simple RC low pass is designed in MatLAB through exponentially weighted moving average with smoothing factor $\alpha = 8.3 \times 10^{-6}$.
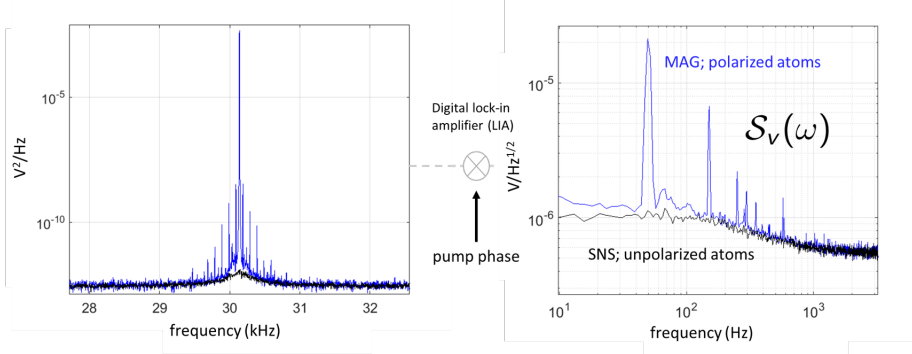
Figure 6.8.: **Power spectral density of the polarimeter signal** for polarized (blue) and non polarized (black) atomic ensemble. Noise spectra after the demodulation.

- the resonant case, where the bias field B_0 causes the atoms to precess on resonance with the pumping frequency $\Omega = \omega_L$,

- the scan of the bias magnetic field around B_0 and

- the addition of a test magnetic signal along the direction of the bias field.

Through the measurements we maintain the same BB OPM settings of cell temperature, probe beam (linear polarization, power and detuning) and optical pumping (frequency modulation, polarization and power). From these measurements we obtain the values for $\mathcal{S}_v(\omega)$, the slope $\frac{dv}{dB}$ and $|\hat{R}(\omega)|^2$ respectively and we calculate

$$\mathcal{S}_B(\omega) \quad = \quad \left(\frac{dv}{dB}\right)^{-2} \frac{\mathcal{S}_v(\omega)}{|\hat{R}(\omega)|^2}. \tag{6.9}$$

Resonant field

The signal $V_S(t_i)$ on this resonant condition is acquired for 100 acquisition cycles. Discrete Fourier transform is implemented with a Hann window in MatLAB to obtain the single sided spectrum. The average of 100 spectra is shown on the left part plot of Figure 6.8 with blue for the magnetometer signal. The lock-in demodulation of the signal $V_S(t_i)$ is implemented without the low pass filter to take the raw in-phase and quadrature component outputs $u^{(\mathrm{raw})}(t_i)$ and $v^{(\mathrm{raw})}(t_i)$. Fast Fourier transform is implemented for both components all of each acquisition cycle and the single sided spectrum is generated. The power spectral density $\mathcal{S}_v(\omega)$ of the quadrature component is again the average of 100 spectra.
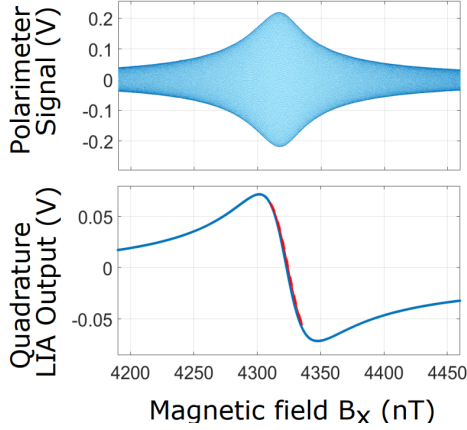
Figure 6.9.: **Polarimeter signal and magnetometer signal versus magnetic field.** (top) Polarimeter signal ($V_S(t)$) for fixed pumping modulation frequency while scanning the magnetic field through resonance. (bottom) OPM signal, i.e. quadrature output ($v(t)$) of the digital lock-in demodulation

As shown on the right hand plot of Figure 6.8, the demodulated signal of the magnetometer is compared against $\mathcal{S}_v(\omega)$ from a non polarized atomic ensemble. The pump beam is blocked during the data acquisition but $V_{\mathrm{mod}}(t_i)$ is acquired and used to generate $V_{\mathrm{ref}}(t_i)$ as described in the previous section.

Slope of dispersive signal $v(B)$

To find the slope $\frac{dv}{dB}\big|_{\Omega=\omega_L}$, we scan the bias magnetic field B_x through a range of 250 nT across the resonance B_0 and record the polarimeter signal $V_S(t_i)$ for 20 acquisition cycles. The ramp of magnetic field applied by modulating the current of the B_x with a period of 0.5 s. During the measurement the pumping frequency is fixed, while the Larmor precession frequency is ramped with the resonant condition $\Omega = \omega_L$ at the middle of the acquisition cycle $t = 0.25$ s. As shown in the top plot of Figure 6.9 the polarimeter signal amplitude then reduces as the magnetometer moves away from the resonant condition. The quadrature component $v(t_i)$ comes from the lock-in amplification of $V_S(t_i)$ including the low pass filtering and it is shown in the bottom plot of Figure 6.9, where the x axis has been calibrated from time to magnetic field units. It has the characteristic shape of a dispersive Lorentzian. This is predicted from the theory since $v(B) \propto F_\sigma(B)$ and according to Equation 3.17 :

$$F_\sigma = F_0 \frac{\Gamma_p}{2} \frac{\Omega - \omega_L(B)}{(\Omega - \omega_L(B))^2 + \Gamma_2^2}, \tag{6.10}$$

with the derivative

$$\left. \frac{\partial F_\sigma}{\partial B} \right|_{B=B_0} = \Gamma_0 \frac{\Gamma_p}{2} \frac{1}{\Gamma_2^2} \left. \frac{\partial \omega_L}{\partial B} \right|_{B=B_0} = \frac{u(0)}{\Gamma_2}. \tag{6.11}$$

In this measurement, we obtain the slope by performing a linear fit of $v(B)$ around the linear part that corresponds to $B = B_0$ indicated with the red dashed line. The linear fitting is repeated for all $v(t_i)$ corresponding to the 20 acquisition cycles and the final value for the slope is the average of the 20 fitting parameters.

Magnetic responsivity

The responsivity of the magnetometer, $|R(\omega)|^2$, is estimated by recording the sensor's noise spectrum while applying along the bias magnetic field direction a known test signal oscillating at different frequencies. In this measurement, we use an oscillatory signal of amplitude 5 mV and frequencies range from 10 Hz to 2.4 kHz as a modulation input to the low noise current generator Twinleaf CSUA 300. The modulation input bandwidth of Twinleaf CSUA 300 is 10 MHz. From the calibration presented in Figure B.2 we infer that the sinusoidal magnetic test signal has an amplitude of 0.18 nT. This is added on top of the 4.3 μT bias field along the x direction. For each magnetic test signal, the spectrum $\mathcal{S}_v(\omega)$ shows a narrow line on the oscillatory frequency. The maximum value of the narrow line is extracted from each spectrum and plotted in Figure 6.10. They can be fitted to the function

$$f(\omega) = \alpha^2 \frac{\Delta\omega^2}{\omega^2 + \Delta\omega^2}, \tag{6.12}$$

where the fitting parameter $\Delta\omega$ is the magnetic resonance linewidth and α the amplitude of the magnetic responsivity. We note that $f(\omega)$ has the same frequency dependence with the square of the responsivity $|R(\omega)|^2$ as derived from the theory in Equation 5.31.

The estimate of the linewidth (HWHM) from the fit of $|R(\omega)|^2$ is in agreement with the linewidth obtained from fitting the spin projection noise (cyan dashed line of Figure 4.3) with the same function $f(\omega)$, Equation 6.12. In this experiment, the fitting parameters of both curves give $\Delta\omega = 170$ Hz. The agreement of these two linewidth estimates is an experimental verification of fluctuation dissipation theorem, according to which the power spectrum of fluctuations is proportional to the frequency response of the system to a small driving force (see the discussion from chapter 2 of [104]).
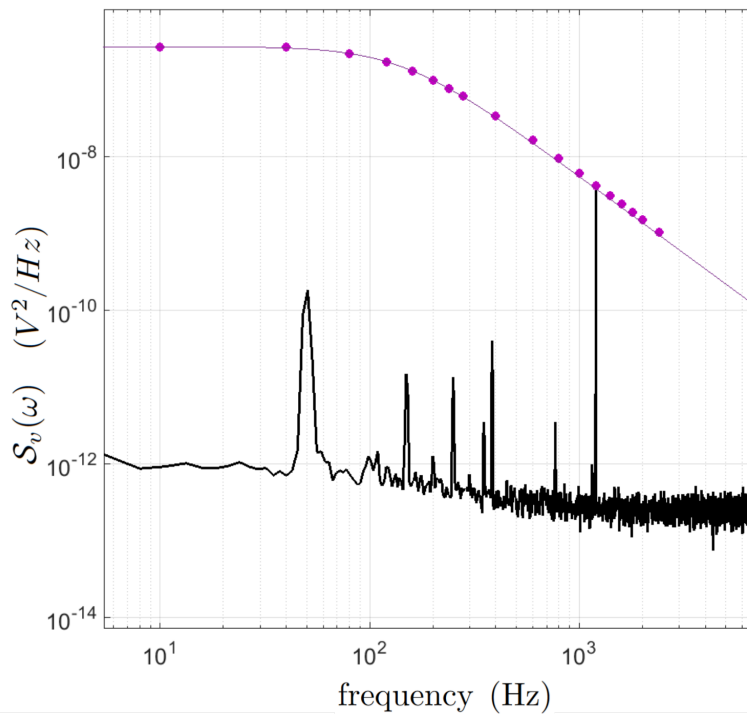
Figure 6.10.: **Experimentally measured magnetic responsivity.** Black curve shows $\mathcal{S}_v(\omega)$ when the frequency of the magnetic field modulation is $1.2\,\mathrm{kHz}$. The spectrum is averaged for 20 measurement cycles of $0.5\,\mathrm{s}$ each. The purple dots show the peak of PSD resonance for different values of the frequency of the magnetic test signal. Purple line shows the fit to the function $f(\omega)$, see equation 6.12.
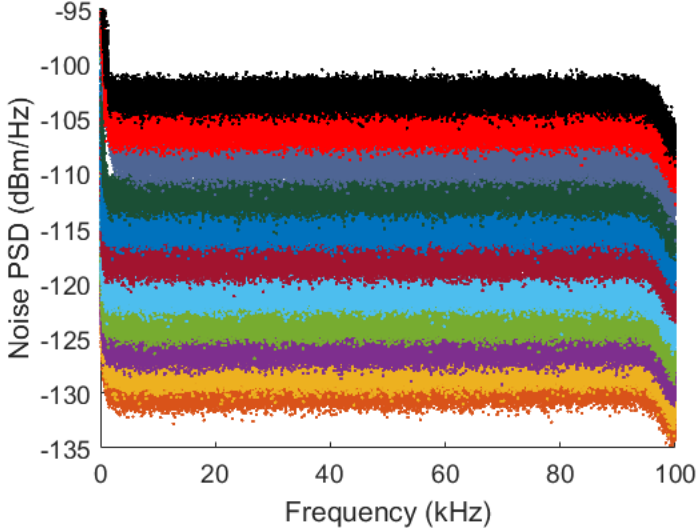
Figure 6.11.: **Detection noise.** Noise spectra of balanced detector at nominal gain 1×10^5 V/A acquired with mean optical power P = 0, 4, 8, 16, 32, 64, 135, 250, 500, 1000, 2000, 4000 µW, from bottom to top.

6.3. Detector characterization

This section presents the results from the noise characterization of the detector used in the experiment. The linearly polarized light beam, 20 GHz blue detuned from the D1 atomic transition, passes through the Rb vapor cell while it is in room temperature. For this measurement, there is no atomic contribution since the bias magnetic field is set to zero and the pump beam is blocked. The detection scheme includes the half-wave plate, the Wollastone prism and two pairs of AR coated plano and concave mirrors. The input light splits in two parts of equal power that reach the differential transimpidance amplifier (DTIA) Thorlabs PDB450A.

We record the output of the DTIA for different values of light input power ranging from 0 to 4 mV. Data are acquired for 50 measurement cycles with duration of 0.5 s. The average noise spectrum for each value of the probe power is plotted in Figure 6.11.

We define the noise power N at a given analysis frequency as the RMS value of the average noise spectrum around this frequency. Here we are interested in the analysis frequency of 30 kHz and plot N as a function of the input power, shown as blue dots in Figure 6.12.
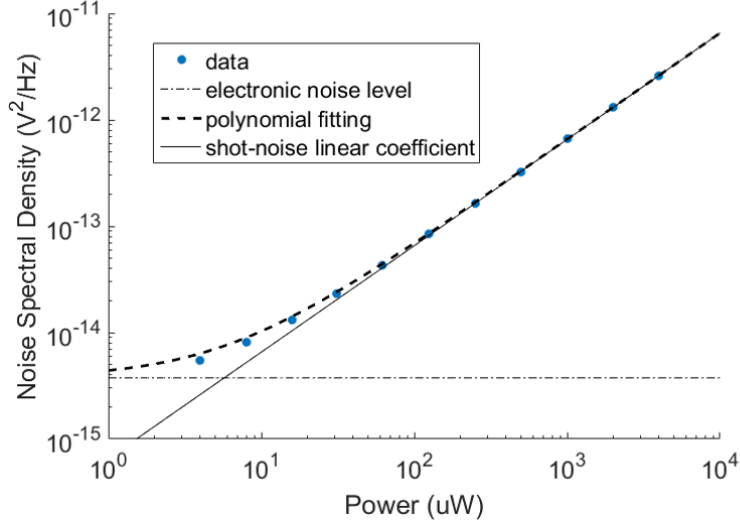
Figure 6.12.: **Shot noise limited power range** The estimated RMS values of the noise power spectral density around the frequency of 30 kHz are plotted as a function of the input power in log-log scale. The thick dashed line fits the data N(P) using Equation 6.13. Broken and solid lines represent the contribution from the electronic and photon shot noise respectively.

The noise power of the electronic output is a function of the average probe power P (see chapter 8 of [2]) :

$$N = A\,P^0 + B\,P^1 + C\,P^2, \tag{6.13}$$

where A, B and C constants.

The terms of the polynomial are the contributions of the electronic noise, the photon shot noise and the technical noise respectively. The detection is characterized photon shot noise limited in the power ranges where

$$B\,P^1 > A\,P^0 \quad \text{and} \quad B\,P^1 > C\,P^2. \tag{6.14}$$

We fit the data with the polynomial function of Equation 6.13 and obtain the values of A, B and C. The analysis shows that when gain of the DTIA is at 1×10^5 V/A the shot noise level is greater than the technical noise for input light power $P > 8\,\mu\text{W}$.

6.4. Squeezed light source

The squeezer light source was designed and built by Ana Predojević and details on its operation can be found in [37, 101]. In this section we mention the modifications of the setup that resulted in generation of 2.3 dB of polarization squeezing used in this experiment to probe the BB OPM.

6.4.1. Laser Stabilization

So far, the group has operated the squeezer for applications where the generated squeezed light was both on resonance [105, 106] and out of resonance [102] with the atomic transition of the D_1 line of Rb. In this work we chose the probe of the atomic magnetometer to be blue detuned by 20 GHz out of resonance of the ^{87}Rb D_1 line center. This increases the signal to noise ratio as the absorption losses that could degrade the squeezing are not significant.

We perform the frequency lock of the extended cavity diode laser using a fiber interferometer. The instrument was built by Jia Kong and more details on its design and characterization can be found in [88]. The fiber system contains two fiber interferometers of 5 m path difference; the frequency control interferometer (FCI) and the temperature control interferometer (TCI). It can reach frequency stability with Allan deviation of 6.9×10^{-10} at 1000 s.

In this application, we use the signal from the balanced photodiode only of the FCI output for the feedback of the laser current. The temperature of the ECDL is set at 26 °C and the mode hop free range area is about 5 GHz. The fiber interferometer in combination with the wavemeter monitoring allowed the lock of the ECDL at 377 130.6 GHz, i.e about 20 GHz to the blue of the D_1 line center of ^{87}Rb.

6.4.2. Second harmonic generation

For the second harmonic generation (SHG) we use the laser system Toptica TA SHG 110 that includes an integrated frequency doubling stage. The light source is a grating stabilized diode laser of Littrow configuration. The light goes through an optical isolator and beam shaping lens to couple to a tapered amplifier (TA). The TA output after a second optical isolator and beam shaping components goes through a beam splitter. 10 % of the amplified power is fiber coupled and it is used as the local oscillator in polarization squeezing. The remaining 90 % is sent to the ring resonator with an LBO crystal. The output of the second harmonic generation is an elliptical beam at 394.7 nm due to the walk-off effect. Because of the bad mode quality even after the beam passes through beam shaping optical components, the fiber coupling of SHG output does not exceed 50 % [101].

The system had to be adjusted so that the power of the 394.7 nm beam at the squeezer to be increased up to 40 mW. The modifications performed for the needs of this experiment are summarized bellow.

   i) The piezoelectric (PZT) actuator acting on the grating of the extended cavity diode master laser was substituted. After the substitution the frequency tuning was possible for a mode hop free scanning range of 5 GHz.

   ii) A half-wave plate and a PBS were introduced after the optical isolator following the master laser. 7 mW of the master laser are fiber coupled and part of it used as input to the fiber interferometer for frequency locking while the remaining power is used for the squeezer, as seed and counter-propagating beam as mentioned in the next subsection.

   iii) The TA chip was characterized and found to be degraded. We replaced it with a newer TA chip that can operate with current up to 4 A.

   iv) The incoupling mirrors and the SHG cavity were adjusted to generate a 394.7 nm light beam of about 100 mW power at the output of the TA-SHG system.

6.4.3. Polarization squeezing

After the fiber coupling, 40 mW of the TA-SHG output are used to pump a sub-threshold optical parametric oscillator (OPO). In this subsection, we summarize the operation of the squeezer setup. The interested reader may find details on the design and capabilities of this apparatus in [37, 101].

For the OPO a type-I periodically poled potassium titanyl phosphate (PPKTP) crystal is used. The crystal lies inside a bow-tie cavity whose length is locked with the Pound-Drever-Hall (PDH) technique as described in [107]. The locking beam is horizontally polarized and counter-propagating. The light comes from the master diode laser of the system Toptica TA-SHG 110 and it is frequency shifted through a double-pass AOM by about 630 MHz. Since the PPKTP crystal is birefringent, the OPO cavity is simultaneously resonant to the vertically polarized squeezed vacuum mode and the horizontally polarized locking beam. The reflection signal from the cavity is used to generate the PDH error signal as the ECDL's frequency is modulated at 20 MHz. The PDH error signal is given as input to an FPGA, followed by a PID controller. The amplified output controlling the cavity's length. The employed lock scheme, built by Ana Predojevic [101] , has minimal contamination to the squeezed vacuum output of the OPO. A half-wave plate and PBS have been added to filter the polarization of the reflection signal.
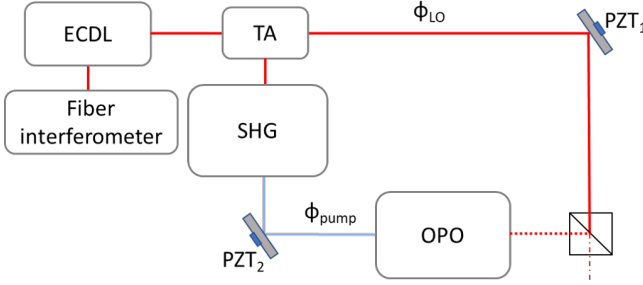
Figure 6.13.: **Quantum Noise lock**; Phase lock , Extended Cavity Diode Laser (ECDL), Tapered Amplifier (TA), Second Harmonic Generation Cavity (SHG), piezo-electric (PZT) actuator , Optical Parametric Oscillator (OPO)

For this work, since the polarization squeezed light is out of resonance, we changed the crystal's temperature in order to achieve the new phase matching conditions. A characterization for the parametric gain as a function of the crystal's temperature can be found in chapter 3 of [102]. Furthermore, due to the thermal lensing effect that is observed when the pump power changes [101], the incoupling alignment is optimized for each value of OPO pump power.

The polarization squeezing is detected at two positions: one right after the squeezing generation ("monitor balanced polarimeter") and a second at the output of the magnetic enclosure. The first balanced polarimeter consists of a half-wave plate, a PBS that splits the polarization in the two components. Both polarization components later pass through a focusing lens and sent to the two photodiodes of the balanced photon shot noise limited photodetector (PDB450A-DC Thorlabs). As described in section 6.3, the final detection stage is a similar setup that shows shot noise limited performance when the gain of the DTIA is set to $G = 1 \times 10^5$ V/A. The two setups are used in a complementary way. We first quantify the generated squeezing at the monitor balanced polarimeter then use the polarization squeezed light for probing of the magnetometer and detect the signal at the second one.

6.5. Quantum noise lock

The quantum noise lock [108] of the polarization squeezing is performed through the active control of the phase $\Delta\phi = \phi_{\mathrm{SV}} - \phi_{\mathrm{LO}}$ between the squeezed vacuum (ϕ_{SV}) and the local oscillator (ϕ_{LO}). The phase readout is the noise power of the balanced polarimeter signal. We monitor the power spectrum at the central

frequency of $1\,\mathrm{MHz}$ with a spectrum analyzer and observe the squeezing oscillations while ϕ_{LO} is ramped with frequency $0.1\,\mathrm{Hz}$. The minimum of the noise oscillations indicates the level of squeezing. For the active stabilization of the phase $\Delta\phi$, we apply RF modulation on the ϕ_{SV} and then demodulate the noise power signal to obtain an error signal. The zero crossings of the error signal correspond to the $\Delta\phi$ of squeezing or antisqueezing.

In the experiment, we used the chain of electronics depicted in Figure 6.14 to generate the phase readout. It is designed for the application of squeezed light to the BB OPM with optical pumping frequency around $30\,\mathrm{kHz}$.

The signal from the balanced detector has a bandwidth of $4\,\mathrm{MHz}$ as it is set to 10^5 gain. The 1/f noise contribution of the signal is filtered through a RC hihg pass filter and the notch filters minimize the impact of the dominant resonant frequency from the magnetometer signal. A low noise amplifier (Femto DHVA) with gain $40\,\mathrm{dB}$ amplifies the signal. The peak detector that follows a second notch filter, is a passive electric component, consisting of a diode placed in series with an RC circuit. The input signal charges the capacitor and due to the diode the discharge towards the incoming direction is prevented. The output of the peak detector passes through the low noise preamplifier (Stanford Research Systems SR560) for band-pass filtering and amplification.

At this point of the processing we obtain the noise level of the signal that is used as a phase readout. The signal is fed to the lock-in amplifier (Stanford Research Systems SR830 DSP). The device includes an internal frequency synthesizer that generates a sinusoid at $2.78\,\mathrm{kHz}$. This is used both for modulation ϕ_{SV}, acting on PZT_2 and as a reference signal for demodulation of the phase readout. The generated error signal is fed to the FPGA for the PID control of the PZT_1. (ϕ_{LO}).

Figure 6.14.: **Signal processing chain for the quantum noise lock.**

7

Squeezed light Bell Bloom OPM with varying atomic density vapor

One of the most important adjustable parameters in the operation of the Bell Bloom magnetometer is the atomic density. Dense alkali vapors induce strong Faraday rotation and show improved sensitivity. At the same time high atomic density operation implies frequent atomic collisions and high optical depth. The interplay between strong Faraday rotation and detrimental absorption and collisional effects determine the optimum for the alkali atom density.

As far as quantum enhancement is concerned, it remains to be shown if and how squeezing techniques are beneficial for optimized sensors. This question is important in the field of sensing and metrology. If quantum enhancement techniques are shown to have metrological advantage in some operational conditions but not at the optimum, then improving the sensor's sensitivity should rely on simpler traditional methods. They would be easy to implement and have at least as high performance as the quantum enhancement methods. This point is experimentally demonstrated in the work of Horrom et al. [29].

In this experiment squeezed light is implemented in a single beam atomic magnetometer and it improves the magnetometer's sensitivity when operated in the low atomic density regime. The operation in the optimal conditions is not affected by the use of squeezed light while for higher atomic density it has a detrimental effect in the sensitivity. The cause of this response to squeezed light could not be determined in that work. Therefore it remains to be investigated if this is an effect owing to technical limitations or there are fundamental reasons that prevent the further sensitivity improvement in high atomic densities. The above open question motivated the implementation of the polarization squeezed light in the Bell Bloom magnetometer described in chapter 4 for 7 different settings of atomic cell temperature between 85 °C to 110 °C. The set temperature values correspond to varying atomic density conditions between 2.18×10^{12} atoms/cm^3 and 1.13×10^{13} atoms/cm^3.
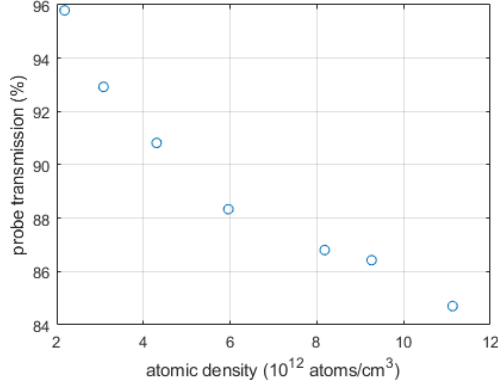
Figure 7.1.: **Probe power transmission**

7.1. Magnetometer operation

The system is operated as a Bell Bloom magnetometer at the finite magnetic field of 4.3 µT. The pump beam of 400 µW is frequency modulated in accordance with the pumping scheme described in chapter 6. The probe beam detuning is set at 20 GHz to the blue from D1 transition causing the beam transmission not to drop below 84 % at the highest atomic density condition. (Figure 7.1).

For the squeezer operation in this experiment, we use 35.4 mW of the frequency doubled output of Toptical TA-SHG 110 as pump for the OPO. The generated squeezing is 2 dB as measured at the monitor balanced detector before the atom light interaction in the magnetometer. The same squeezed light state is used for probing the spin dynamics as we increase the atomic density. The losses introduced due to the probe absorption by the atoms cause the degradation of the detected squeezing after the cell (Figure 7.2).

For each atomic density setting, the experiments performed are the following;

- spin noise spectroscopy probed both with linearly polarized light and polarization squeezed light,

- Bell Bloom magnetometer operation at 4.3 µT with frequency modulated pumping at angular frequency $\Omega = \omega_l = 2\pi \times 30$ kHz (50 acquisition cycles)

- Bell Bloom magnetometer operation at constant pumping frequency while the magnetic field is scanned between 4.2 µT and 4.45 µT (data acquisition for 20 cycles). The probing of the spin dynamics in this part is performed with classical light.
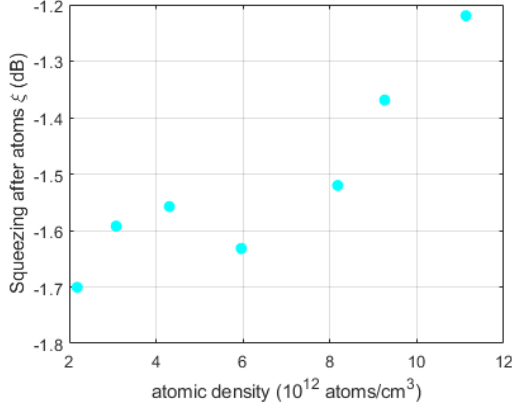
Figure 7.2.: **Dependence of the detected squeezing on the atomic density**
Losses introduced due to the absorption by the atoms degrade the
squeezing as the atomic density increases.

The data analysis discussed in detail in chapter 6 applies on the data of each
temperature setting as well. In particular, the fit of the in-phase LIA component
$u(t_i)$ provides the signal amplitude and the fit of the quadrature component $v(t_i)$
the linewidth of the magnetic resonance. As depicted in Figure 7.3, the signal
amplitude increases as a function of the atomic density up to a saturation point,
while the increase of the magnetic resonance linewidth is linear. Therefore the
slope $\frac{dv}{dB}|_{\Omega=\omega_L}$, which is proportional to the ratio of the two (Equation 6.11),
shows an optimum for the atomic density of 2.18×10^{12} atoms/cm^3, as depicted
in (Figure 7.4).

7.1.1. Power spectral density

The power spectral density of the quadrature signal is calculated both for the
magnetometer and spin noise spectroscopy signal. For each atomic density value
we obtain 50 spectra $\mathcal{S}_v^k(\omega)$, $k \in [1, 50]$, according to the process described in
chapter 6. We note that besides the technical noise coupling from the power line
showing as spikes at 50 Hz multiples, the average spectrum of the signal derived
from polarized atoms overlaps the one from unpolarized atoms. This is observed
for both types of probing and for all of the atomic density conditions.

The normalized magnetic frequency response $|\hat{R}(\omega)|$ of the sensor is calculated
from Equation 5.36, given the mean value of the magnetic resonance linewidth
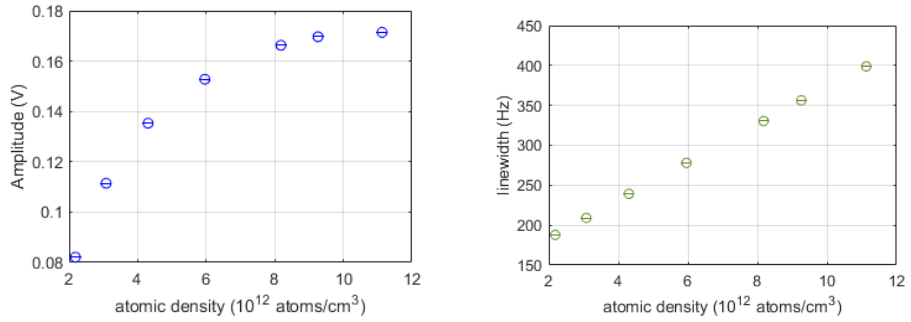$\Delta\omega$. The equivalent magnetic noise spectrum then follows from Equation 6.9,

Figure 7.3.: **Magnetometer signal as a function of atomic density** (a) amplitude (b) linewidth
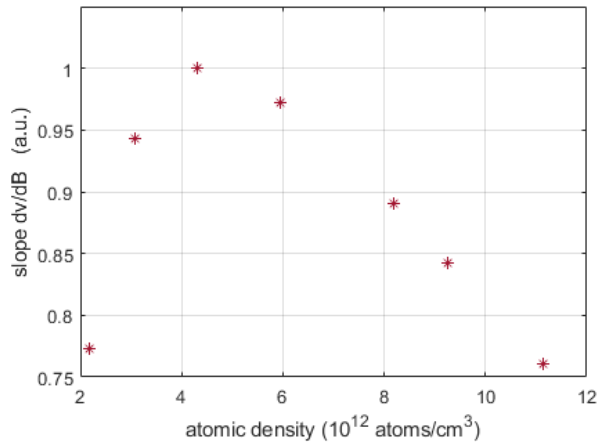

Figure 7.4.: **Slope dv/dB as a function of atomic density** The estimated errorbars are smaller than the ratio between the above quantitites gives the slope. The errorbars are too small to observe.
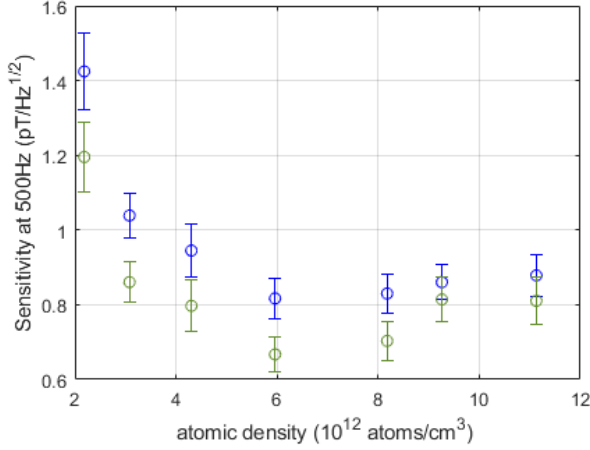
Figure 7.5.: **Dependence of the sensitivity at** 500 Hz **on the atomic density** Mean values sensitivity for the Bell Bloom magnetometer (blue) is improved when squeezed light is used for probing (green).

where the average value of 50 spectra is used for the mean value of $\mathcal{S}_v(\omega)$ and the standard error of the mean (SME) for $\Delta\mathcal{S}_v(\omega)$.

7.1.2. Enhancement of sensitivity and measurement bandwidth

Comparing the equivalent magnetic noise spectra for coherent and squeezed light probing (Figure 7.7, Figure 7.8), quantum enhancement is noted in the photon shot noise limited frequency range. In particular, focusing at the analysis frequency of 500 Hz, optical squeezing improves the sensitivity at all measured densities, and these span a range that includes the optimum density (Figure 7.7). This implies that with squeezing, the magnetometer can reach a sensitivity that it cannot reach without it.

According to Equation 5.38, each power spectral density $\mathcal{S}_v^k(\omega)$, for $k \in [1, 50]$, can be fitted to the equation

$$f(\omega) = \alpha + \mathcal{L}(\omega)\beta \tag{7.1}$$

where $\mathcal{L}(\omega)$ the normalized Lorentzian with $\Delta\omega$ the magnetic resonance linewidth. The fitting parameters α and β provide the value of the photon shot noise $\mathcal{S}_{N_{S_2}}$ and spin projection noise for the unpolarized atomic ensemble $\mathcal{S}_\sigma$ respectively. The reported value and error are determined as the mean and the standard error of the mean of the 50 fitting parameters $\mathcal{S}_{N_{S_2}}^k$ and $\mathcal{S}_\sigma^k$.

As discussed in chapter 4, the $3\,\mathrm{dB}$ measurement bandwidth is defined with respect to the above quantum noise levels as

$$\omega_{3\,\mathrm{dB}} \equiv \Delta\omega\sqrt{\mathcal{S}_\sigma/\mathcal{S}_{N_{S_2}} + 1} \tag{7.2}$$

In this experiment, the mean value $\omega_{3\,\mathrm{dB}}$ for classical and squeezed light noise is computed for each atomic density and the beneficial impact of squeezed light probing shows in all of the densities. (Figure 7.6)

In conclusion, in this chapter we have studied the application of polarization squeezed light to the Bell Bloom magnetometer of atomic vapor through a range of densities between $2.18 \times 10^{12}\,\mathrm{atoms/cm^3}$ and $1.13 \times 10^{13}\,\mathrm{atoms/cm^3}$. Optical squeezing, used for the off-resonant probing, was shown to suppress the optical noise without affecting the low frequency part of the equivalent magnetic noise. The results show an optimum of the magnetometer performance and demonstrate metrological advantage due to polarization squeezing in all of the conditions of atomic densities. In contrast to what was shown in previous work [29], in this backaction evading configuration, polarization squeezing is beneficial also for atomic densities beyond the optimum. Losses due to absorption from the atoms degrade the squeezing, an effect more evident at high atomic densities. Detuning further off resonance the squeezed light while increasing the optical power can compensate for the losses and give the conditions for equally good performance of the magnetic sensor. The above presented experimental results confirm the backaction evading scheme employed in the Bell Bloom magnetometer. According to Equation 4.4, vapor density is an important parameter for the measurement backaction noise. Operating with a magnetometer with more and more dense atomic vapor and showing the enhancement with optical squeezing for all the atomic density values is an additional proof of the backaction evasion. Given the importance of the atomic density for the sensitivity of the optical magnetometer, this work provides an insight on the impact of optical squeezing on an optimized magnetometer. As a following more involved step, optical squeezing can be implemented to a *fully* optimized magnetometer that is obtained after scanning all of the relevant parameters affecting the magnetometer sensitivity i.e probe beam power and detuning, optical pumping scheme for each atomic density value.
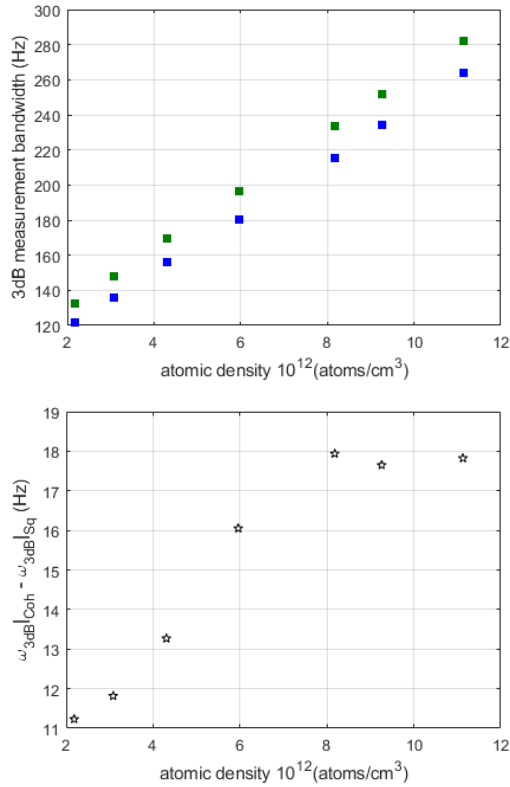
Figure 7.6.: **Dependence of** $3\,\mathrm{dB}$ **measurement bandwidth as a function of the atomic density** (a) measurement bandwidth for coherent (blue) and squeezed light (green) probing (b) quantum enhancement of $3\,\mathrm{dB}$ measurement bandwidth $\omega_{3\,\mathrm{dB}}|_{\mathrm{Coh}} - \omega_{3\,\mathrm{dB}}|_{\mathrm{Sq}}$.
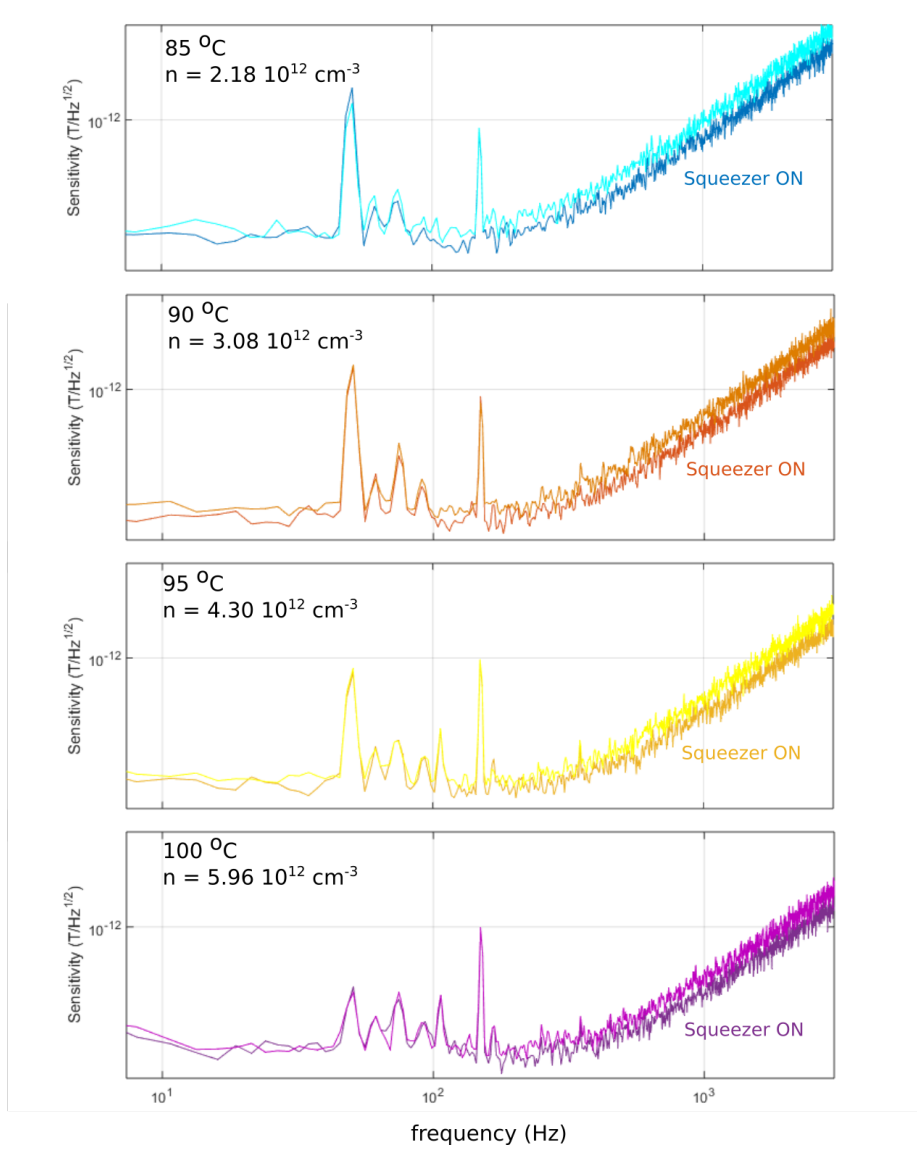
Figure 7.7.: **Equivalent magnetic noise spectrum for atomic density settings from** 2.18×10^{12} atoms/cm^3 **to** 5.96×10^{12} atoms/cm^3
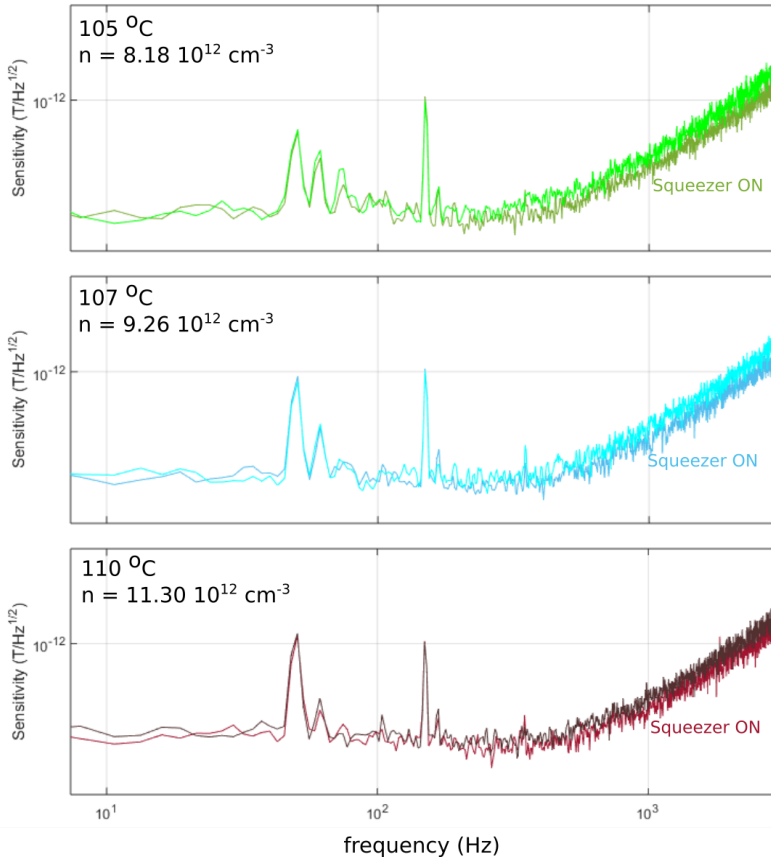
Figure 7.8.: **Equivalent magnetic noise spectrum for atomic density settings from** 8.18×10^{12} atoms/cm^3 **to** 11.3×10^{12} atoms/cm^3

8
Conclusions and outlook

In this thesis, we have studied the application of polarization squeezed light to improve the sensitivity and bandwidth of a sensitive optically-pumped magnetometer.

We used Bell-Bloom optical pumping on the D_1 line to generate a precessing spin polarization in a cell of ^{87}Rb with about 100 Torr of N_2 buffer gas, and Faraday rotation probing, also near the D_1 line but off resonance, to detect the spin precession. Used as a magnetometer, this system shows sub-pT/$\sqrt{\text{Hz}}$ sensitivity to fields near the Earth field, while also being quantum noise limited. For field strength changes at frequencies below about 100 Hz, spin projection noise is the dominant noise contribution, whereas for changes at frequencies above this frequency, shot noise is dominant.

We used a parametric amplifier, implemented with a periodically-poled nonlinear optical crystal inside a resonator cavity, to produce squeezed vacuum tunable around the Rb D_1 line. Combining this squeezed vacuum with a coherent state of orthogonal polarization, we produced light with sub-shot-noise fluctuations in the S_2 Stokes parameter, the parameter detected in the Faraday rotation measurement of the atomic polarization. The squeezer produces about ≈ 2 dB of vacuum squeezing, limited by the available pump power. A "quantum noise lock" was developed to stabilize the relative phase of the squeezed vacuum and coherent state, and thus ensure that the S_2 Stokes parameter was squeezed at all times.

Comparing the magnetometer's equivalent magnetic noise spectrum $\mathcal{S}_B(\omega)$ when probed with squeezed light versus with with coherent states, we observed the following: 1) squeezed light probing reduces $\mathcal{S}_B(\omega)$ in the shot-noise-limited frequency regime, 2) squeezed light probing increases the measurement bandwidth, i.e., the bandwidth at which the equivalent magnetic noise increases by 3 dB, 3) $\mathcal{S}_B(\omega)$ did not increase in the spin-projection noise limited frequency regime.

These observations are explained by a quantum physical model for the magnetometer dynamics. The model uses the Bloch equations to describe spin precession, and includes projection noise and shot noise via stochastic terms in the Bloch equations and readout equation, respectively. The model is solved by a

perturbative approach in which the Bloch equations are linearized around the noiseless solution. This linear equation for the noise explains the role of measurement back-action in the Bell-Bloom magnetometry scheme, and the role of probe squeezing in this scheme. When the detected S_2 Stokes parameter is squeezed, the accompanying antisqueezing of the S_3 Stokes parameter couples into the spin system through the AC Stark shift. In lowest order, this noise only alters the spin component along the magnetic field, a component that does not contribute to the signal. The scheme is thus back-action evading.

It is probably worth noting again how different this scenario is from "textbook" discussions of quantum noise in sensing. These often focus on canonical systems such as position and momentum, or two quadratures of the same field mode. In such systems, reducing noise in one variable inevitably increases noise in its conjugate. Here, in contrast, we are working with spin systems, not canonical systems, and the spin uncertainty relations relate three variables, not two. This allows that the spin oscillates between two components to generate a convenient AC signal, while a third absorbs the noise from measurement back-action. Similar observations have been made with cold atoms [98, 109, 91], but this is, to our knowledge, the first application of this idea to a practical sensor.

The magnetometer was also operated with fixed conditions for optical pumping and readout, at atomic vapor densities ranging from 2.18×10^{12} atoms/cm^3 to 1.13×10^{13} atoms/cm^3. The signal amplitude, detected noise spectrum and magnetic resonance width were recorded as a function of the vapor density. The sensitivity is observed to improve with increasing vapor density and then to degrade for densities higher than $n \approx 6 \times 10^{12}$ atoms/cm^3. The comparison of the magnetic noise spectra between laser- and squeezed-light probing shows improved sensitivity in the shot-noise-limited frequency range for all the measured atomic density values.

This final result provides an interesting companion to the work of Horrom et al. [29], which used a quite different squeezing and magnetometer strategy to study the role of optical squeezing in density-optimized optical magnetometry. That work observed that, for a given frequency of interest, squeezed-light probing improved magnetic sensitivity below the optimal density, worsened sensitivity above that density, and, to within experimental precision, left the optimal sensitivity unchanged. Given the ease with which density can be tuned in many atomic vapor systems, this cast doubt upon the utility of optical squeezing for probing vapor systems. One of the main motivations of this thesis was to understand if this observed behavior was universal, or only a feature of specific sensing methods. We conclude that it is the latter.
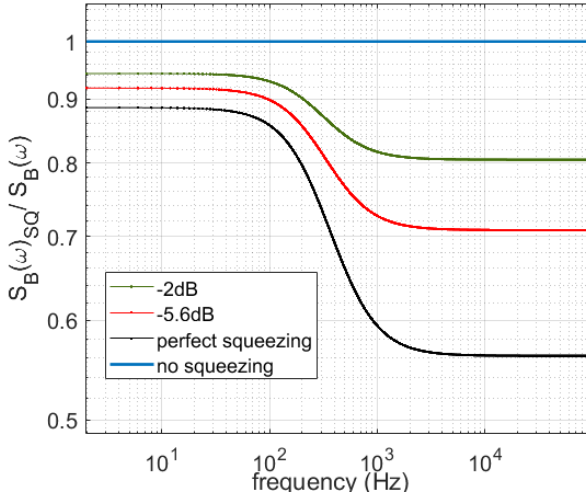
Figure 8.1.: $\mathcal{S}_B(\omega)_{\mathrm{SQ}}/\mathcal{S}_B(\omega)$ **Ratio of the equivalent magnetic noise spectrum for probing the magnetometer with squeezed light over the same quantity with no squeezing for three levels of squeezing before interaction with the atomic medium: the one used in the experiments of chapter 4 ($-2\,\mathrm{dB}$), the strongest squeezing reported at the Rb $\mathbf{D}_1$ line, and "perfect squeezing," i.e. vanishing noise in the S_2 Stokes component.**

Outlook: Further improvement with optical squeezing

The quantum advantages demonstrated in the thesis have been experimentally limited by the available squeezing [37]. It is natural to ask what sensitivity and bandwidth gains would be possible if more squeezing were available. This can be estimated using the model presented in chapter 5.

We first consider the performance of the Bell-Bloom magnetometer as implemented in chapter 4, but with different levels of input squeezing. Starting from the analytic expressions for the magnetic noise spectrum $\mathcal{S}_B(\omega)$ in Equation 5.39, we calculate $\mathcal{S}_B(\omega)_{\mathrm{SQ}}/\mathcal{S}_B(\omega)$, the ratio of the equivalent magnetic noise spectrum for probing with squeezed light, over the same quantity calculated for laser light, i.e. with $0\,\mathrm{dB}$ of squeezing. We consider three different values of the squeezing parameter ξ^2 before interaction with the atoms: $-2.0\,\mathrm{dB}$, which is the squeezing level in chapter 4, $-5.6\,\mathrm{dB}$, which is the strongest squeezing yet reported at the Rb D_1 line [46] and "perfect squeezing" with negligible remaining S_2 noise. The results are shown in Figure 8.1. As a representative result, for magnetic field fluctuations at $500\,\mathrm{Hz}$, up to $5\,\mathrm{dB}$ of sensitivity advantage could in principle be gained by perfect squeezing. Higher (lower) frequencies would have greater (lesser) advantages from the use of squeezed light.

The above results were obtained in simulations with fixed atomic density and fixed probe detuning, and thus with a fixed linear absorption of the probe light. This absorption explains why the advantage due to squeezing is limited to $5.6\,\mathrm{dB}$, because optical losses introduce additional noise. It is natural to ask whether adjustment of the density and/or probe detuning could reduce this absorption, without impacting the magnetometer sensitivity. As discussed in chapter 7, the magnetometer's sensitivity would clearly suffer if the density is significantly reduced. In contrast, an increase in probe detuning, accompanied by an increase in probe power to maintain the sensitivity to F_z, may be a more interesting strategy. This has been studied in cold atom Faraday probing [59], with the conclusion that detuning can be increased at constant sensitivity with zero net effect on "damage" to the atomic state via off-resonance scattering and measurement back-action. This suggests that something similar should occur in the Rb vapor system, so that strong squeezing before the atomic interaction could produce a similarly strong enhancement of magnetometer sensitivity.

The sensitivity enhancement techniques used in this thesis appear to be compatible with other methods that increase the signal to noise ratio [82] and bandwidth [110]. The techniques may also be applicable to instruments besides magnetometers. Vapor-phase gyroscopes [69, 111] and instruments to search for exotic spin-dependent forces, e.g. [70] or [112] operate on very similar principles to the Bell-Bloom magnetometer studied here.

Bibliography

[1] M. Scully and M. Zubairy, Quantum Optics. Cambridge University Press, 1997.

[2] H.-A. Bachor and T. C. Ralph, A guide to experiments in quantum optics. John Wiley & Sons, 2019.

[3] V. Braginsky and Y. Vorontsov, "Quantum mechanical limitations in macroscopic experiments and modern experimental technique," Usp Fiz. Nauk, vol. 114, pp. 41–53, 1974.

[4] C. W. Helstrom, "Quantum detection and estimation theory," Journal of Statistical Physics, vol. 1, pp. 231–252, Jun 1969.

[5] J. Abadie, B. P. Abbott, R. Abbott, and et al, "A gravitational wave observatory operating beyond the quantum shot-noise limit," Nature Physics, vol. 7, pp. 962–965, Dec 2011.

[6] J. Aasi, J. Abadie, B. P. Abbott, and et al, "Enhanced sensitivity of the ligo gravitational wave detector by using squeezed states of light," Nature Photonics, vol. 7, pp. 613–619, Aug 2013.

[7] F. Acernese and et al (Virgo Collaboration), "Increasing the astrophysical reach of the advanced virgo detector via the application of squeezed vacuum states of light," Phys. Rev. Lett., vol. 123, p. 231108, Dec 2019.

[8] C. M. Caves, "Quantum-mechanical noise in an interferometer," Phys. Rev. D, vol. 23, pp. 1693–1708, Apr 1981.

[9] M. Evans, S. Gras, P. Fritschel, J. Miller, L. Barsotti, D. Martynov, A. Brooks, D. Coyne, R. Abbott, R. X. Adhikari, K. Arai, R. Bork, B. Kells, J. Rollins, N. Smith-Lefebvre, G. Vajente, H. Yamamoto, C. Adams, S. Aston, J. Betzweiser, V. Frolov, A. Mullavey, A. Pele, J. Romie, M. Thomas, K. Thorne, S. Dwyer, K. Izumi, K. Kawabe, D. Sigg, R. Derosa, A. Effler, K. Kokeyama, S. Ballmer, T. J. Massinger, A. Staley, M. Heinze, C. Mueller, H. Grote, R. Ward, E. King, D. Blair, L. Ju, and C. Zhao, "Observation of parametric instability in advanced ligo," Phys. Rev. Lett., vol. 114, p. 161102, Apr 2015.

[10] J. Aasi, J. Abadie, B. Abbott, R. Abbott, T. Abbott, M. Abernathy, C. Adams, T. Adams, P. Addesso, R. Adhikari, et al., "Enhanced sensitivity of the ligo gravitational wave detector by using squeezed states of light," Nature Photonics, vol. 7, no. 8, pp. 613–619, 2013.

Bibliography

[11] F. Acernese, M. Agathos, L. Aiello, A. Allocca, A. Amato, S. Ansoldi, S. Antier, M. Arène, N. Arnaud, S. Ascenzi, et al., "Increasing the astrophysical reach of the advanced virgo detector via the application of squeezed vacuum states of light," Physical review letters, vol. 123, no. 23, p. 231108, 2019.

[12] H. Yu, L. McCuller, M. Tse, N. Kijbunchoo, L. Barsotti, and N. Mavalvala, "Quantum correlations between light and the kilogram-mass mirrors of ligo," Nature, vol. 583, no. 7814, pp. 43–47, 2020.

[13] F. Acernese and et. al., "Quantum backaction on kg-scale mirrors: Observation of radiation pressure noise in the advanced virgo detector," Phys. Rev. Lett., vol. 125, p. 131101, Sep 2020.

[14] W. Happer, "Optical pumping," Rev. Mod. Phys., vol. 44, pp. 169–249, Apr 1972.

[15] W. Happer and B. Mathur, "Effective operator formalism in optical pumping," Physical Review, vol. 163, no. 1, p. 12, 1967.

[16] I. K. Kominis, T. W. Kornack, J. C. Allred, and M. V. Romalis, "A subfemtotesla multichannel atomic magnetometer," Nature, vol. 422, pp. 596–599, Apr. 2003.

[17] D. Budker and M. Romalis, "Optical magnetometry," Nat Phys, vol. 3, pp. 227–234, Apr. 2007.

[18] H. B. Dang, A. C. Maloof, and M. V. Romalis, "Ultrahigh sensitivity magnetic field and magnetization measurements with an atomic magnetometer," Appl. Phys. Lett., vol. 97, no. 15, p. 151110, 2010.

[19] K.-M. C. Fu, G. Z. Iwata, A. Wickenbrock, and D. Budker, "Sensitive magnetometry in challenging environments," AVS Quantum Science, vol. 2, no. 4, p. 044702, 2020.

[20] M. N. Nabighian, V. J. S. Grauch, R. O. Hansen, T. R. LaFehr, Y. Li, J. W. Peirce, J. D. Phillips, and M. E. Ruder, "75th anniversary: The historical development of the magnetic method in explorationhistorical development of magnetic method," Geophysics, vol. 70, no. 6, p. 33ND, 2005.

[21] P. D. D. Schwindt, S. Knappe, V. Shah, L. Hollberg, J. Kitching, L.-A. Liew, and J. Moreland, "Chip-scale atomic magnetometer," Appl. Phys. Lett., vol. 85, pp. 6409–6411, Dec. 2004.

[22] E. Boto, N. Holmes, J. Leggett, G. Roberts, V. Shah, S. S. Meyer, L. D. Muñoz, K. J. Mullinger, T. M. Tierney, S. Bestmann, et al., "Moving magnetoencephalography towards real-world applications with a wearable system," Nature, vol. 555, no. 7698, pp. 657–661, 2018.

[23] A. Borna, J. Iivanainen, T. R. Carter, J. McKay, S. Taulu, J. Stephen, and P. D. Schwindt, "Cross-axis projection error in optically pumped magnetometers and its implication for magnetoencephalography systems," NeuroImage, vol. 247, p. 118818, 2022.

[24] S. Afach, B. C. Buchler, D. Budker, C. Dailey, A. Derevianko, V. Dumont, N. L. Figueroa, I. Gerhardt, Z. D. Grujić, H. Guo, et al., "Search for topological defect dark matter with a global network of optical magnetometers," Nature Physics, vol. 17, no. 12, pp. 1396–1401, 2021.

[25] M. V. Romalis, Quantum noise in atomic magnetometers, p. 25–39. Cambridge University Press, 2013.

[26] J. Kong, R. Jiménez-Martínez, C. Troullinou, V. G. Lucivero, G. Tóth, and M. W. Mitchell, "Measurement-induced, spatially-extended entanglement in a hot, strongly-interacting atomic system," Nature Communications, vol. 11, no. 1, p. 2415, 2020.

[27] H. Bao, J. Duan, S. Jin, X. Lu, P. Li, W. Qu, M. Wang, I. Novikova, E. E. Mikhailov, K.-F. Zhao, K. Mølmer, H. Shen, and Y. Xiao, "Spin squeezing of 1011 atoms by prediction and retrodiction measurements," Nature, vol. 581, no. 7807, pp. 159–163, 2020.

[28] F. Wolfgramm, A. Cerè, F. A. Beduini, A. Predojević, M. Koschorreck, and M. W. Mitchell, "Squeezed-light optical magnetometry," Phys. Rev. Lett., vol. 105, p. 053601, Jul 2010.

[29] T. Horrom, R. Singh, J. P. Dowling, and E. E. Mikhailov, "Quantum-enhanced magnetometer with low-frequency squeezing," Phys. Rev. A, vol. 86, p. 023803, Aug 2012.

[30] N. Otterstrom, R. C. Pooser, and B. J. Lawrie, "Nonlinear optical magnetometry with accessible in situ optical squeezing," Opt. Lett., vol. 39, pp. 6533–6536, Nov 2014.

[31] I. Novikova, E. E. Mikhailov, and Y. Xiao, "Excess optical quantum noise in atomic sensors," Phys. Rev. A, vol. 91, p. 051804, May 2015.

[32] L. Bai, X. Wen, Y. Yang, L. Zhang, J. He, Y. Wang, and J. Wang, "Quantum-enhanced rubidium atomic magnetometer based on faraday rotation via 795 nm stokes operator squeezed light," Journal of Optics, vol. 23, p. 085202, aug 2021.

[33] C. Troullinou, R. Jiménez-Martínez, J. Kong, V. G. Lucivero, and M. W. Mitchell, "Squeezed-light enhancement and backaction evasion in a high sensitivity optically pumped magnetometer," Phys. Rev. Lett., vol. 127, p. 193601, Nov 2021.

[34] X. Zhang, S. Jin, W. Qu, and Y. Xiao, "Dichroism and birefringence optical atomic magnetometer with or without self-generated light squeezing," Applied Physics Letters, vol. 119, no. 5, p. 054001, 2021.

[35] G. Vasilakis, V. Shah, and M. V. Romalis, "Stroboscopic backaction evasion in a dense alkali-metal vapor," Phys. Rev. Lett., vol. 106, p. 143601, Apr 2011.

[36] R. Schnabel, W. P. Bowen, N. Treps, T. C. Ralph, H.-A. Bachor, and P. K. Lam, "Stokes-operator-squeezed continuous-variable polarization states," Phys. Rev. A, vol. 67, p. 012316, Jan 2003.

[37] A. Predojević, Z. Zhai, J. M. Caballero, and M. W. Mitchell, "Rubidium resonant squeezed light from a diode-pumped optical-parametric oscillator," Phys. Rev. A, vol. 78, p. 063820, Dec 2008.

[38] R. J. Glauber, "The quantum theory of optical coherence," Phys. Rev., vol. 130, pp. 2529–2539, Jun 1963.

[39] R. E. Slusher, L. W. Hollberg, B. Yurke, J. C. Mertz, and J. F. Valley, "Observation of squeezed states generated by four-wave mixing in an optical cavity," Phys. Rev. Lett., vol. 55, pp. 2409–2412, Nov 1985.

[40] A. B. Matsko, I. Novikova, G. R. Welch, D. Budker, D. F. Kimball, and S. M. Rochester, "Vacuum squeezing in atomic media via self-rotation," Phys. Rev. A, vol. 66, p. 043815, Oct 2002.

[41] J. Ries, B. Brezger, and A. I. Lvovsky, "Experimental vacuum squeezing in rubidium vapor via self-rotation," Phys. Rev. A, vol. 68, p. 025801, Aug 2003.

[42] E. E. Mikhailov and I. Novikova, "Low-frequency vacuum squeezing via polarization self-rotation in rb vapor," Opt. Lett., vol. 33, pp. 1213–1215, Jun 2008.

[43] L.-A. Wu, H. J. Kimble, J. L. Hall, and H. Wu, "Generation of squeezed states by parametric down conversion," Phys. Rev. Lett., vol. 57, pp. 2520–2523, Nov 1986.

[44] H. Vahlbruch, M. Mehmet, K. Danzmann, and R. Schnabel, "Detection of 15 db squeezed states of light and their application for the absolute calibration of photoelectric quantum efficiency," Phys. Rev. Lett., vol. 117, p. 110801, Sep 2016.

[45] G. Hétet, O. Glöckl, K. A. Pilypas, C. C. Harb, B. C. Buchler, H.-A. Bachor, and P. K. Lam, "Squeezed light for bandwidth-limited atom optics experiments at the rubidium d1 line," Journal of Physics B: Atomic, Molecular and Optical Physics, vol. 40, pp. 221–226, dec 2006.

[46] Y. Han, X. Wen, J. He, B. Yang, Y. Wang, and J. Wang, "Improvement of vacuum squeezing resonant on the rubidium d1 line at 795 nm," Opt. Express, vol. 24, pp. 2350–2359, Feb 2016.

[47] D. A. Steck, "Rubidium 87 d line data, 2001," URL http://steck.us/alkalidata, vol. 83, 2016.

[48] S. J. Seltzer, Developments in Alkali-Metal Atomic Magnetometry. PhD thesis, Princeton University, 2008.

[49] S. J. Seltzer and M. V. Romalis, "High-temperature alkali vapor cells with antirelaxation surface coatings," Journal of Applied Physics, vol. 106, no. 11, p. 114905, 2009.

[50] W. C. Griffith, S. Knappe, and J. Kitching, "Femtotesla atomic magnetometry in a microfabricated vapor cell," Opt. Express, vol. 18, pp. 27167–27172, Dec 2010.

[51] M. V. Romalis, "Hybrid optical pumping of optically dense alkali-metal vapor without quenching gas," Phys. Rev. Lett., vol. 105, p. 243001, Dec 2010.

[52] W. E. Bell and A. L. Bloom, "Optically driven spin precession," Phys. Rev. Lett., vol. 6, pp. 280–281, Mar 1961.

[53] R. Jimenez Martinez, "Microfabricated spin polarized atomic magnetometers," Ph. D. Thesis, 2013.

[54] S. R. de Echaniz, M. Koschorreck, M. Napolitano, M. Kubasik, and M. W. Mitchell, "Hamiltonian design in atom-light interactions with rubidium ensembles: A quantum-information toolbox," Phys. Rev. A, vol. 77, p. 032316, Mar 2008.

Bibliography

[55] B. Julsgaard, Brian Julsgaard-PhD. PhD thesis, PhD thesis, 2003.

[56] D. V. Kupriyanov, O. S. Mishina, I. M. Sokolov, B. Julsgaard, and E. S. Polzik, "Multimode entanglement of light and atomic ensembles via off-resonant coherent forward scattering," Phys. Rev. A, vol. 71, p. 032348, Mar 2005.

[57] J. M. Geremia, J. K. Stockton, and H. Mabuchi, "Tensor polarizability and dispersive quantum measurement of multilevel atoms," Phys. Rev. A, vol. 73, p. 042112, Apr 2006.

[58] J. K. Stockton, Continuous quantum measurement of cold alkali-atom spins. PhD thesis, California Institute of Technology, Mar 2007.

[59] M. Koschorreck, Generation of Spin Squeezing in an Ensemble of Cold RUbidium 87. PhD thesis, ICFO, 2010.

[60] G. Vasilakis, Precision measurements of spin interactions with high density atomic vapors. PhD thesis, Princeton University, 2011.

[61] M. Fleischhauer, A. B. Matsko, and M. O. Scully, "Quantum limit of optical magnetometry in the presence of ac stark shifts," Phys. Rev. A, vol. 62, p. 013808, Jun 2000.

[62] I. Novikova, A. B. Matsko, V. L. Velichansky, M. O. Scully, and G. R. Welch, "Compensation of ac stark shifts in optical magnetometry," Phys. Rev. A, vol. 63, p. 063802, May 2001.

[63] I. Sulai, R. Wyllie, M. Kauer, G. Smetana, R. Wakai, and T. Walker, "Diffusive suppression of ac-stark shifts in atomic magnetometers," Optics letters, vol. 38, no. 6, pp. 974–976, 2013.

[64] D. F. J. Kimball, E. B. Alexandrov, and D. Budker, General principles and characteristics of optical magnetometers, p. 3–24. Cambridge University Press, 2013.

[65] A. Leszczyński, M. Mazelanik, M. Lipka, M. Parniak, M. Dąbrowski, and W. Wasilewski, "Spatially resolved control of fictitious magnetic fields in a cold atomic ensemble," Optics Letters, vol. 43, no. 5, pp. 1147–1150, 2018.

[66] E. Boto, N. Holmes, J. Leggett, G. Roberts, V. Shah, S. S. Meyer, L. D. Muñoz, K. J. Mullinger, T. M. Tierney, S. Bestmann, G. R. Barnes, R. Bowtell, and M. J. Brookes, "Moving magnetoencephalography towards real-world applications with a wearable system," Nature, vol. 555, pp. 657–, Mar. 2018.

[67] C. Abel, S. Afach, N. J. Ayres, C. A. Baker, G. Ban, G. Bison, K. Bodek, V. Bondar, M. Burghoff, E. Chanel, Z. Chowdhuri, P.-J. Chiu, B. Clement, C. B. Crawford, M. Daum, S. Emmenegger, L. Ferraris-Bouchez, M. Fertl, P. Flaux, B. Franke, A. Fratangelo, P. Geltenbort, K. Green, W. C. Griffith, M. van der Grinten, Z. D. Grujić, P. G. Harris, L. Hayen, W. Heil, R. Henneck, V. Hélaine, N. Hild, Z. Hodge, M. Horras, P. Iaydjiev, S. N. Ivanov, M. Kasprzak, Y. Kermaidic, K. Kirch, A. Knecht, P. Knowles, H.-C. Koch, P. A. Koss, S. Komposch, A. Kozela, A. Kraft, J. Krempel, M. Kuźniak, B. Lauss, T. Lefort, Y. Lemière, A. Leredde, P. Mohanmurthy, A. Mtchedlishvili, M. Musgrave, O. Naviliat-Cuncic, D. Pais, F. M. Piegsa, E. Pierre, G. Pignol, C. Plonka-Spehr, P. N. Prashanth, G. Quéméner, M. Rawlik, D. Rebreyend, I. Rienäcker, D. Ries, S. Roccia, G. Rogel, D. Rozpedzik, A. Schnabel, P. Schmidt-Wellenburg, N. Severijns, D. Shiers, R. Tavakoli Dinani, J. A. Thorne, R. Virot, J. Voigt, A. Weis, E. Wursten, G. Wyszynski, J. Zejma, J. Zenner, and G. Zsigmond, "Measurement of the permanent electric dipole moment of the neutron," Phys. Rev. Lett., vol. 124, p. 081803, Feb 2020.

[68] S. Knappe, V. Gerginov, P. D. Schwindt, V. Shah, H. G. Robinson, L. Hollberg, and J. Kitching, "Atomic vapor cells for chip-scale atomic clocks with improved long-term frequency stability," Opt. Lett., vol. 30, pp. 2351–2353, Sep 2005.

[69] T. W. Kornack, R. K. Ghosh, and M. V. Romalis, "Nuclear spin gyroscope based on an atomic comagnetometer," Phys. Rev. Lett., vol. 95, p. 230801, Nov 2005.

[70] J. Lee, A. Almasi, and M. Romalis, "Improved limits on spin-mass interactions," Phys. Rev. Lett., vol. 120, p. 161801, Apr 2018.

[71] M. E. Limes, D. Sheng, and M. V. Romalis, "^{3}He$-^{129}$Xe comagnetometery using ^{87}Rb detection and decoupling," Phys. Rev. Lett., vol. 120, p. 033401, Jan 2018.

[72] S. F. Huelga, C. Macchiavello, T. Pellizzari, A. K. Ekert, M. B. Plenio, and J. I. Cirac, "Improvement of frequency standards with quantum entanglement," Phys. Rev. Lett., vol. 79, pp. 3865–3868, Nov 1997.

[73] M. Auzinsh, D. Budker, D. F. Kimball, S. M. Rochester, J. E. Stalnaker, A. O. Sushkov, and V. V. Yashchuk, "Can a quantum nondemolition measurement improve the sensitivity of an atomic magnetometer?," Phys. Rev. Lett., vol. 93, p. 173002, Oct 2004.

[74] P. Grangier, R. E. Slusher, B. Yurke, and A. LaPorta, "Squeezed-light–enhanced polarization interferometer," Phys. Rev. Lett., vol. 59, pp. 2153–2156, Nov 1987.

[75] E. S. Polzik, J. Carri, and H. J. Kimble, "Spectroscopy with squeezed light," Phys. Rev. Lett., vol. 68, pp. 3020–3023, May 1992.

[76] Y. Han, X. Wen, J. He, B. Yang, Y. Wang, and J. Wang, "Improvement of vacuum squeezing resonant on the rubidium d1 line at 795 nm," Opt. Express, vol. 24, pp. 2350–2359, Feb 2016.

[77] I. Novikova, E. E. Mikhailov, and Y. Xiao, "Excess optical quantum noise in atomic sensors," Phys. Rev. A, vol. 91, p. 051804, May 2015.

[78] X. Zhang, S. Jin, W. Qu, and Y. Xiao, "Dichroism and birefringence optical atomic magnetometer with or without self-generated light squeezing," Applied Physics Letters, vol. 119, no. 5, p. 054001, 2021.

[79] V. Shah, G. Vasilakis, and M. V. Romalis, "High bandwidth atomic magnetometery with continuous quantum nondemolition measurements," Phys. Rev. Lett., vol. 104, p. 013601, Jan 2010.

[80] V. Gerginov, M. Pomponio, and S. Knappe, "Scalar magnetometry below 100 ft/hz1/2 in a microfabricated cell," IEEE Sensors Journal, vol. 20, no. 21, pp. 12684–12690, 2020.

[81] D. Sheng, S. Li, N. Dural, and M. V. Romalis, "Subfemtotesla scalar atomic magnetometry using multipass cells," Phys. Rev. Lett., vol. 110, p. 160802, Apr 2013.

[82] V. Lucivero, W. Lee, N. Dural, and M. Romalis, "Femtotesla direct magnetic gradiometer using a single multipass cell," Phys. Rev. Applied, vol. 15, p. 014004, Jan 2021.

[83] A. R. Perry, M. D. Bulatowicz, M. Larsen, T. G. Walker, and R. Wyllie, "All-optical intrinsic atomic gradiometer with sub-20 ft/cm/√hz sensitivity in a 22 µt earth-scale magnetic field," Opt. Express, vol. 28, pp. 36696–36705, Nov 2020.

[84] R. Li, F. N. Baynes, A. N. Luiten, and C. Perrella, "Continuous high-sensitivity and high-bandwidth atomic magnetometer," Phys. Rev. Applied, vol. 14, p. 064067, Dec 2020.

[85] V. G. Lucivero, W. Lee, M. E. Limes, E. L. Foley, T. W. Kornack, and M. V. Romalis, "A femtotesla quantum-noise-limited pulsed gradiometer at finite

fields," in Quantum Information and Measurement (QIM) V: Quantum Technologies, p. T3C.3, Optica Publishing Group, 2019.

[86] M. Limes, E. Foley, T. Kornack, S. Caliga, S. McBride, A. Braun, W. Lee, V. Lucivero, and M. Romalis, "Portable magnetometry for detection of biomagnetism in ambient environments," Phys. Rev. Applied, vol. 14, p. 011002, Jul 2020.

[87] M. W. Mitchell and S. Palacios Alvarez, "Colloquium: Quantum limits to the energy resolution of magnetic field sensors," Rev. Mod. Phys., vol. 92, p. 021001, Apr 2020.

[88] J. Kong, V. G. Lucivero, R. Jiménez-Martínez, and M. W. Mitchell, "Long-term laser frequency stabilization using fiber interferometers," Review of Scientific Instruments, vol. 86, no. 7, p. 073104, 2015.

[89] V. G. Lucivero, P. Anielski, W. Gawlik, and M. W. Mitchell, "Shot-noise-limited magnetometer with sub-picotesla sensitivity at room temperature," Review of Scientific Instruments, vol. 85, no. 11, pp. –, 2014.

[90] W. Happer and B. S. Mathur, "Effective operator formalism in optical pumping," Phys. Rev., vol. 163, pp. 12–25, Nov 1967.

[91] G. Colangelo, F. M. Ciurana, L. C. Bianchet, R. J. Sewell, and M. W. Mitchell, "Simultaneous tracking of spin angle and amplitude beyond classical limits," Nature, vol. 543, pp. 525–528, 03 2017.

[92] G. Colangelo, F. Martin Ciurana, G. Puentes, M. W. Mitchell, and R. J. Sewell, "Entanglement-enhanced phase estimation without prior phase information," Physical Review Letters, vol. 118, p. 233603, Jun 2017.

[93] R. Jiménez-Martínez, W. C. Griffith, S. Knappe, J. Kitching, and M. Prouty, "High-bandwidth optical magnetometer," J. Opt. Soc. Am. B, vol. 29, pp. 3398–3403, Dec 2012.

[94] V. Gerginov, S. Krzyzewski, and S. Knappe, "Pulsed operation of a miniature scalar optically pumped magnetometer," J. Opt. Soc. Am. B, vol. 34, pp. 1429–1434, Jul 2017.

[95] V. G. Lucivero, R. Jiménez-Martínez, J. Kong, and M. W. Mitchell, "Squeezed-light spin noise spectroscopy," Phys. Rev. A, vol. 93, p. 053802, May 2016.

[96] V. G. Lucivero, A. Dimic, J. Kong, R. Jiménez-Martínez, and M. W. Mitchell, "Sensitivity, quantum limits, and quantum enhancement of noise spectroscopies," Phys. Rev. A, vol. 95, p. 041803, Apr 2017.

[97] L. McCuller, C. Whittle, D. Ganapathy, K. Komori, M. Tse, A. Fernandez-Galiana, L. Barsotti, P. Fritschel, M. MacInnis, F. Matichard, K. Mason, N. Mavalvala, R. Mittleman, H. Yu, M. E. Zucker, and M. Evans, "Frequency-dependent squeezing for advanced ligo," Phys. Rev. Lett., vol. 124, p. 171102, Apr 2020.

[98] Q. Y. He, S.-G. Peng, P. D. Drummond, and M. D. Reid, "Planar quantum squeezing and atom interferometry," Phys. Rev. A, vol. 84, p. 022107, Aug 2011.

[99] I. M. Savukov, Spin Exchange Relaxation Free (SERF) Magnetometers, pp. 451–491. Cham: Springer International Publishing, 2017.

[100] R. Jiménez-Martínez, J. Kołodyński, C. Troullinou, V. G. Lucivero, J. Kong, and M. W. Mitchell, "Signal tracking beyond the time resolution of an atomic sensor by kalman filtering," Phys. Rev. Lett., vol. 120, p. 040503, Jan 2018.

[101] A. Predojevic, Rubidium resonant squeezed light from a diode-pumped optical-parametric oscillator. PhD thesis, ICFO, 2009.

[102] V. G. Lucivero. PhD thesis, 2016.

[103] Z. Instruments, "Principles of lock-in detection and the state of the art," CH-8005 Zurich, Switzerland, Accessed, 2016.

[104] D. Budker and D. Kimball, Optical Magnetometry. Cambridge University Press, 2013.

[105] F. Beduini, Entanglement and state characterisation from two-photon interference. PhD thesis, ICFO, 2015.

[106] F. Wolfgramm, Atomic quantum metrology with narrowband entangled and squeezed states of light. PhD thesis, ICFO, 2012.

[107] F. A. Beduini, J. A. Zielińska, V. G. Lucivero, Y. A. de Icaza Astiz, and M. W. Mitchell, "Interferometric measurement of the biphoton wave function," Phys. Rev. Lett., vol. 113, p. 183602, Oct 2014.

[108] K. McKenzie, E. E. Mikhailov, K. Goda, P. K. Lam, N. Grosse, M. B. Gray, N. Mavalvala, and D. E. McClelland, "Quantum noise locking," Journal of Optics B: Quantum and Semiclassical Optics, vol. 7, pp. S421–S428, sep 2005.

[109] G. Puentes, G. Colangelo, R. J. Sewell, and M. W. Mitchell, "Planar squeezing by quantum non-demolition measurement in cold atomic ensembles," New Journal of Physics, vol. 15, no. 10, p. 103031, 2013.

[110] R. Li, F. N. Baynes, A. N. Luiten, and C. Perrella, "Continuous high-sensitivity and high-bandwidth atomic magnetometer," Physical Review Applied, vol. 14, no. 6, p. 064067, 2020.

[111] M. Shi, "Investigation on magnetic field response of a 87Rb-129Xe atomic spin comagnetometer," Opt. Express, vol. 28, pp. 32033–32041, Oct. 2020. Publisher: OSA.

[112] Y. Yang, T. Wu, J. Chen, X. Peng, and H. Guo, "All-optical single-species cesium atomic comagnetometer with optical free induction decay detection," Applied Physics B, vol. 127, no. 3, p. 40, 2021.

[113] A. H. Jazwinski, Stochastic processes and filtering theory. Courier Corporation, 2007.

[114] M. Cerna and A. F. Harvey, "The fundamentals of fft-based signal analysis and measurement," tech. rep., Application Note 041, National Instruments, 2000.

[115] I. M. Savukov and M. V. Romalis, "Effects of spin-exchange collisions in a high-density alkali-metal vapor in low magnetic fields," Phys. Rev. A, vol. 71, p. 023405, Feb 2005.

Appendices

A

Diffusion term

The fluctuation dissipation theorem relates the diffusion and relaxation terms in linear stochastic differential equations. Often this is related to thermal noise, but here, since the spin system would relax to a maximum entropy state, i.e. a fully mixed state, the concept of temperature is not pertinent. Nonetheless, as in the case of relaxation through loss of energy to a finite-temperature thermal reservoir, one can relate the diffusion to the equilibrium variance.

Meanwhile, we can understand the spin noise by starting with Eq. (5.1). Our question is: what does the diffusion term $\mathbf{N}_F$ need to be, given the relaxation terms $-\Gamma\mathbf{F}$ and $-P\mathbf{F}$. We note that the terms with $\mathbf{B}$, S_3 and $P\hat{z}F_{\mathrm{max}}$ are not relevant to this question - they will influence the dynamics over longer times, but the relation between $\mathbf{N}_F$ and the relaxation terms must hold at every instant, and independently of the values of these other terms. For that reason, it suffices to consider

$$\frac{d}{dt}F_i = -(\Gamma + P)F_i + \Sigma_{ij}\eta_j, \qquad (A.1)$$

where η_j are independent Gaussian white noise, defined by $\langle\eta_i(t)\eta_j(t')\rangle = \delta_{ij}\delta(t-t')$ and Σ is a matrix. This describes an Ornstein-Uhlenbeck process [113], i.e., Brownian motion with relaxation toward $\mathbf{F} = \mathbf{0}$. Σ must satisfy the fluctuation-dissipation theorem, which is to say, give the correct equilibrium distribution for $\mathbf{F}$. For a spin-F system with small polarization, the equilibrium covariance matrix is $\mathrm{cov}(F_i, F_j) = \delta_{ij}N_A F(F+1)/3$ [2]. This is a diagonal matrix, indicating no correlations among different components F_i. It follows that each component F_i is independently described by the same Ornstein-Uhlenbeck equation

$$\frac{d}{dt}F_i = -\Gamma'F_i + \sigma\eta, \qquad (A.2)$$

---

[2] The spin variance is a function of spin polarization, becoming $\mathrm{cov}(F_i, F_j) = \delta_{ij}F/2$ for a fully-polarized state. At the same time, some spin-relaxation effects, notably spin-exchange broadening, are non-linear in the degree of polarization. These effects can be handled by including two hyperfine states in the description, but this is beyond the scope of the model we use here.

A. Diffusion term

where for convenience we have defined $\Gamma' \equiv \Gamma + P$. This has the well-known statistics $\langle F \rangle = 0$, $\langle F^2 \rangle = \sigma^2/2\Gamma'$ in the long-time limit.

The Wiener increment is defined by $E[dW] = 0$ and $E[dW^2] = dt$ and is independent of the current value of **F**. Considering now the equilibrium distribution of F, it is clear that the mean value will be zero. Meanwhile the increment of second moment will be

$$
\begin{aligned}
dE[F^2] &= E[(F + dF)^2] - E[F^2] \\
&= E[(F - \Gamma' F dt + \sigma dW)^2] - E[F^2] \\
&= -2\Gamma' E[F^2] dt + \sigma^2 E[dW^2] + O(dt)^2 \\
&= (-2\Gamma' E[F^2] + \sigma^2) dt.
\end{aligned} \tag{A.3}
$$

This vanishes, and thus the variance $E[F^2]$ is unchanging, when $\sigma^2 = 2\Gamma' E[F^2]$. We want this to occur when the spin variance is $E[F^2] = N_A F(F + 1)/3$, so we arrive to $\sigma^2 = 2\Gamma' N_A F(F + 1)/3$. In this way we obtain Eq. (5.2).

B

Magnetometer sensitivity calibration with the response to the external test signal

In this appendix, we present an alternative method for the calculation of the equivalent magnetic noise spectrum, based on the use of a test signal and the noise spectrum of the observed signal.

As discussed in chapter 6 , $\mathcal{S}_{\mathrm{v}}(\omega)$ is the power spectral density of the signal v after the lock in demodulation. When a magnetic test signal of amplitude B_{appl} and frequency ω_{appl} is applied along the bias field direction, it has an impact on the signal $v(t)$. Even though the effect of B_{appl} on $v(t)$ is small relative to the r.m.s. fluctuation, it can be seen in the power spectrum as a narrow line around the frequency ω_{appl} (Figure 4.3). The measurement is repeated for ω_{appl} ranging from 10 Hz to 2.4 kHz.

The maxima of the narrow lines are fitted to $f(\omega)$ (Equation 6.12) to give the amplitude spectral density of the magnetic signal as a function of frequency. A_{res} is the amplitude spectrum in V_{rms} of the observed signal and it is given by [114]

$$A_{\mathrm{res}}(\omega) = \sqrt{f(\omega)w_{\mathrm{Hann}}f_s},\tag{B.1}$$

where f_s the sampling frequency and $w_{\mathrm{Hann}} = 1.5$ the noise power bandwidth of the Hann window that is used for the data acquisition. The slope $dv/dB(\omega)$ is then computed as

$$\frac{dv}{dB}(\omega) = \frac{B_{\mathrm{appl}}(\omega)}{A_{\mathrm{res}}(\omega)}.\tag{B.2}$$

Combining this with Equation 6.9, the equivalent magnetic noise spectrum is

$$\mathcal{S}_B(\omega) = \mathcal{S}_{\mathrm{v}}(\omega)\left|\frac{dv(\omega)}{dB(\omega)}\right|^{-2} = \mathcal{S}_{\mathrm{v}}(\omega)\frac{B_{\mathrm{appl}}^2(\omega)}{A_{\mathrm{res}}^2(\omega)}.\tag{B.3}$$

To accurately determine the magnitude of B_{appl} we calibrate the signal of the waveform generator introduced in the modulation input of the low noise current
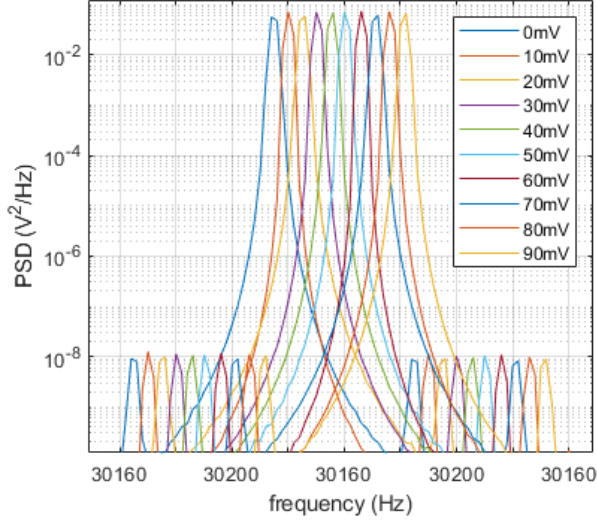
Figure B.1.: **Power spectra of the magnetometer signal for different DC modulation input.** The central frequency of the resonances are used for the calibration of V_{offset} to Larmor precession frequency

generator Twinleaf CSUA 300 to the bias field signal that the atoms are sensing. For this we introduce a dc offset on top of $4.3\,\mu$T bias field through the modulation input and measure the Larmor precession frequency of the atoms ω_L. For each value of V_{offset} we adjust the modulation frequency Ω of the optical pumping and keep it at the resonant value ($\Omega = \omega_L$) that maximizes the amplitude of the magnetometer's signal. As shown in Figure B.2, the central frequency of the resonance is shown to depend linearly from V_{offset}. From the equation of the linear fit of the data shown in Figure B.2 we obtain the calibration factor in (Hz/V). Multiplying with the gyromagnetic ratio [1] it is expressed in T/V. From this calibration method we infer that when an oscillating signal of amplitude $5\,$mV is given as modulation input to the low frequency noise generator, a magnetic test signal of amplitude $0.36\,$nT is generated along the bias field direction.

---

[1] The value of the gyromagnetic ratio of ^{87}Rb is to a good approximation $\gamma = 7\,$Hz$\,$nT^{-1}, since the operating conditions are outside the SERF regime ($\omega_0 T_{SE} \sim 63$ [115]).
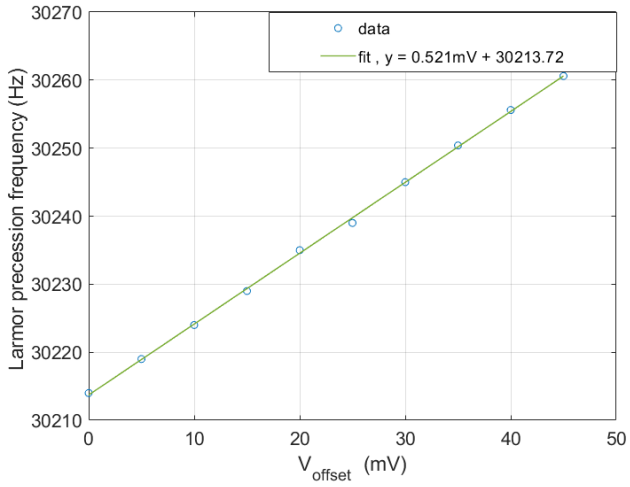
Figure B.2.: **Calibration of the DC voltage fed to the twinleaf modulation input to Larmor precession frequency** While operating the BB OPM at constant bias field we add in the same direction a modulation input from the DC offset V_{offset} of the waveform generator. The Larmor precession frequency values reported are the central frequency of the magnetic resonances for each V_{offset}.

Acknowledgement

I would like to begin by expressing my gratitude to my supervisor, Morgan Mitchell. I am very thankful that he trusted me with such a challenging project and guided me patiently throughout the process. At this point, I can confirm the claim on the web-page that a student of his group needs no previous experience, just passion, knowledge, and energy to overcome difficulties. He is a great scientist with very good teaching skills that can motivate inspiring conversations.

I would like to thank Ricardo Jiménez-Martínez for providing me the foundation of atomic magnetometers, Jia Kong for spending along with me a big part of my PhD, and had very input on quantum optics and atomic physics matters. I am grateful that Gianvito Lucivero joined the group during the final years of this project. It has been a pleasure working with him and for sure the schematics of the article would have been so nice without his contribution. I consider myself lucky to have learned from such great scientists that have always been available to offer advice and have formed an enjoyable and collaborative environment.

I would like to express my gratitude to Pau Gomez Kabelka who besides his busy schedule helped me with the abstract of the thesis in Català. Moltes gràcies! I am very thankful to Kostas Mouloudakis. It has been a great pleasure working with a good friend who is very knowledgeable on the topic. I have been happy to have collaborated with Michele Gozzelino on the squeezer setup during his visit to the group. I have learned a lot from the discussions on magnetometry and Matlab coding from Dominic Hunter, many thanks for the nice time in the lab even during the difficult moments of the pandemia. I am thankful for the smooth collaboration with Sven Bodenstedt and Michael Tayler.

Working in Morgan Mitchell's group offered a nice international environment through which I met very talented people and made dear friends. Huge thanks to Chiara Mazzinghi, Ola Sierant, and Vindhyia Prakash for their support and friendship advice and collaboration. I am grateful to Natalia Alves, Maria Hernandez, and Lorena Bianchet for the calm and supportive atmosphere in the office. Thanks to Natalia Bruno, Federica Beduini, Silvana Palacios, Giorgio Colangelo, Ferran Martin and Simon Coop for their useful advice and the smooth introduction to the group. I would like to acknowledge for their interesting conversations and always pleasant interaction Enes Aybar, Daniel Benedicto, Laura Zarraoa, Stuti Gugnani, and Tomas Lamich. Special thanks to Michal Lipka who along with Ola Sierant continued working on the magnetometer setup. I have been very happy to see the next generation of the experimental setup to which I devoted a lot of time and effort during the last years.

This work has been accomplished under very unique conditions of the pandemia and I often think that if it was not for the support of a network of friends

List of Publications

The main work arising from this thesis can be found in

- <u>Charikleia Troullinou</u>, Ricardo Jiménez-Martínez, Jia Kong, Vito Giovanni Lucivero, and Morgan W. Mitchell, *Squeezed-Light Enhancement and Back-action Evasion in a High Sensitivity Optically Pumped Magnetometer*,

  Phys. Rev. Lett. **127**, 193601 – Published: 2 November 2021

Other publications I participated in during my PhD:

- Jia Kong, Ricardo Jiménez-Martínez, <u>Charikleia Troullinou</u>, Vito Giovanni Lucivero, Géza Tóth and Morgan W. Mitchell, *Measurement-induced, spatially-extended entanglement in a hot, strongly-interacting atomic system*,

  Nature Communications volume **11**, Article number: 2415 (2020) – Published: 15 May 2020

- Ricardo Jiménez-Martínez, Jan Kołodyński, <u>Charikleia Troullinou</u>, Vito Giovanni Lucivero, Jia Kong, and Morgan W. Mitchell, *Signal Tracking Beyond the Time Resolution of an Atomic Sensor by Kalman Filtering*,

  Phys. Rev. Lett. **120**, 040503 – Published 26 January 2018